Electrochemical Energy Reviews (2022) (Suppl 2) 5:28
https://doi.org/10.1007/s41918-022-00171-5

REVIEW ARTICLE

Recent Advances and Perspectives of Electrochemical CO_2 Reduction Toward C_{2+} Products on Cu-Based Catalysts

Xiaodeng Wang[1,2] · Qi Hu[1] · Guodong Li[1] · Hengpan Yang[1] · Chuanxin He[1]

Received: 2 December 2021 / Revised: 10 February 2022 / Accepted: 2 June 2022 / Published online: 20 November 2022

Abstract
Renewable-electricity-powered electrochemical CO_2 reduction reactions (CO_2RR) to highly value-added multi-carbon (C_{2+}) fuels or chemicals have been widely recognized as a promising approach for achieving carbon recycling and thus bringing about sustainable environmental and economic benefits. Cu-based catalysts have been demonstrated as the only candidate metal CO_2RR electrocatalysts that catalyze the C–C coupling. Unfortunately, huge challenges still exist in the highly selective CO_2RR to C_{2+} products due to the higher activation barrier of C–C coupling and complex multi-electron reaction. Key fundamental issues regarding both active species and product formation pathways have not been elucidated by now, but recent developments of advanced strategies and characterization tools allow one to comprehensively understand the Cu-based CO_2RR mechanism. Herein, we review recent advance and perspective of Cu-based CO_2RR catalysts, especially in terms of active phases and product formation pathways. Then, strategies in catalysts design for CO_2RR toward C_{2+} products are also presented. Importantly, we systematically summarized the advanced tools for investigating the CO_2RR mechanism, including in situ/operando spectroscopy techniques, isotope labeling, and theoretical calculations, aiming at unifying the knowledge of active species and product formation pathways. Finally, future challenges and constructive perspectives are discussed, facilitating the accelerated advancement of CO_2RR mechanism research.

Keywords CO_2RR · Raman spectrum · Active phases · Formation pathways · Reaction mechanisms · Copper · DFT calculations

1 Introduction

In the past hundreds of years, especially after the Second Industrial Revolution, the development of human society has been heavily dependent on fossil fuels as the main energy sources, such as coal and oil. Due to the excessive consumption of fossil fuels, the concentration of CO_2 in the atmosphere increases sharply from 270 ppm (1 ppm = 1 mL m^{-3}) in the early 1800s to 410.45 ppm in June 2019 [1–7], bringing about a series of problems including global warming and energy crisis. In terms of reducing the concentration of atmospheric CO_2, replacing fossil fuels with various clean and renewable energy such as solar and wind is one potential approach to reduce the emission of CO_2. On the other hand, converting CO_2 to value-added fuels through CO_2 reduction reactions (CO_2RR) has recently received extensive attention and been devoted to reducing the present CO_2. It is noted that the renewable energy sources were difficult to be used because of their intermittent nature and stored by limited storage devices. Therefore, CO_2RR using renewable electricity can not only be converted into fuels and chemical industry to achieve carbon recycling, but also solve the problems of the intermittent and unstable renewable energy utilization [8–12].

Since Hori et al. systematically investigated the CO_2RR performance of various metal electrodes in the 1980s and 1990s [13], extensive studies used to improve the activity and selectivity of CO_2RR catalysts have been reported. Among various CO_2RR electrocatalysts investigated so far, Cu-based materials have been considered to be the only metallic electrocatalyst capable of reducing CO_2 to

✉ Qi Hu
hq2016@szu.edu.cn

✉ Chuanxin He
hecx@szu.edu.cn

[1] College of Chemistry Environmental Engineering, Shenzhen University, Shenzhen 518060, Guangdong, China

[2] School of Electronic and Electrical Engineering, Chongqing University of Arts and Sciences, Chongqing 400030, China

multi-carbon oxygenates and hydrocarbons (denoted as C_{2+} products) [14–18]. Therefore, the development of various Cu-based electrocatalysts has greatly improved the overall performance for decades. Nevertheless, high overpotential is required due to the stable structure of CO_2 molecules and the relatively low Faradaic efficiencies (FEs) are observed due to the competing hydrogen evolution reaction (HER). Furthermore, the extremely strong reducing power leads to the wide product distribution of Cu-based CO_2RR electrocatalysts, reducing the selectivity of a specific product. The complexity of the CO_2RR mechanism not only is reflected by the high probability that C_{2+} products share the same intermediates and have cross-reaction pathways, but also arises from the fact that the product distribution is highly surface-sensitive. In particular, four possible intermediates for the formation of C_2H_4 and EtOH (i.e., *COCHO, *CHCOH, *CCH, and CH_2CHO*) have been proposed and the adjusted ratio of their FEs has been extensively studied [19–23]. Although multiple factors (i.e., physical and chemical properties, the change of the surface state, defects, etc.) have been reported to play a key role in the catalytic activity of Cu-based catalysts, surface speciation on the surface of various types of Cu during CO_2RR remains still under debate [24, 25]. Therefore, we believe that tracking the evolution of surface speciation and gaining a deeper insight into reaction pathways will guide the future design of efficient electrocatalysts for producing CH_4 and C_{2+} products.

With the rapid development of density functional theoretical (DFT) calculations and advanced characterization technologies, great efforts have been devoted to exploring the mechanism of Cu-based CO_2RR catalysts, especially the determination of the chemical state of Cu sites and the exploration of CO_2RR pathways. Therefore, we aim to comprehensively review recent advances and perspectives in understanding the mechanism of Cu-based CO_2RR catalysts, which have brought about considerable improvements in identifying the active sites and possible reaction pathways. This review would begin by introducing the CO_2RR mechanism on Cu-based catalysts, including the discussion of the active sites, the summary of main C_{2+} product pathways, and the main factors affecting CO_2RR performance. As shown in Scheme 1, we then discuss strategies in catalyst design for CO_2RR toward C_{2+} products, as well as advanced tools for investigating CO_2RR mechanisms. An overview of strategies and advanced tools improves understanding of the active phase of catalysts, the selectivity of C_{2+} products, key intermediate states, and the rate-determining step (RDS). Furthermore, the future development and challenge, and more deeper insights into the mechanism of Cu-based CO_2RR catalysts are also discussed.

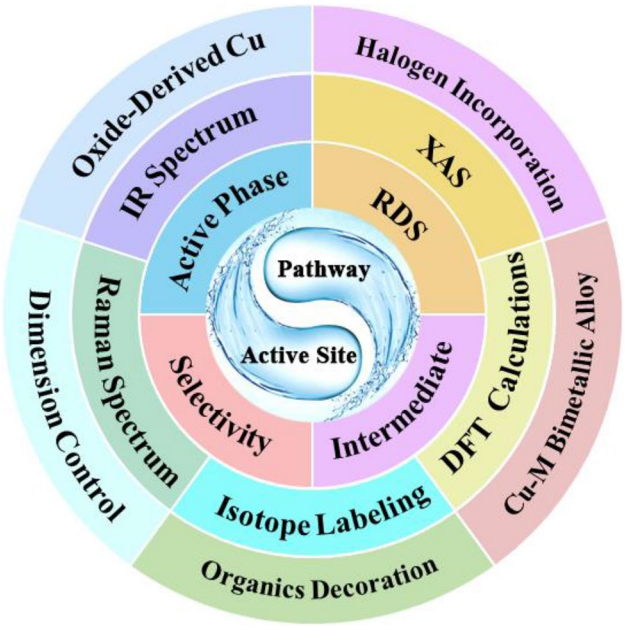

Scheme 1 Outline of this review. Recent strategies and advanced tools are further summarized to improve understanding of the CO_2RR mechanism, especially the discussion of active sites and possible reaction pathways

2 Mechanism on CO_2RR on Cu Catalysts

2.1 An Overview of CO_2RR Mechanisms on Cu-Based Catalysts

Designing a complete and coherent schematic diagram to understand the overall mechanism of CO_2RR is a challenging task, owing to the highly complicated and multiple processes with multi-electron/proton transfer via various reaction pathways in an aqueous solution [24–30]. For Cu-based catalysts, the distribution of products is broad, such as main C_1 (CO, HCOOH, and CH_4) and C_2 ($H_2C_2O_4$, C_2H_4, C_2H_6, and EtOH) and C_3 (PrOH) products. Table 1 summarizes the half-reactions of C_{2+} products that can be produced from the CO_2RR with the corresponding reversible hydrogen electrode (RHE) potential. Despite the variety of the products, the first step of CO_2RR is the initial activation of CO_2 molecules. However, the formation of the $CO_2^{\cdot-}$ radical intermediate via one-electron injection process requires a very negative redox potential [−1.9 V vs. standard hydrogen electrode (SHE)] because CO_2 is a very stable molecule. The adsorption of CO_2 generates CO by breaking the C–O bond or formate through the formation of the C–H bond, in which the obtained *CO is a key intermediate for CH_4, alcohols, and C_{2+} products.

In general, the whole formation of C_{2+} products mainly included four steps: (1) the formation *CO; (2)

Table 1 Standard equilibrium potentials for the electrochemical CO_2 reduction to CO and further reduced C_{2+} products

Reaction	Name	E^0/(V vs. SHE)
$CO_2 + 2H^+ + 2e^- \rightleftharpoons CO_{(g)} + H_2O_{(l)}$	CO	−0.10
$2CO_2 + 8H^+ + 8e^- \rightleftharpoons CH_3COOH_{(aq)} + 2H_2O_{(l)}$	Acetic acid (HAc)	0.11
$2CO_2 + 10H^+ + 10e^- \rightleftharpoons CH_3CHO_{(aq)} + 3H_2O_{(l)}$	Acetaldehyde (AcH)	0.06
$2CO_2 + 12H^+ + 12e^- \rightleftharpoons C_2H_5OH_{(aq)} + 3H_2O_{(l)}$	Ethanol (EtOH)	0.09
$2CO_2 + 12H^+ + 12e^- \rightleftharpoons C_2H_{4(g)} + 4H_2O_{(l)}$	Ethylene (C_2H_4)	0.08
$2CO_2 + 14H^+ + 14e^- \rightleftharpoons C_2H_{6(g)} + 4H_2O_{(l)}$	Ethane (C_2H_6)	0.14
$3CO_2 + 18H^+ + 18e^- \rightleftharpoons C_3H_7OH_{(aq)} + 5H_2O_{(l)}$	Propanol (PrOH)	0.10

the formation of the C–C bond; (3) post-C–C-coupling; (4) desorption of products. However, in the case of the formation of C_{2+} products on Cu-based catalysts, clarifying the formation path of the product is a huge challenge. Most possible C_{2+} pathways during CO_2RR are summarized in the previous reviews [2, 9, 26, 31, 32], which clearly demonstrate that the mechanism is complex due to the presence of many intermediates and pathways. In addition, the selectivity and pathways of C_{2+} products are highly dependent on the active phase of Cu-based electrocatalysts and the surrounding electrolyte, such as the chemical state, exposed crystal face, pH value, and composition of the electrolyte.

2.2 True Active Sites: Cu^0 or Cu^+

The complexity of CO_2RR on Cu-based catalysts arises from the abundance of C_{2+} products, involved multiple proton/electron transfer steps, and the activity and selectivity of C_{2+} products are highly surface-sensitive, especially for oxide-derived Cu (OD-Cu) catalysts [16, 33]. Though various OD-Cu catalysts have been designed and significantly improved the activity and selectivity of C_{2+} products during CO_2RR, the mechanism of the significant enhancement toward C_{2+} products remains controversial. Fundamentally, since the standard reduction potential of Cu^+/Cu^0 redox is − 0.36 V, Cu-based catalysts are thermodynamically metallic following the Pourbaix diagram under the potentials of CO_2RR [24]. Therefore, many researchers believe that the active phase is metallic Cu, and the related mechanism of enhanced activity and selectivity on OD-Cu catalysts during CO_2RR is attributed to unique structures, grain boundaries, low-coordinated atoms, defective sites, and roughened morphology [34]. However, on one hand, the state of Cu can easily vary due to the reversible change between the oxidation state and the reduction state of Cu under electrochemical reaction condition. On the other hand, the kinetics of Cu reduction is slow, which is confirmed by many characterizations [35]. Furthermore, many groups confirm that the Cu^+ sites remain on the surface of catalysts and the key active sites during CO_2RR.

By combining experimental and theoretical research, it has been proposed that under the condition of CO_2 reduction, the presence of metastable states (such as residual oxygen, underground oxygen, and the Cu oxide state) significantly enhances the activation of CO_2 and reduces the energy barrier of CO–CO dimerization to promote C_{2+} pathways [36, 37]. DTF calculations suggested that during the initial step of CO_2 activation, the strong H_2O adsorption site on top of the Cu^+ region can provide hydrogen bonding to stabilize the CO_2 on the adjacent Cu^0 region. For the followed *CO dimerization step, due to the opposite Mulliken charges of *CO on Cu^+ and Cu^0, this electrostatic force significantly improved the kinetics of CO–CO coupling, thus improving the selective of C_{2+} products. Mistry et al. reported that the presence of Cu^+ played a key role in lowering the onset potential and improving C_2H_4 selectivity by using operando X-ray absorption spectroscopy (XAS) and cross-sectional scanning transmission electron microscopy (STEM) [35]. Recently, the influence of the Cu oxidation state on the catalytic performance has been widely discussed and summarized. Interesting, by summarizing various Cu catalysts related on Cu^+ species [24], Chen and coworkers found a link between the chemical state and selectivity. They proposed that the mixed Cu^+ and Cu^0 states favored the selectivity of C_2 products, while the Cu^+- and Cu^0-dominated states enhanced the selectivity of C_1 products.

Although experimental and theoretical studies indicate that the Cu^+ states play a key role in improving the selectivity of C_{2+} products, no direct experimental studies showed that this high selectivity was attributed to the Cu^+ states. Remarkably, Xu and coworkers firstly reported that CuO_x and $CuO_x/(OH)_y$ species are unlikely to be the active sites for facilitating the formation of C_{2+} products by combining variation trends of product selectivity and spectroscopic results [25, 38]. Furthermore, Xu's group also found that the Cu–O species were pH dependent by in situ surface-enhanced Raman spectroscopy (SERS), which could be completely reduced in the nearly neutral electrolyte [39]. This phenomenon is generally confirmed by recent reports related to Raman spectroscopic results. Importantly, in addition to Raman spectroscopic characterizations, fully reduced Cu–O species were observed in CO_2-saturated

0.1 M (1 M = 1 mol L^{-1}) $KHCO_3$ during CO_2RR by electron energy loss spectroscopy (EELS), in situ electrochemical TEM and the quasi-in situ X-ray photoelectron spectroscopy (XPS) analysis, but associated catalysts still maintained high selectivity of C_{2+} products [40, 41]. The above results were discussed in detail in Sect. 4.1, and those investigations further confirmed that surface oxygen-containing species were indeed completely reduced, indicating that Cu–O species are not the active sites for the formation of C_{2+} products. Furthermore, the differences of CO adsorption bands on mechanically polished polycrystalline Cu (referred to as Cu-MP) and anodized Cu-MP were monitored by using time-resolved SERS in CO_2-saturated 0.1 M $KHCO_3$ [42], which was consistent with that of polycrystalline Cu and OD-Cu reported by Xu and coworkers in CO-saturated 0.05 M KOH, indicating that changes of nanostructure and nanomorphology may play key roles in improving selectivity of C_{2+} products. In addition, the coordination number of OD-Cu catalysts was obtained by fitting extended X-ray absorption fine structures (EXAFS) curve, which was lower than that of Cu foil, indicating that undercoordinated Cu sites might play a key role in improving the selectivity of C_2 products.

2.3 Possible Reaction Pathways to C_{2+} Products

Due to the competitive undesired HER and higher activation barrier of C–C coupling as well as competition of C–C, C–O and C–H bond formations, the formation of C_{2+} products from CO_2RR on Cu-based electrocatalysts is a difficult and complex multi-electron reaction. There are two proposed mechanisms for C–C bond formation: the Eley–Rideal mechanism (E–R), in which gas CO is the reactant, and the Langmuir–Hinshelwood mechanism (L–H), in which catalyst surface adsorbed CO is the reactant. Calle-Vallejo et al. suggested that CO–CO coupling mainly proceeded through the E–R mechanism on Cu(1 0 0) by using a purely thermodynamical model, in which gaseous CO may insert itself into the bond between the Cu surface and adsorbed CO [21]. Major pathways for C_{2+} products are usually associated with the L–H mechanism to form a $*C_2O_2$ intermediate, which can be hydrated to generate C_{2+} products [43, 44]. Importantly, the energy barriers of the C–C coupling via the E–R mechanism were higher than that of the L–H mechanism [45]. The C–C coupling mechanism was controversial and affected by many factors, including applied potentials, cation, tensile strain, and CO partial pressure, which could be beneficial to increase *CO coverage and reduce activation energies for *CO dimerization [46–50]. Therefore, understanding the C–C coupling mechanism and determining the reaction path of products will be more conducive to the design of catalysts for highly selective C_{2+} compounds rather than C_1 chemicals. Possible reaction pathways for C_{2+} products (C_2H_4, C_2H_6, EtOH, and PrOH) are summarized in this section and that of other products can be found in other reviews [27, 32, 51].

2.3.1 C_2H_4 Pathway

To date, although two different pathways of the C_2H_4 formation based on the overpotential have been proposed during CO_2RR and CO reduction reactions (CORR) on the Cu single-crystal surface, the mechanism of C_2H_4 formation is still under debate on Cu-based catalysts. In earlier studies, the direct CH_2–CH_2 coupling has been proposed to form C_2H_4 [52], while recent studies suggested that the formation of C_2H_4 was more likely through CO dimerization [49, 53]. For the first time, Hori et al. reported that the C_2H_4 formation was pH independent, while the CH_4 formation depended on the pH [13]. This indicated that the RDS of CH_4 pathway involved a coupled proton–electron transfer, whereas that of C_2H_4 did not. However, the process of C–C coupling was still controversial. Koper and coworkers used differential electrochemical mass spectrometry (DEMS) technique to explore the intermediate of C–C coupling [54]. They concluded that the first step of the C_2 pathway was CO–CO coupling, followed by the protonation (CO–CHO) to form a surface-bonded enediol or enediolate, or an oxametallacycle, which would explain the selectivity toward C_2H_4. They also proposed two different pathways of C_2H_4 formation with different overpotentials by using DEMS [55]. The high-overpotential pathway shares the same RDS intermediate as CH_4, occurred both on Cu (100) and (111) facets, while the low-overpotential pathway involves the RDS of CO–CO coupling on Cu (100) facet.

Apart from the DEMS technique, employing in situ Fourier transform infrared spectroscopy (FTIR) [56], OC–COH took place on the Cu (100) facet, while not found on the Cu (111) facet. For Cu-based catalysts, the intermediate of CHO–CHO [57] and CH_2–CO [58–61] were proposed as the pathway of C–C coupling to elucidate the mechanism of C_2H_4 formation. Wang and coworkers proposed a H-assisted CHO–CHO coupling mechanism for C_2H_4 formation combined DFT calculations and experiments on Cu (111) [62]. In addition, the intermediate of CH_2–CO in the C_2H_4 pathway could be detected on Cu-based composite catalysts. For instance, on Cu-Ag composites [61], CO_2 could be first reduced to CO and then bind to either Cu or Ag sites, while CO on the Cu sites could be reduced further to CHO or CH_x intermediates. The CO on Ag sites may then insert itself into $*CH_2$ to form $*COCH_2$ intermediates of C_2H_4 pathway.

2.3.2 EtOH Pathway

It is generally believed that EtOH is proposed to share the similar intermediates at the early stages of CO/CO_2

reduction such as C_2H_4. Therefore, the C–C coupling is also considered to be the key step for EtOH formation, including two reaction pathways involved CO–CO couplings and *CHO or *CH_x intermediates inserted CO. Zhang et al. demonstrated that ionic liquids, as a chemical trapping agent, could selectively suppress the formation of products during CO_2RR [63]. They proposed that EtOH can be produced through the pathway of *CH_2 intermediates inserted CO, while C_2H_4 can be produced through two independent pathways. This mechanism was widely present in Cu-based alloy catalysts, which are discussed in detail in Sect. 3. For the CO–CO coupling pathways, *CHCOH and *$OCHCH_2$ have been reported as sharing intermediates that determine the selectivity of C_2H_4 and EtOH [22, 23]. Calle-Vallejo and coworkers reported that the reaction barriers of CO/CO_2 reduction to EtOH were larger than that of C_2H_4 by combining experimental and computational studies, and hence it was easier to form the latter [64], which was consistent with the selective tendency of Cu-based catalysts. In addition, H. Sargent and coworkers reported that reaction intermediates starting from *HCCOH become more favorable for EtOH by introducing Ag on the Cu surface [23]. They also found an alternative catalytic approach to promote EtOH by increasing the energy barrier of intermediates starting from *$OCHCH_2$ to C_2H_4 [22].

2.3.3 C_2H_6 Pathway

Ethane, as a minor product on the Cu-based catalysts during CO_2RR, has only been reported occasionally [65–71]. In analogy with EtOH, C_2H_6 can be formed through the similar intermediates for the electrocatalytic reduction of CO/CO_2, including two important pathways: (1) *CO dimerization pathways, and (2) coupling of *CH_x accompanied by further hydrogenation [65, 66, 72]. The intermediate of *OC_2H_5 derived from *C_2O_2 was reported as the key in determining selectivity between C_2H_6 and EtOH. Therefore, C_2H_6 and EtOH should be detected together, which is consistent with previous reports [65, 73]. However, on one hand, Zhang et al. demonstrated only EtOH was detected by using ionic liquids via the intermediate of *OC_2H_5 on the Cu foam catalyst [63]. On the other hand, Bertheussen et al. reported that C_2H_6, AcH, and EtOH were observed during CORR on OD-Cu electrodes [74], while only C_2H_6 was not detected through the CH_2CHO reduction, indicating that the formation of C_2H_6 from *OCH_2CH_3 can be ruled out. In addition, D. Handoko et al. reported that the formation of C_2H_6 was likely to originate from the *CH_3 dimerization by adding diacetyl as the reactant, rather than further hydrogenation of *C_2H_4 or *OCH_2CH_3 [66].

2.3.4 PrOH Pathway

In order to improve the FE of PrOH, much research effort has been dedicated. More recently, the FE for PrOH product during CO_2RR was enhanced through the modification of Cu-based catalysts, which include reconstructed nanocrystals [75], dense pack [76], two-step activation [77], Cu^{2+} ion cycling [78], and core–shell structures [22]. However, the mechanism of C–C coupling, especially in PrOH generation of CO_2RR and CORR, remains a challenge. So far, it has been proven that C_2H_4 is an intermediate in the formation of PrOH in CO_2RR and CORR. Ren et al. reported that significant amounts of PrOH could be observed when using a 1:1 mixture of C_2H_4 and CO, while little or no detectable amounts of PrOH are produced when only CO or C_2H_4 were reduced [75]. During CO_2RR, PrOH generation was optimized when both C_2H_4 and CO are formed at a high rate. They concluded that PrOH could be formed through the coupling of C_2H_4 with CO. H. Sargent and coworkers designed a strategy via binding of C_2 intermediates to boost selectivity from C_2 to C_3 products [79]. The combined product distributions showed that the increase production of PrOH corresponded to the decrease in C_2H_4, indicating that the C_2 intermediate coupling with CO for PrOH generation may be related to C_2H_4. In addition, Han and coworkers observed that PrOH and EtOH followed a similar trend of increasing selectivity with the corresponding decrease in C_2H_4, indicating the presence of a common intermediate in the reaction process [80]. Further DFT calculations suggested the stabilization of *OCH_2CH_2 intermediate was favorable for the formation of PrOH and EtOH, which was in agreement with previously reported mechanisms for PrOH production [22].

However, it was also generally accepted that the formation of PrOH involved the dimerization between CO and hydrogenated carbon (e.g., *CH_2), followed by proton/electron transfer to form propionaldehyde, and then further reduced to PrOH. For instance, Yang and coworkers proposed that PrOH formation required coupling between CO and *CH_2 by analyzing Tafel slopes and potentials of CH_4 and PrOH [76]. Zhang et al. demonstrated that the formation of PrOH involved *CH_2 by using the chemical trapping agent of ionic liquids, which was also the intermediate of EtOH and C_2H_4 [63]. In addition, Xu and coworkers reported that a small proportion of PrOH come from cross-coupling between CO and AcH when using CO and AcH by combining isotope labeling and spectroscopic techniques, while the main PrOH was produced through self-coupling of CO [81]. Therefore, they demonstrated that the C–C coupling between CO and AcH was unlikely to be the main pathway during CORR.

2.4 Factors Influencing the Formation of C–C Bond in C_{2+} Products

In general, pathways of CO_2RR to various C_{2+} products are highly influenced by applied overpotential, liquid electrolyte, and properties of the electrocatalyst. In the CO_2RR process, liquid electrolytes, including ionic liquids [82, 83], organic electrolytes [84, 85], and aqueous electrolytes, can realize ionic transport and provide a reaction environment. Most of the research on CO_2RR has been carried out in aqueous electrolytes and recent advances in other electrolyte types are presented in other reviews [34, 86]. The intrinsic properties of electrocatalysts (facets, defects, and morphology) significantly affect the adsorption energy of intermediates and the energy barrier of CO_2RR, which changes the pathway of products. In this section, we will discuss in detail the three main factors that influence the product pathways: pH, cations, and facet effects.

2.4.1 pH Effect

The pH is an essential factor in determining the activity and selectivity due to the complex protonation process during CO_2RR, especially inhibiting the HER and turning the ratio of C_1/C_2 products for Cu-based catalysts [27, 87]. In general, as the pH increases, the selectivity of the product shifts from H_2 and CH_4 to multi-carbon products such as C_2H_4 [88]. However, the effect of pH on CO_2RR products is very complex, which may be related to the multiple proton-coupled-electron transfer and the RDS in different reaction pathways [78, 89, 90]. The difference of the formation, the starting potential, and the Tafel slope of CH_4 and C_2H_4 indicates that they follow different reaction paths [91]. For the first time, Hori and coworkers proposed that the reaction rate for CH_4 is pH dependent on the normal hydrogen electrode (NHE) scale due to the coupled proton–electron transfer of *CO during the RDS [58], while that of C_2H_4 was shown to be pH independent. By contrast, Schouten's group reported that the onset potentials of CH_4 and C_2H_4 on Cu (111) electrodes were both pH dependent through online electrochemical mass spectrometry (OLEMS) [92]. This can be explained by the coexistence of two different C_2H_4 formation pathways. The high-overpotential pathway on Cu (100) and (111) facets shares the same RDS with CH_4 (*CO protonation) and the low-overpotential pathway on Cu(100) involves the CO–CO coupling [55]. Contrary to the second pathway, the first pathway, which includes CH_4 and C_2H_4, shows a pH dependence on the SHE scales as there is a coupled proton/electron transfer of CO involved. It was concluded that both the CO–CO coupling or proton–electron transfer from water during the RDS are conceivable elucidations for the pH independence of the C_{2+} pathway on the SHE scales.

The bulk pH, however, is different from that at gas–liquid–solid three-phase interfaces due to the unbalance between the supply and the consumption of protons [27]. The shift of local pH during CO_2RR depends on the bulk pH in the electrolyte, buffer capacity of the electrolyte, the current density, and the morphology of catalysts [93, 94]. The selectivity toward C_2 products on Cu-based catalysts can also be tuned by inhibiting the production of CH_4 and H_2 in the buffer electrolyte, which depends on the nature and concentration of electrolyte [35, 47, 95, 96]. Furthermore, by considering solvent effects using implicit solvation model, DFT calculations presented that the C_1 and C_2 paths on Cu(111) are competing and products are pH-dependent underlying CORR [97]. At low pH, the C_1 pathway forms CH_4 through *COH to *CHOH, while C_{2+} pathways are suppressed kinetically. At neutral pH, the C_1 and C_{2+} pathways share a common *COH, in which the branching C–C coupling is achieved through the pathway of CO–COH. At high pH, selectivity for C_{2+} products through the early C–C coupling arises by kinetically blocking C_1 pathways [98]. Based on the above analysis, especially for Cu-based catalysts, higher pH electrolytes are more favorable for the generation of C_{2+} products [88]. For instance, Sargent and coworkers reported that the Cu catalyst reduced CO_2 into C_2H_4 with 70% FE at -0.55 V_{RHE} in a strong alkaline electrolyte (7 M KOH). Combined experimental and theoretical insights, strong alkaline media can accelerate the kinetics of CO_2RR by lowering the CO_2 reduction and the C–C coupling energy barrier and stabilizing the adsorbed OCCO through a stronger dipole attraction. Therefore, more researchers are investigating higher concentration of KOH as electrolytes to further enhance the FE of C_{2+} products [99].

However, as shown by experimental investigations and DFT calculations, the current mechanistic understanding of the formation of C_{2+} products suggests that the C_{2+} pathway of CO–CO coupling is pH independent, in which there is no proton transfer in this L–H process. Recently, Lu and Xu pointed out that the reactions performed at a higher electrolyte pH are actually subjected to a larger overpotential by $\Delta pH \times 59$ mV, and the catalytic effect of the highly alkaline electrolyte could be exaggerated when comparing C_{2+} products formation rates [100]. Systematically varying the concentration of Na^+ and OH^-, they first found that the rate of C_{2+} product increased significantly with the increase in OH^- concentration under the same RHE scale, which was similar to the phenomenon in the previous study. However, the RDS of C_{2+} products is pH independent, so it is reasonable to compare the C_{2+} products formation rate at the same SHE scales. Based on the same SHE scales, they found that the formation rate of C_{2+} products did not change with the increase in OH^- concentration, and at the same OH^- concentration, that increased significantly with the increase in Na^+ concentration. Therefore, they concluded that the increase in

Na^+ concentration, rather than OH^-, improved the formation rate of C_{2+} products during CORR at the SHE scales. The introduction of crown ether led to a sharp decrease rate of C_{2+} products formation, further confirming the effect of the nature and concentration of cations for CORR.

2.4.2 Cation Effect

Much research effort reported that the cations in the electrolyte play a key role in influencing the activity and selectivity of catalysts at the reaction interface during CO_2RR and CORR [47, 50, 98, 101]. The involved mechanisms have been discussed widely since it was first reported decades ago. Akira and Hori observed that the selectivity of C_2H_4 and alcohols was progressively higher than that of CH_4 and H_2 with ionic size increasing from $Li^+ < Na^+ < K^+ < Cs^+$ [102]. They proposed that this cationic effect stems from the adsorption tendency of cation on electrode surfaces, which is mainly determined by the reaction energetics and the degree of cation hydration. The hydration capacity could be stronger with ionic size increasing, and the larger size cation is not only more likely to be adsorbed, but also can be rejected by H^+ to reduce the selectivity toward CH_4 and H_2. In addition, Thorson et al. proposed that adsorbed cations at the electrode surface could stabilize the intermediate $*CO^{2-}$ to promote the CO_2RR [103]. Kim et al. observed that the generation of CO was more efficient in K^+-based electrolytes than that of Na^+ [104]. Further DFT calculations clarified that the local electric field induced by alkali metal cations is beneficial to enhance the stability of intermediates such as *COOH and *CO, and thus lower the thermodynamic energy barrier [105, 106]. However, by taking into account the solvent effect, this effect was not observed by the Ab Initio Molecular Dynamics (AIMD) simulations [107].

In addition to the effect of cation adsorption and stabilizing intermediates, the mechanism of electronic field effects induced by cations was also mentioned, which was strongly dependent on the size of hydrated cation [108–110]. Recently, Chan et al. reported that the multi-scale modeling approach was able to have an extraordinary quantitative consistency with experimental trends in cation effects, supporting the effect of cations by changing the interfacial electric field [108]. Due to the less surrounded H_2O for larger cations, the size of hydrated cations was arranged in order: $Cs^+{\cdot}xH_2O < Rb^+{\cdot}xH_2O < K^+{\cdot}xH_2O < Na^+{\cdot}xH_2O < Li^+{\cdot}xH_2O$. Therefore, the smallest size of $Cs^+{\cdot}xH_2O$ showed the strongest electric field, which could facilitate the adsorption of intermediates and the generation of multi-carbon products [110, 111]. For example, on O_2-plasma-activated Cu, the current density and selectivity of C_{2+} products increased with the increase in alkali metal cation size [110]. Further DFT calculations showed that larger cations are more conducive to adsorption, resulting in the stabilization of the CO_2RR intermediates to enhance the generation of C_{2+} products. However, based on the Poisson-Nan-Planck model, the interfacial electric field of Cs^+ is weaker than that of K^+ due to the reduced dielectric constant [112]. It was noted that the promotion effect of alkali metal cations may be related to not only the electric field but also the pK_a for the hydrolysis. Bell and coworkers proposed that the FE of C_2H_4 and EtOH increased with the increase in alkali metal cation size [113], which was ascribed to the hydrolysis capacity of cations. With the increase in cation size, the pK_a decreased, which reduced the pH value to increase the CO_2 concentration near the cathode.

Although a variety of possible ways in which cations influence surface-mediated electrocatalytic reactions have been proposed, no consensus has been reached due to the lack of direct experimental evidence. The Stark tuning rate is usually used to represent the electric field strength, which is obtained by fitting the slope of the peak frequency of the *CO stretch band and the corresponding applied potential [100, 114, 115]. Using surface-enhanced infrared absorption spectroscopy (SEIRAS) [115], Waegele and coworkers found that the electric field intensity was too small to have a significant effect on the observed changes in C_2H_4 selectivity, but sharp peaks generated by the interaction of *CO and H_2O were detected. They suggested that the C_2H_4 collection efficiency was due to the changing interaction between *CO and H_2O in the presence of different cations. In addition, recent studies by Xu and coworkers demonstrated that the reaction rate can be significantly increased by increasing the cation concentration without the change of interfacial electric field intensity, which is determined by the Stark tuning rate [100]. This result indicated that the interfacial electric field intensity is not a key parameter of CORR. Furthermore, Xu et al. also systematically studied on the impact of cationic effects, including electricity and non-electric field (NEF) strength components [116]. In this work, the rates of CORR and HER increased with the increase in cation size on polycrystalline Cu catalysts, while the FE of CORR products also increased from Li^+ to K^+, but leveling off for the larger cations. The Stark tuning rate measurements by using in situ SEIRAS investigations in five different alkaline metal cation electrolytes implied that the size of electrochemically related cation followed the sequence: $Cs^+{\cdot}xH_2O \sim Rb^+{\cdot}xH_2O \sim K^+{\cdot}xH_2O < Na^+{\cdot}xH_2O < Li^+{\cdot}xH_2O$. The variation trend of the reactivity rate and Stark tuning rate is similar in these cation-containing electrolytes. They drew a conclusion that the cationic effect has both the favorable interfacial electric field strength and the unfavorable NEF strength component.

2.4.3 Facet Dependency

Experimentally, it is well established that the activity and selectivity of catalysts during CO_2RR and CORR are strongly dependent on the surface crystal facets of Cu-based catalysts [27, 117, 118]. It has been confirmed that the Cu (100) facet particularly increases the selectivity for C_2 products, especially C_2H_4, while Cu (111) favors preferentially the generation of CH_4 [109]. The generation of C_2H_4 on the Cu (100) facet follows two different pathways depending on the applied overpotentials. At low overpotentials, C_2H_4 is pH dependent and exclusively produced through CO–CO coupling. At high overpotentials, the formation of C_2H_4 and CH_4 via a *CHO pathway are strong pH dependent on the SHE scales, similar to that on the Cu (111) facet. In addition, Cu (110) facet preferentially increases the selectivity for CH_4 containing trace amounts of C_2H_4. Apart from CH_4 and C_2H_4, liquid, oxygenated compounds also could be detected on the low-index Cu facets [e.g., Cu (111), Cu (110), Cu (100)] [96, 101]. Hori et al. reported that the Cu (111) facet preferentially formed HCOOH compared to alcohols, while the opposite could be detected on the Cu (100) facet. The Cu (110) facet yielded similar selectivity toward liquid and oxygenated compounds [91].

Similar to the low-index of the Cu (100) facet, the stepped Cu (211) facet is favorable for CO–CO coupling compared with Cu (111), and thus is beneficial for the formation of C_{2+} products [78, 119–121]. A. Nilsson et al. reported the C_2H_4 and CH_4 products of three Cu single-crystal surfaces (100), (111), and (211). They offered a qualitative interpretation that the activity of Cu (100) and Cu (211) is quite similar, whereas that of Cu (111) is the lowest [119], which has been previously demonstrated by H. T. Wang and coworkers [2]. Furthermore, high-index Cu crystal facets [i.e., Cu (311), Cu (511), Cu (711), and Cu (911)] tended to be highly selective for C_2H_4 and other liquid and oxygenated compounds [69, 91, 122–126], For example, Y. Huang and coworkers reported that activated Cu NWs catalysts with the Cu (511) plane ([3(100) × (111)]) stepped surface exhibit a high FE of C_2H_4 (77.40% ± 3.16%) over ~ 200 h [123]. DFT calculations revealed that the stepped surface was thermodynamically favorable for C_2 products compared with the surface of Cu (100), but unfavorable to the formation of C_1 products and H_2. Different from the plane of Cu-[n(100) × (111)] [40, 91, 101], Cu-[n(100) × (110)] ($n > 2$) facets are highly EtOH selective, while the stepped Cu(210) is more selective toward CH_4 [40, 127]. In addition, F. Jaramillo et al. demonstrated that Cu (751) over the Si (111) substrate was higher selective for > $2e^-$ oxygenate generation at low overpotentials than that of Cu (111) and Cu (100) [126]. In addition to single-crystal Cu, grain boundary (GB) Cu also presented high activity and selectivity of C_{2+} products during CO_2RR [128, 129]. For instance, Gong and coworkers reported that the GB-rich Cu could be obtained to drive a remarkable FE of 73% for C_{2+} products [130]. DFT calculations further revealed that the Σ3 twin boundary can increase the CO binding energy to improve the kinetics of CO dimerization.

It is important to determine the crystal face structure of Cu catalysts for understanding the catalytic mechanism to design new catalysts. However, Cu catalysts would not maintain a constant structure and morphology under CO_2RR operating conditions, resulting in the change of Cu lattice structure and exposure of unsaturated active sites, which has been widely studied [12, 131, 132]. For example, Kim et al. investigated the lattice structure evolution of the polycrystalline Cu electrode via operando electrochemical scanning tunneling microscopy (ECSTM) [133]. Under CO_2RR conditions with a fixed negative potential (− 0.9 V vs. SHE), the surface of polycrystalline Cu gradually reconstructed, first to Cu (111) within 30 min, then to Cu (100) after another 30 min, and remained stable after that, which was consistent with subsequent reports [134, 135]. In addition, the morphology and crystal face changes of Cu catalysts under CO_2RR operating conditions were observed by using in situ TEM, operando grazing incidence X-ray diffraction, and electrochemical atomic force microscopy [136–140]. Therefore, an in-depth understanding of the dynamic evolution of Cu catalysts can determine the true active site and further understand the relationship between structure and catalytic performance.

3 Strategies in Cu-Based Catalysts Design for CO_2RR toward C_{2+} Products

3.1 Dimension Control

The evaluation of electrocatalytic performance depends heavily on the inherent physical and chemical properties of materials, which can be fine-tuned by modifying the morphology of the material, such as its size and shape [2, 27, 34, 141, 142]. Therefore, the exploration of nanostructure is of great significance in improving the selectivity of C_{2+} products on Cu-based CO_2RR catalysts. So far, diverse morphologies have been developed for rapid CO_2RR processes. According to the spatial configurations, Cu-based nanomaterials can be classified into five categories as follows: single-atomic catalysts (SACs); zero-dimensional (0D) nanomaterials, such as metal nanoparticles (NPs) and nanoclusters; one-dimensional (1D) nanomaterials, such as nanowires (NWs), nanotubes (NT) and nanorods (NRS); two-dimensional (2D) nanomaterials, such as nanosheets (NSs); and three-dimensional (3D) nanomaterials, having nanometer sizes at different directions.

3.1.1 SACs

Due to the unique electronic structure and unsaturated coordination environment, SACs have been showed enhanced activity and unique selectivity toward CO_2 reduction into CO, CH_4, HCOOH, CH_3OH, C_2H_4, C_2H_6, EtOH, and CH_3COCH_3, respectively [143–153]. For instance, Zhao et al. [150] designed single-atom Cu on N-doped porous carbon catalysts for reducing CO_2 to CH_3COCH_3 as the major product (FE 36.7%) with a production rate of 336.1 μg h^{-1} in Fig. 1a. DFT calculations revealed that the active site of single Cu with four N atoms reduces the activation energy of CO_2 and the reaction free energy of C–C coupling (Fig. 1b). However, Karapinar et al. [145] suggested that single Cu sites were converted into very small Cu NPs by using the operando XAS experiment during CO_2RR, which is likely to be the catalytically active species, displaying a unique EtOH selective with the FE of 55%. In addition, Qiao's group [147] developed a Cu-C_3N_4 complex with dual active centers for reducing CO_2 into C_2 (C_2H_5OH, C_2H_6, and C_2H_4) species. DFT computations revealed that g-C_3N_4 framework could not only provide additional active centers, but also effectively uplift the d-band center of Cu toward the Fermi level to enhance the adsorption strength of the intermediates during CO_2RR.

3.1.2 0D structure

Differing from bulk Cu-based materials, 0D nanomaterials can provide a higher electrochemical surface area to enhance

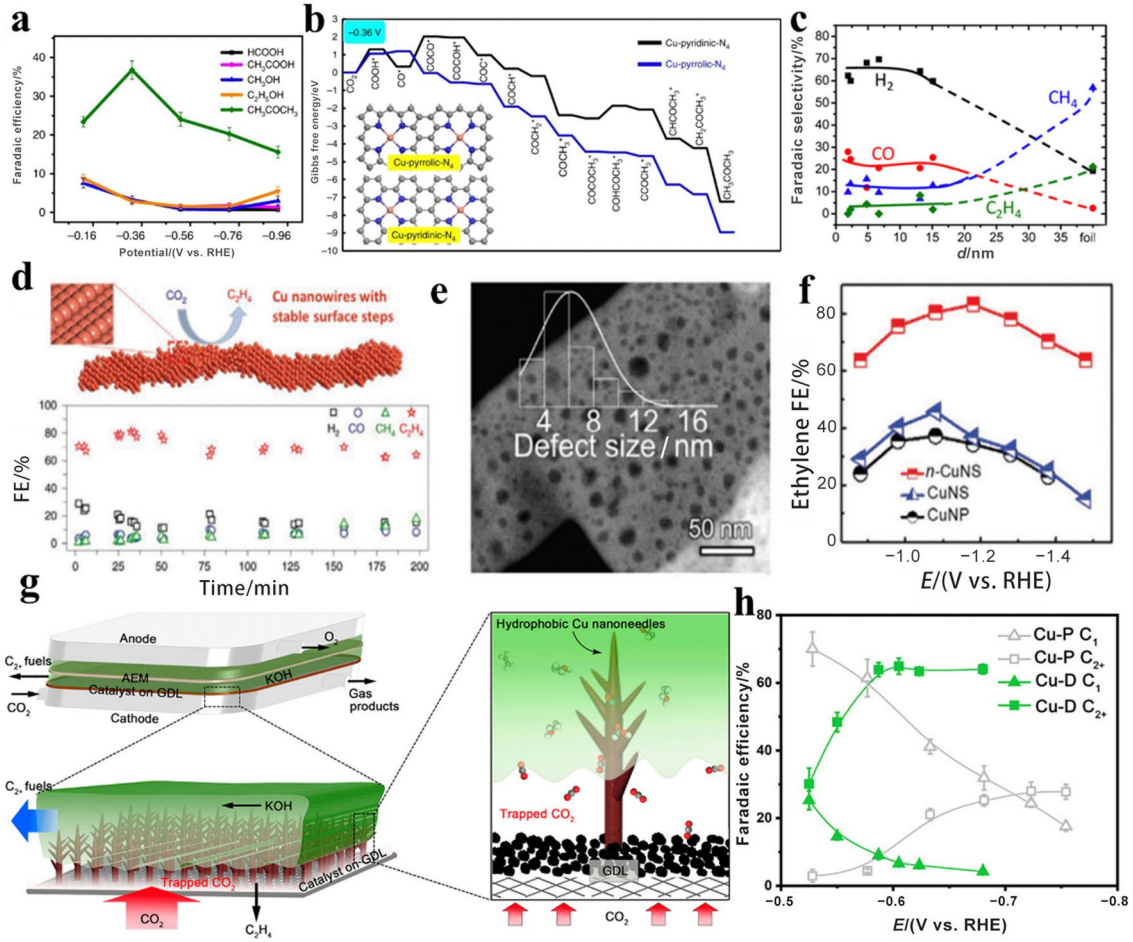

Fig. 1 **a** FEs of CO_2RR products on Cu-SA/NPC. **b** Free energy diagrams CO_2 reduction to CH_3COCH_3 on two types of Cu-SA/NPC. Reproduced with permission from Ref. [150]. Copyright © 2020, Springer Nature. **c** FEs of reaction products during CO_2RR on Cu NPs. Reproduced with permission from Ref. [157]. Copyright © 2014, American Chemical Society. **d** Schematic illustration of Cu NWs with stepped surface and its FE of reaction products during CO_2RR. Reproduced with permission from Ref. [123]. Copyright © 2020, Springer Nature. **e** TEM images of n-Cu NSs, size histograms of nano-defects and **f** the FE of C_2H_4 for n-Cu NS, Cu NS, and Cu NP. (**e**, **f**) Reproduced with permission from Ref. [175]. Copyright © 2020, American Chemical Society. **g** Illustration of the microfluidic CO_2 flow cell (left) and the hierarchical electrode design (right). **h** C_{2+} and C_1 FEs on Cu-D and Cu-P electrodes. (**g**, **h**) Reproduced with permission from Ref. [185]. Copyright © 2021, American Chemical Society

the activity and selectivity of Cu-based catalysts during CO_2RR. Combined with theory and experiment, ~ 2 nm metallic Cu clusters have been demonstrated to be active sites for the high selectvity of CH_4 due to the increased adsorption strength of CO intermediate and the reduced energy barrier of the CO → CHO* step with decreasing particle size during CO_2RR [154–156]. Differing from Cu clusters, Cu NPs produced CH_4 and C_2H_4 as the predominant hydrocarbon product from CO_2RR [4, 117]. For example, the catalytic activity and selectivity of H_2 and CO were significantly increased for Cu NPs with the decrease in Cu NP size, particularly for NP size below 5 nm, while the selectivity of CH_4 and C_2H_4 was inhibited (Fig. 1c) [157]. Huang and coworkers [158] reported a high-yield synthesis of unique star decahedron Cu NPs, which included a large number of surface defects, twin boundaries, tension strains, and multiple stacking faults. This unique structure led to lower overpotentials by 0.149 V for CH_4 than commercial Cu NPs and high FE of (52.43% ± 2.72%) for C_2H_4 production at (− 0.993 ± 0.012 9) V_{RHE}. DFT calculation revealed that the existence of twin boundaries significantly reduced the energy barrier of *CHO at low overpotential to promote the generation of CH_4, while at high overpotential the lower formation energy of *OC–CHO was more conducive to the formation of C_2H_4. Anna et al. [159] synthesized three different sizes of Cu NC cubes (24, 44, and 63 nm), in which the cubes with side length of 44 nm showed the highest activity and selectivity toward CO_2RR (FE_{CO_2RR} = 80%) with a 41% FE for C_2H_4. However, the ratio of selectivity for C_2H_4 and CH_4 increased with the increase in cube size. This result indicated that an optimal ratio of edge sites over (100) plane-sites played a key role in maximizing C_2H_4 selectivity and the activity of CO_2RR. As discussed above, the size of NPs has an effect on CO_2RR selectivity. With the size of NPs increases, the relative atom number on the corners and edges decreases, which is not conducive to the formation of CH_4, while the increase in atomic numbers in the plane promotes the formation of C_2H_4. In general, the selectivity of C_2H_4/CH_4 increases with the increasing size of NPs.

3.1.3 1D structure

Compared with 0D electrocatalysts, 1D nanostructures are beneficial for exposing the specific crystal plane, improving the electron transport performance, and maintaining long-term durability due to the preferential crystal growth and no defects on the surface. Various NWs electrocatalysts including powder and self-supporting NWs have been designed and the mechanisms have been extensively studied [123, 160–167]. Yang and coworkers [163] reported that ultrathin fivefold twinned Cu NWs exhibited high CH_4 selectivity with trace amounts of C_2H_4 due to the existence of the high-density twin boundary edge during CO_2RR. In addition, Sun's group [160] reported 50 nm Cu NWs with especially selective for CO reduction into C_2H_4 and C_2H_6. Furthermore, Huang's group [123] reported that Cu NWs with highly active stepped surfaces by in situ electrochemical activation demonstrate a remarkable FE of C_2H_4 (> 70%) and exceptionally high stability over 200 h (Fig. 1d). DFT studies reveal that the stepped surface was in favor of C_2 products compared with the Cu(100) surface and revealed a higher barrier for the C_1 pathways and HER. Similarly, Xia's group [162] demonstrate that partially oxidized Cu NWs achieve an FE as high as 57.7% for C_2H_4 at − 1.0 V_{RHE}, which can be mainly due to the rough surface and the presence of defective sites and cavities.

Differing from powder NWs, the main products self-supporting NWs were complex, such as CO [168–172], CH_3OH [173], C_2H_4 [164], C_2H_5OH [164], C_2H_6 [165], and PrOH [166], which may result from differences in the length and density of Cu NWs. For example, Ma et al. synthesized Cu NWs array electrodes with different lengths and densities [65]. HCOOH formation can always be detected, while PrOH was observed on Cu catalysts with NWs length not less than (2.4 ± 0.56) mm. As the length of Cu NWs increased, the formation of C_2H_6 (FE = 2%) with a small amount of EtOH was observed. They proposed a formation route of C_2H_6 through the intermediate (CH_3CH_2O) in the CO–CO pathway. More importantly, with the increase in Cu NWs length and density, the local pH value increased, which can enhance CO–CO coupling to promote the formation of C_2H_4.

3.1.4 2D structure

Compared with bulk structures, 2D nanomaterials have larger specific surface area to expose specific crystal faces and facile electron and/or ion transfer properties, which are conducive to improving activity and selectivity of CO_2RR [40, 174–176]. For instance, Zhang and coworkers designed Cu NSs with defects at the nanoscale (2–14 nm) for CO_2RR into C_2H_4 in Fig. 1e [175]. Experimental and DFT calculation results reveal that highest FE of C_2H_4 FE (83.2% in Fig. 1f) with a current density of ~ 60 mA cm^{-2} at − 1.18 V_{RHE} was attributed to enhanced adsorption of reaction intermediates and hydroxyl ions on the surface of nano-defective structure to synergistically promote C–C coupling for C_2H_4 formation. In addition, Kang' group [176] reported that the Cu NSs exhibit a higher acetate FE (48%) with a partial current density of 131 mA cm^{-2} during CORR. Further analysis suggested that the reduction of exposed (100) and (110) surfaces inhibited the formation of C_2H_4 and EtOH to enhance acetate selectivity.

3.1.5 3D structure

Similar to self-supported NWs, the major products of 3D nanostructure were complex, such as CO [177], HCOOH [67], C_2H_4 [178, 179], EtOH [180], C_2H_6 [181, 182], and PrOH, which may result from the influence of local pH, retention time of the intermediate, gas permeability or liquid diffusion. For instance, Broekmann and coworkers [181] prepared mesoporous Cu foam with C_2 (C_2H_4 and C_2H_6) FE reaching 55% at − 0.8 V_{RHE}. The systematic CO_2 electrolysis study shows that the surface aperture with moderate pore size was beneficial to improve the FE of C_2 by providing more available C–C coupling sites and increasing the retention time of the intermediate (in particular CO and C_2H_4). In another study, Broekmann's group [179] also found that μm-sized pores on a 3D skeleton structure could capture the reaction intermediates (e.g., C_2H_4) more effectively and promote the complete reduction of C_2 products. In addition, the main product of Cu nanofoam with pore sizes prepared by Sargent was C_2H_4 [178].

Apart from micron-sized pores, nano-porous structures could also increase the local pH value and prolong the retention time of intermediates to enhance C_2 selectivity [182]. Cu mesopore electrodes with the precise adjustment of the pore widths and depths were synthesized by sputtering Cu on anodized aluminum oxide. In general, the FE of C_2 products increased with the decrease in hole width and depth, whereas that of the C_1 products was decreased. As the pore width was reduced from 300 to 40 nm with the hole depth 40 nm, the FE of C_2H_4 was increased from 8% to 38%. Interestingly, when the pore depth is increased from 40 to 70 nm with the hole width 40 nm, the main C_2 product was converted to C_2H_6 with an FE of 46%. Though the effect and mechanism of different morphologies on the activity and selectivity of CO_2RR are different, the morphologies with more edges, edges, or sharp tips seem to be more conducive to promoting C_{2+} products, such as nano-dendrite [183, 184]. Recently, Gao et al. reported a 3D bionic Cu catalyst on GDL, which mimicked the unique hydrophobic structure of Setaria's leave (Fig. 1g) [185]. This unique structure was conducive to the establishment of a gas–liquid–solid triple-phase boundary. The experimental results showed that hierarchical Cu structure achieved high FE (64% ± 1.4%) of C_{2+} products with a current density of (255 ± 5.7) mA cm^{-2} (Fig. 1h), as well as excellent stability over 45 h in the flow reactor at 300 mA cm^{-2}, which greatly exceeded the performance of the wettable Cu electrode.

3.2 Oxide-Derived Cu

Recently, oxide-derived catalysts have attracted widespread attention for CO_2RR. Various oxide-derived metal electrocatalysts, including Au, Ag, Co, Sn, In, and Cu, have been prepared and their mechanisms have been studied in detail. The high selectivity and stability of oxide-derived Cu-based catalysts mainly possess beneficial properties such as the low-coordinated [169, 171, 186], metallic Cu^0 atoms [66, 69, 187–189], Cu^+/Cu^0 site [190], Cu^+ site [35, 184, 191, 192], increased grain boundaries [68, 193–197] and subsurface oxygen [198, 199]. Although the actual active site is still debated, OD-Cu has shown excellent performance in reducing the required overpotential and improving selectivity. Oxide-derived Cu-based catalysts were prepared by annealed, electrochemical, and plasma. In this section, the selectivity of C_{2+} products on oxide-derived Cu-based electrocatalysts will be described in detail as followed.

3.2.1 Annealed/OD-Cu

Annealing is a convenient and useful way to improve the activity and selectivity of Cu-based catalysts, which is affected by the temperature and the corresponding gas atmosphere during CO_2RR or CORR. For example, W. Li et al. reported OD-Cu electrodes prepared by annealing in air at 500 °C [193], which produces EtOH and HAc with the FE of 57% at modest potentials. In addition, by using the TEM nano-diffraction analysis and temperature-programmed desorption (TPD) experiments [194], they found that the grain boundary density of OD-Cu and the CO binding sites decreased with increasing annealing temperature in N_2 (Fig. 2a, b). They concluded that the active sites on the surface of OD-Cu, especially strong binding sites of *CO, were supported by grain boundaries. To quantify the effect of GBs during CORR [195], they prepared five electrodes by depositing Cu on carbon nanotubes with different annealing temperatures in N_2. With the increase in annealing temperature, the amount of GBS in Cu NPs decreases gradually, confirmed by TEM. The activity was linearly related to the density of GBs (Fig. 2c), indicating that GBs were responsible for creating the vast majority of the active surfaces.

Interestingly enough, the major product was EtOH rather than C_2H_4 on OD-Cu prepared by annealing in air [74, 186, 193, 194, 200]. Apart from annealed Cu foil, Wang and coworkers reported CuO nanowires obtained by annealing in air for 8 h [186], in which the optimized Cu nanowires achieved 50% FE toward production of EtOH for CORR. By combining structural analysis and DFT calculations, the high FE of EtOH be related to the unsaturated (110) surface sites on the Cu NWs. Furthermore, the FE of EtOH was higher than C_2H_4 on the Cu foil annealed in air at 500 °C during CO_2RR and CORR [200], while that of C_2H_4 was higher on the surface of Cu (100), Cu (111), and polycrystalline Cu. In addition, the main products on annealed Cu electrocatalysts for CO_2RR were CO or HCOOH [68, 169, 171, 201]. The total FE of CO and HCOOH increased with the increase in annealing temperature in air [68], while this was opposite in

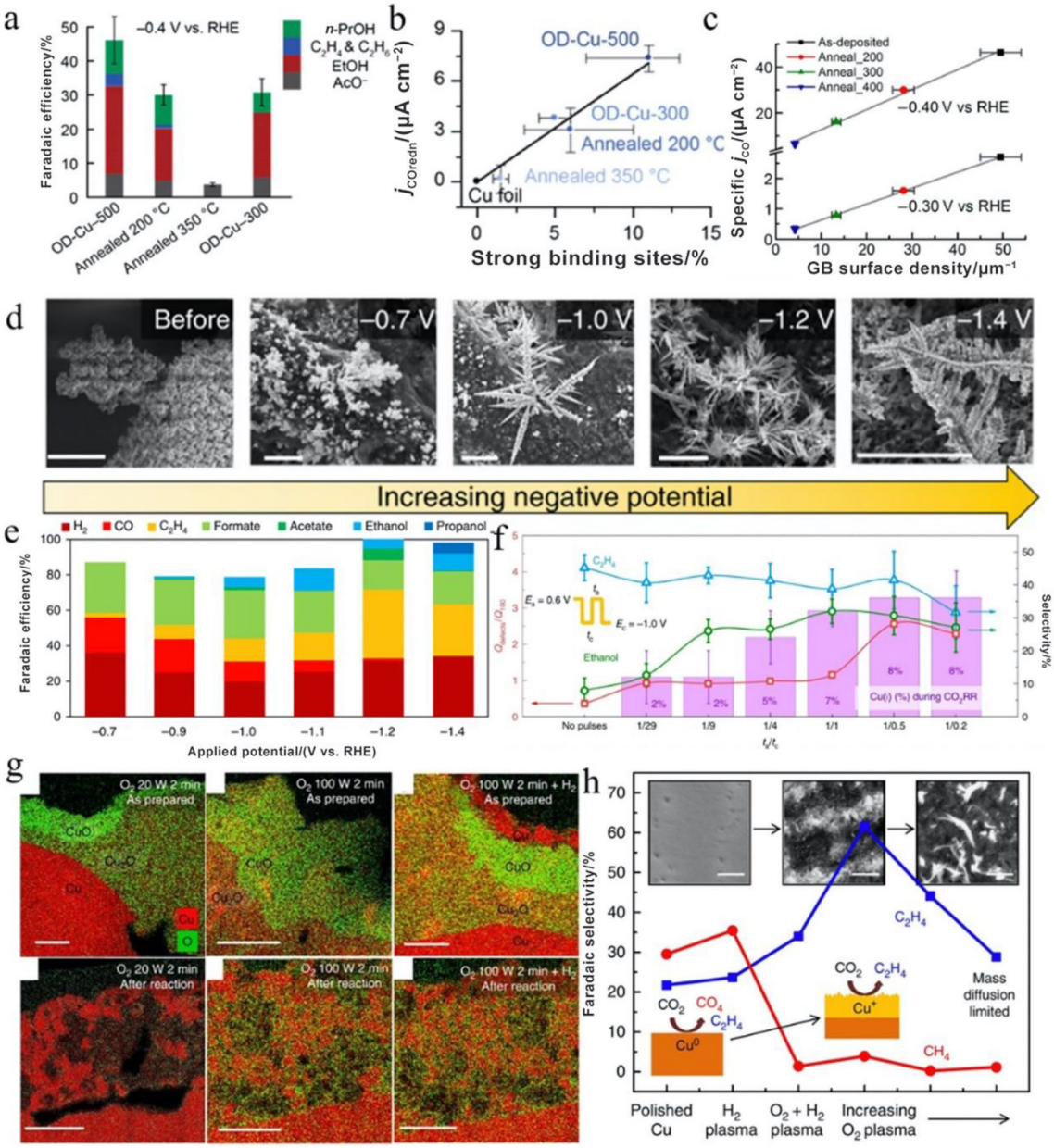

Fig. 2 **a** FEs for CORR in 0.1 M KOH. **b** Surface-area corrected j_{CO} at − 0.4 V_{RHE} versus the percentage of binding sites. (**a**, **b**) Reproduced with permission from Ref. [194]. Copyright © 2015, American Chemical Society. **c** Correlation between j_{CO} and GB surface density. Reproduced with permission from Ref. [201]. Copyright © 2015, American Chemical Society. **d** SEM images with a scale of 5 μm at different applied potentials after at least 1 h of reaction. **e** FEs of CO_2RR products on ERD Cu. (**d**, **e**) Reproduced with permission from Ref. [184]. Copyright © 2020, Springer Nature. **f** $Q_{defects}/Q_{100}$ and product selectivity as a function of t_a/t_c applied. Reproduced with permission from Ref. [127]. Copyright © 2020, Springer Nature. **g** EDS maps of Cu foils treated with O_2 plasma for 20 W 2 min, 100 W 2 min, and 100 W 2 min + H_2 plasma. **h** Summary of hydrocarbon selectivity of plasma-treated Cu foils at − 0.9 V_{RHE}. (**g**, **h**) Reproduced with permission from Ref. [35]. Copyright © 2016, Springer Nature

5% H_2/Ar [169, 171]. Wang and coworkers systematically studied CO_2 reduction on high-density Cu NWs, in particular the surface structure effects on the formation of *CO. They proposed a structure–property relationship between highly dense nanowires and identified open facets [e.g., (110) and reconstructed (110)], which may be the active sites for CO_2 reduction into CO at the low overpotentials.

3.2.2 Electrochemical/OD-Cu

Different from the annealed/OD-Cu, the electrochemical/OD-Cu showed higher FE of hydrocarbons than that of multi-carbon oxygenates [66, 70, 77, 184, 192, 202], including electrodeposition and anodizing, which could also promote activity and selectivity of C_{2+} products during CO_2RR. For instance, Sargent and coworkers [184] synthesized Cu nano-dendrites by electro-redeposition with a C_{2+} FE of ~ 73% (~ 45% C_2H_4, 22% EtOH, 9% PrOH) in Fig. 2d, e. They attributed the enhanced selectivity to the increased local pH and the presence of Cu^+ at negative potentials. In addition, the electrodeposition of dendritic Cu resulted in the CO_2RR product selectivity toward C_2H_4 (FE = 34.3%) without multi-carbon oxygenates [77], while the thermal annealing treatment of dendritic Cu directed the CO_2RR product selectivity toward EtOH and PrOH (FE_{total} = 24.8%), which was higher that of C_2H_4. They proposed that the generation of hydrocarbon on the surface of electropolished Cu relied on a coupled C_1/C_2 reaction pathway that shares common intermediates such as *COH and $*CH_2$, whereas that on the annealed Cu catalyst depended on the CO–CO coupling pathway. However, they also reported that both annealed and electrodeposited Cu skeleton catalysts showed profound selectivity toward C_2H_4 and C_2H_6 [179], which suggested that this preference was related to the presence of (100) textured Cu. More importantly, Ren et al. found that the FE of C_2H_4 and EtOH can be systematically regulated by altering the thickness of the deposited overlayers [202].

Interestingly, on the electrodeposited/OD-Cu, the highest FE of C_2 products corresponds to potential in the range of − 0.9 to − 1.2 V_{RHE}, indicating that the formation of hydrocarbon products on the electropolished Cu is more likely to depend on the intermediates of *CHO or *COH rather than CO–CO coupling. Therefore, both CH_4 and C_2H_6 were observed [66, 70, 77, 179, 192, 202]. In particular, the FEs of CH_4 on the electrodeposited Cu electrodes were 55% and 59% [192, 202], respectively. Similar to the electrodeposited Cu, the peak potential of the highest FE of C_2 products on the anodized OD-Cu also located on the higher potential [42, 127, 140, 203, 204]. For example, by tuning the applied pulse potential [127], the surface structure and composition of Cu catalyst can be adjusted simultaneously during CO_2RR. The evolution of morphology was detected by using cyclic voltammetry and in situ atomic force microscopy, and the chemical states on the surface of catalysts were detected by quasi-in situ XPS. The results established a correlation between increased C_{2+} products (76% at − 1.0 V_{RHE} in CO_2-saturated 0.1 M $KHCO_3$ solution) in Fig. 2f and the presence of Cu (100) steps, Cu_2O and Cu (100) defects, which synergistically promoted C–C coupling.

3.2.3 Plasma/OD-Cu

Oxygen plasma treatment is a simple and scalable technique for rapidly changing the chemical state, tunning morphology, creating defects, and embedding atoms on catalyst surfaces at room temperature, which has been used to enhance activity and selectivity of CO_2RR [35, 191, 205]. For example, Mistry et al. showed that oxygen plasma-activated OD-Cu catalysts enabled a higher C_2H_4 selectivity (> 60%) than other plasma-treated Cu foils at − 0.9 V_{RHE} by suppressing CH_4 formation (Fig. 2 h) [35]. Combined STEM–EDS and operando XAFS, Cu^{2+} are found to be reduced quickly, while Cu^+ species were remarkably resistant to reduction and remained on the surface during CO_2RR in Fig. 2g, which played a key role for CO_2RR into C_2H_4. Later, Gao et al. conducted plasma-activated Cu NCs catalyst with a tunable (100) facet and ion (O^{2-} and Cl^-) content [191], which exhibited drastically FE of ~ 45% for C_2H_4 and ~ 22% for EtOH with current density of ~ 35 mA cm^{-2} at − 1.0 V_{RHE}. By combining STEM–EDS results with in situ XPS, they proposed that the presence of surface and subsurface oxygen species was the key of affecting the binding of CO and Cu to achieve high activity and C_{2+} products selectivity. In addition, they also reported that O_2-plasma-treated Cu foil exhibited drastically FE of ~ 58.9% for C_{2+} products with current density of ~ 38 mA cm^{-2} at − 1.0 V_{RHE} [205].

Recently, Scholten et al. prepared a series of well-oriented Cu (100) and Cu (111) single-crystal catalysts to determine the real catalytic active site [140]. All samples were first initially prepared via sputtering in an ultra-high vacuum (UHV), and then treated by Ar sputtering, O_2 Plasma, and electropolishing treatment, respectively. DFT calculations predicted that the single-crystal Cu electrode will generate hydrocarbon products, but their experimental results showed that well-oriented Cu single-crystal catalysts treated by UHV with atomically ordered arrangement generated H_2 during CO_2RR. Only electropolished and O_2-plasma-treated Cu catalysts produced significant amounts of hydrocarbons. The quasi-in situ XPS results ruled out the effect of the oxidation state or the presence of subsurface oxygen in the treated Cu catalysts on the different selectivity trends. ECSTM images confirmed the existence of step edges/bunches on the surface of treated Cu catalysts.

3.3 Organics Decoration

Organic molecule modification of Cu-based catalysts can not only improve the activity and selectivity of C_1 products (e.g., CO and HCOOH) [206–208], but also improve that of C_2 products (e.g., C_2H_4 and EtOH) [28, 141, 209]. Due to the interaction between organic groups and intermediates, the surface modification by organic molecules played an important role in regulating the electronic structure of

Cu, changing the morphology, or affecting binding strengths of intermediates. For example, amino acid modifier was an effective way to dramatically enhance the FE of hydrocarbons on Cu electrodes during CO_2RR. Wang and coworkers for the first time reported that various amino acids (i.e., glycine, dl-alanine, dl-leucine, dl-tyrosine, dl-arginine, and dl-tryptophan) were used as surface additives on Cu electrodes [210], and found that amino acids containing –COOH and $–NH_2$ functional groups enhanced the hydrocarbon selectivity, while that could be weakened by using additives in the absence of –COOH or $–NH_2$. In particular, glycine-modified Cu NWs films, only containing –COOH and $–NH_2$ functional groups, provided higher hydrocarbon FE of 34.1%, nearly twofold than that of the bare Cu NWs films. Combining theoretical calculations with experimental observations, they concluded that both –COOH and $–NH_2$, especially $–NH_2$, could stabilize *COOH and *CHO intermediates to promote the formation of hydrocarbon. Moreover, a volcano-type dependency of hydrocarbon selectivity upon the amount of glycine modifier suggested that too high Glycine coverage may block active catalytic sites and inhibit CO_2RR.

Similar to amino acids, polyacrylamide (PAM)- or polyaniline (PANI)-modified Cu also stabilizes intermediates to improve selectivity of C_2 products due to the presence of $–NH_2$ functional group [206, 211, 212]. Sunyhik et al. reported that the Cu foam modified by PAM can double the FE of C_2H_4 as compared to unmodified foam (Fig. 3a, b) [211]. According to DFT calculations, PAM not only donates charge to the Cu surface through the Cu–O bond

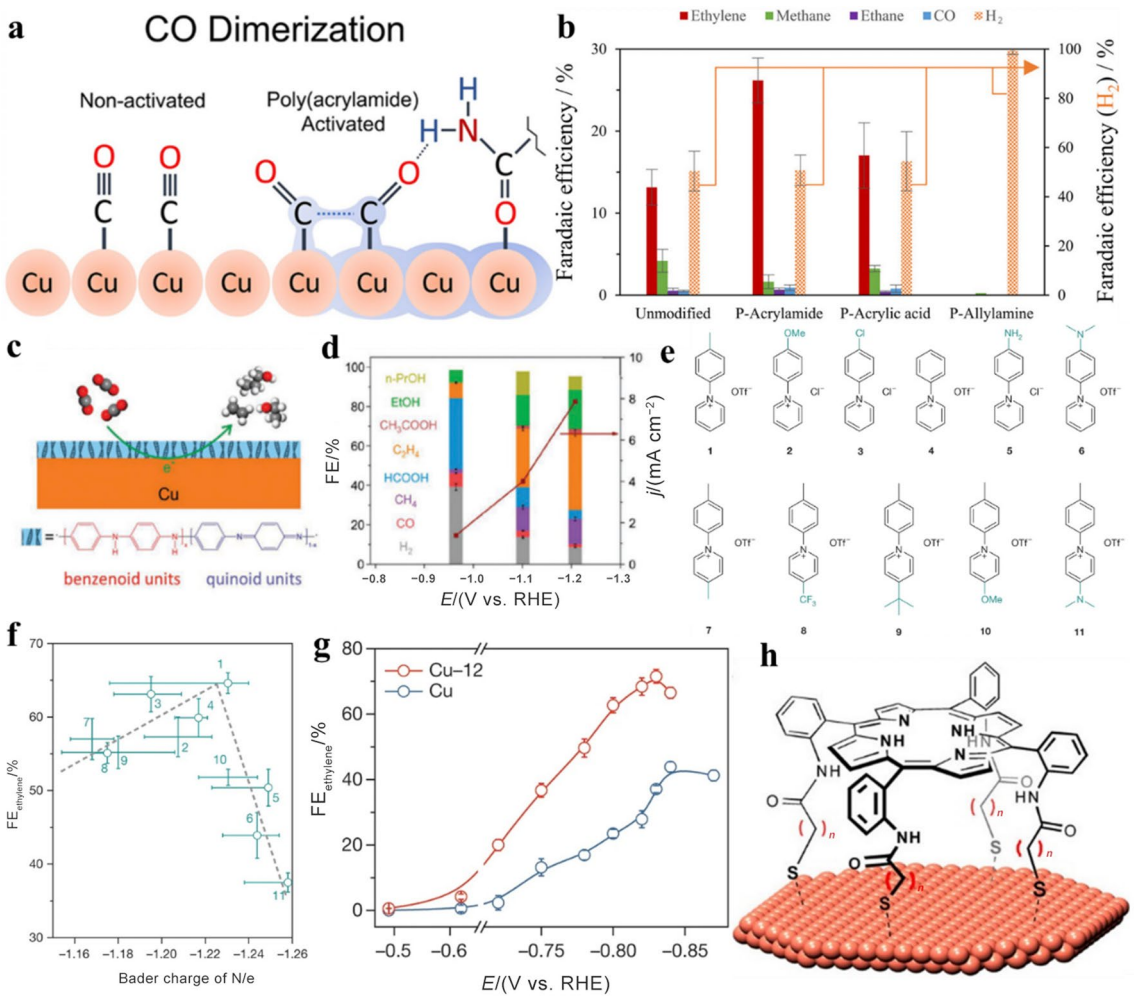

Fig. 3 **a** A schematic of CO–CO coupling for Cu with or without poly(acrylamide) modification. **b** Bar chart of FEs of Cu foams for CO_2RR without treatment and with modified with poly(acrylamide). (**a**, **b**) Reproduced with permission from Ref. [211]. Copyright © 2018, American Chemical Society. **c** Schematic illustration of Cu-PANI electrode and **d** its FE of CO_2RR products and current density. (**c**, **d**) Reproduced with permission from Ref. [214]. Copyright © 2020, American Chemical Society. **e** Molecular structures of additives 1–11. **f** Trend for C_2H_4 FE and calculated Bader charge. **g** FE of C_2H_4 on Cu and Cu-12. (**e**–**g**) Reproduced with permission from Ref. [217]. Copyright © 2020, Springer Nature. **h** Schematic illustration of free-base porphyrins possessing different linker lengths. Reproduced with permission from Ref. [219]. Copyright © 2017, American Chemical Society

between Cu surface and its carbonyl group to activate CO for dimerization, but also stabilized the CO dimer intermediate via H bond due to the presence of $–NH_2$ functional group. Gewirth, A. and coworkers reported a Cu-polyamine hybrid catalyst through the co-electroplating scheme with the FE (87% ± 3%) for C_2H_4 at − 0.47 V_{RHE} [213]. The SERS results indicated that the higher CO_2RR activity toward C_2H_4 resulted from higher surface pH, higher CO content, and higher stabilization of intermediates on the Cu-polyamine electrode. Zhuang and coworkers reported a Cu/PANI interface by coating a PANI solution on Cu foil and the FE of C_{2+} products was increased from 15% to 60% (Fig. 3c, d) [214]. This excellent performance was attributed to an improvement in the coverage of *CO by using IR spectroscopy.

Apart from the amines-containing molecules, pyridinium and benzimidazole (BIMH) were also employed as the competent modifiers to stabilize key reaction intermediate on the catalyst surface for selectivity escalation [215–217]. For instance, Han et al. reported that the selectivity of C_{2+} products can be tuned from 26.0% to 76.1% via electrochemical coupling of *N*-aryl pyridinium on the polycrystalline Cu [216]. Strikingly, H. Sargent and coworkers proposed a strategy to stabilize the intermediate during CO_2RR through the introduction of a series of N-substituted pyridinium-based molecules on the surface of Cu (Fig. 3e) [217]. By quantifying the CO configurations through in situ SERS, they found that the ratio of atop-bonded CO (CO_L) to bridge-bonded CO (CO_B) was positively correlated with the Bader charge of nitrogen atoms. A volcano-shaped relationship was observed between the FE of C_2H_4 and nitrogen Bader charge (Fig. 3f). Therefore, the pyridinium additives-modified Cu has moderate electron donation capacity to reach the optimal FE of C_2H_4, achieving a C_2H_4 FE of 72% (Fig. 3g). In addition, Zhong et al. reported BIMH-modified Cu foil, which can directly convert CO_2 to C_{2+} products with the FE of ~ 77% through enhancing formation of *COOH, verified by DFT simulations [215]. In particular, in addition to C_2H_4, molecular modifications have also been favorable for the generation of EtOH [218, 219]. Sargent et al. reported a CO_2-to-EtOH conversion with an EtOH FE of 41% at 124 mA cm^{-2} by functionalizing the surface of Cu with porphyrin-based metallic complexes (FeTPP[Cl]) [218]. Compared to bare Cu, the local concentration CO on FeTPP[Cl]/Cu obviously improved based on Raman spectroscopy analysis. DFT calculations further indicated that higher local CO coverage contributed to C–C coupling and led the reaction toward EtOH. In addition, Gong et al. presented a modular synthetic approach via self-assembly of supramolecular iron porphyrin with a terminated thiol group bound to the Cu surface (Fig. 3h), achieving up to 57% EtOH FE during CORR [219].

In addition to stabilize intermediates and reduce the energy barrier of C–C coupling, *N*,*N*′-ethylene-phenanthrolinium dibromide (1-Br_2), and ethylenediaminetetraacetic acid disodium salt (EDTA-2Na) were beneficial for tuning the morphology of electrodes [220, 221]. Herein, Thevenon et al. reported a convenient method for fabricating of nanostructured Cu cube using 1-Br_2 as a molecular additive [220]. The FE of C_{2+} products was as high as 70%, and the surface morphology remained unchanged over 40 h. Mechanistic studies revealed that the protective organic layer formed by its dimerization not only kept the stable long-time electrocatalysis, but also promoted the FE of C_{2+} products. Liu et al. constructed porous hollow Cu microspheres (H-Cu MPs) by using the method of EDTA-2Na-assisted electrodeposition [221]. The synthesized H-Cu MPS was spherical and uniformly dispersed, while Cu-Poly without EDTA-2Na presented a block-like morphology, which led to a double increased C_2H_4 FE from 23.3% to 50.1%. DFT calculations revealed that the adsorbed EDTA anions regulated the morphology, but also reduced the formation energy of the dimer to increase yield of C_2H_4.

3.4 Halogen Incorporation

Compared to oxygen, the effect of halogen ions (right next to the oxygen family), particularly F, Cl, Br, and I, has also been investigated and halide-derived Cu-based electrocatalysts showed extraordinary activity and selectivity of C_{2+} products for CO_2RR. Although the mechanism of the effect of halide-derived Cu was complex and contradictory, it mainly focused on the construction of unique Cu nanostructures or specifically adsorbed halogen ions on the surface of Cu. In earlier studies, the halide-assisted reconstruction resulted in nanostructure Cu to explore more (100) planes at surfaces, resulting in a significant increase in C_2 products selectivity [110, 119, 196, 205, 222, 223]. Recently, Hu and coworkers [71] present a wet chemistry strategy to prepare a series of well-defined cuprous halide (e.g., CuCl, CuBr, and CuI) microcrystals in Fig. 4a. Interestingly, I-derived Cu nanofibers showed a particular selectivity toward C_2H_6 at a low-overpotential and dendritic Cu from Br reduction dominantly presented a favorable formation of C_2H_4 at large overpotential, which all favor the higher selectivity of C_{2+} products, whereas Cl-derived Cu NCs manifest being more favorable for the selectivity of CO and HCOOH in a wide range of applied potential. Their findings revealed that the morphology effect of halide-derived Cu was regarded as the main factor affecting the selectivity of CO_2RR products. Similarly, Kim et al. [224] prepared Cu-halide-derived catalysts with different nanostructures by using anodic halogenation. For all Cu-halide-derived catalysts, CO and HCOOH are subject to form at a low overpotential, while C_2 products gradually become predominant with C_2H_4 as the major product and a small amount of C_3 products gradually form when the potential turns more negative. The higher C_{2+} products

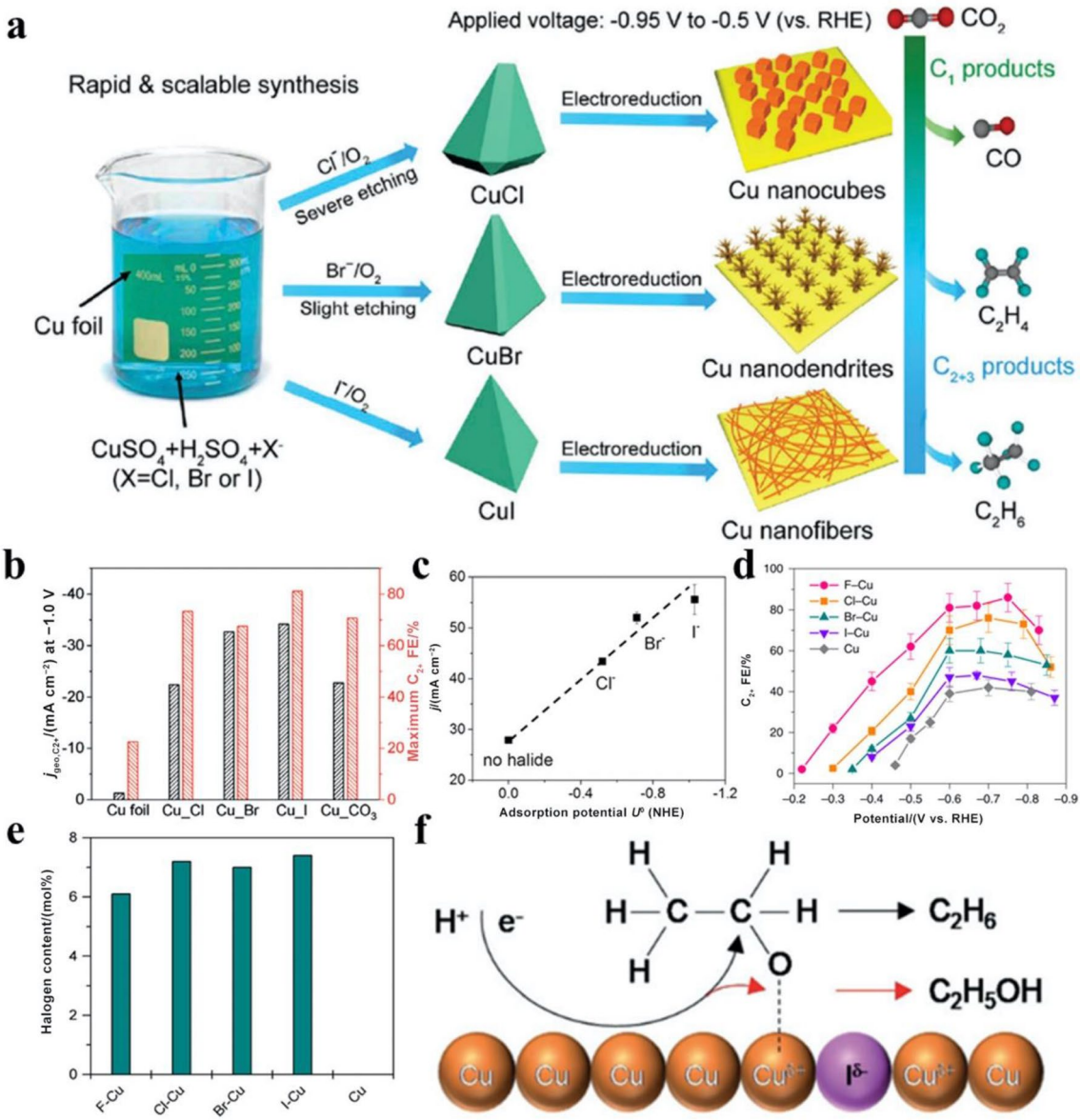

Fig. 4 **a** Schematic illustration of the synthesis of CuCl, CuBr, and CuI and the Cu nanostructure via electrochemical reduction. Reproduced with permission from Ref. [71]. Copyright © 2019, American Chemical Society. **b** Total FEs and partial current density of C_{2+} products. Reproduced with permission from Ref. [225]. Copyright © 2019, Wiley. **c** Correlations between current density and halide adsorption potential. Reproduced with permission from Ref. [205]. Copyright © 2017, American Chemical Society. **d** The FEs of C_{2+} products over X-Cu catalysts. **e** Bulk halogen contents determined by EDX. (**d**, **e**) Reproduced with permission from Ref. [62]. Copyright © 2020, Springer Nature. **f** EtOH and C_2H_6 reaction pathway outlining the selectivity determining $*OCH_2CH_3$. Reproduced with permission from Ref. [73]. Copyright © 2020, Wiley

were attributed to the high density of defect sites that promote C–C coupling and low roughness that inhibits HER.

Apart from the construction of unique Cu nanostructures, the presence of residual halides can enhance activity and selectivity of C_{2+} products during CO_2RR. For instance, Gao et al. [225] reported that the presence of residual halides reduced the overpotential and increased the rate of C_{2+} products in Fig. 4b. This enhancement effect increased with the increase in halide ions adsorption capacity ($I^- > Br^- > Cl^-$) by combining the trend of CO_2 electroreduction performance with XPS characterizations, which was consistent with his recent research (Fig. 4c) [205, 226]. Furthermore, Wang and coworkers confirmed that F^- existed on the surfaces of these catalysts by XPS characterizations, whereas Cl^-, Br^- or I^-species were detected [62]. The FE and normalized formation rates of C_{2+} products increased in the sequence of no halide < I < Br < Cl < F at all corresponding potentials (Fig. 4d), which was attributed to the difference of CO

adsorption energy caused by halogen electronegativity and H_2O activation energy. The surface contents of halogens in the X-Cu (where X = F, Cl, Br, or I) catalysts measured by XPS were ~ 6 mol% (mol% means the molar percentage) (Fig. 4e) higher than their bulk contents (~ 2 mol%). Different from the research of Gao and coworkers, Wang proposed that it was difficult to disentangle the intrinsic effort of halide species due to the different catalyst morphologies.

So far, the mechanisms and products of halide-derived Cu-based catalysts are chaotic for CO_2RR. Qiao and coworkers [73] reported I-derived Cu using calcination and subsequent electrochemical reduction, which exhibited significantly greater C_2H_6 selectivity than C_2H_4 and EtOH (Fig. 4f). By combining with in situ XAS and Raman spectrum, they found experimentally for the first time that the generation of C_2H_6 and EtOH shared the same intermediate of oxygen-bound ethoxy and the stability of the intermediate was beneficial to controlling the formation of C_2H_6. Apart from the products of C_2H_6 and EtOH, the high CH_4 selectivity of 83% and a high C_2H_4 selectivity of 93% were achieved on Cu catalysts by using the epoxide-assisted hydrolysis method with Cl^- or I^-, respectively [227]. Experiments and DFT studies show that the CO_L and CO_B on the local Cu^0/Cu^+ sites are favorable to couple into C_2H_4, whereas the CO_B on the Cu^0 sites is suitable for the hydrogenation of CH_4. It was noted that the surface contents of halogens (Cl or I) measured by XPS were not detected after electrochemical CO_2 reduction, which was consistent with previous research [71, 119, 196, 222, 223].

3.5 Cu–M Bimetallic Alloys

Cu, as a catalyst to produce C_{2+} products, has attracted the most attention due to the neither too strong nor too weak bond between *CO and Cu. Compared with pure Cu, Cu-based bimetallic catalysts have demonstrated promising results in selectively generating C_{2+} products in the past few years [228, 229]. It is generally assumed that In and Sn metals are known to mainly generate HCOOH during CO_2RR, while Au, Ag and Zn metals are more likely to generate CO [230]. Thus, Cu–M bimetallic electrodes (where M = In, Sn) maintained a higher selectivity to CO or $HCOO^-$. However, Cu–M (where M = Au, Ag, Zn) not only showed increased CO selectivity in some cases, but also have demonstrated synergistic effects, increasing selectivity of C_{2+} products [101]. In general, the CO_2RR performance of bimetallic catalysts varies with the change of composition and morphology, both of which might be modified. The products of various Cu-based alloy catalysts during CO_2RR were complex and summarized in previous reports [17, 101, 228–231], and we address recent progress on Cu-based alloy catalysts with C_{2+} products in the following sections.

3.5.1 Cu–Ag Alloys

Recently, Cu–Ag alloys system has been intensively proposed and showed enhanced CO_2RR selectivity and activity toward C_{2+} products than pure Cu. In general, the surface Cu-rich samples are preferred for C_{2+} products during CO_2RR, while that of Ag-rich is mainly CO, highlighting the importance of the metal atomic ratio in alloyed catalysts. The facilitated FE of C_{2+} products in the Cu–Ag alloys system has been usually associated with the enhanced coverage of *CO to suppress of HER, the diffusion of CO from Ag to Cu that promotes C–C coupling (CO spillover) [61, 232–238] and the optimized binding energy of reaction intermediates [23, 239–241]. For example, as shown in Fig. 5a, Gao et al. developed Cu NWs decorated with Ag islands by reducing Ag-covered Cu_2O NWs [234]. The production of CO on Ag sites led to the increase in local CO concentration to promote the formation of the C–C bond on Cu sites (Fig. 5b), which was confirmed by calculating the efficiency of CO spillover (Fig. 5c). Chen and coworker developed Ag NWs coated with various thicknesses of the OD-Cu layer via a two-step method for CO_2RR [233]. According to in situ Raman spectroscopy, the peaks greatly declined and then remained steady under − 0.55 V for 5 min in 0.1 M $KHCO_3$ due to the possible dynamic equilibrium between Cu^0 and Cu^+. Using in situ XAS, they found a strong correlation between the valence state of Cu and the distribution of products. They concluded that the CO generation can overcome the limitation of mass transport between Ag sites and nearby Cu sites to reach a high FE of EtOH. However, Cuenya et al. developed well-defined Cu_2O NCs (35 nm) uniformly covered with Ag NPs (5 nm) by reducing Ag-covered Cu_2O NCs. Compared to pure Cu_2O NCs, the FE of the Ag-covered Cu NCs electrocatalyst for C_{2+} liquid products (30%) displayed a twofold increase at − 1.0 V_{RHE} [238], while the formation of HCOOH and H_2 was inhibited. Operando XAS showed that Cu_2O NCs were partially reduced under CO_2RR conditions accompanied by the re-dispersion of Ag NPs, while the surface Cu_2O species was completely reduced through the Raman spectroscopy data. Raman spectroscopy data further revealed that the introduced Ag site caused a CO binding configuration and the significant variations of the bond between *CO and Cu sites, which were mainly caused by the Ag–Cu site, and were essential for C–C coupling. These proposed that CO spillover can effectively take place on the Ag sites near Cu, and the alloying of Cu with Ag could change the binding energy of CO to promote the generation of C_{2+} liquid products.

Apart from the effect of CO spillover, Cu–Ag alloys were beneficial to increase the binding energy of the intermediates during CO_2RR (e.g., *CO, CH_3CHO*, and *CHCHOH), which improved the FE of alcohol production. For instance, as shown in Fig. 5d, Li et al. [23] developed the bimetallic

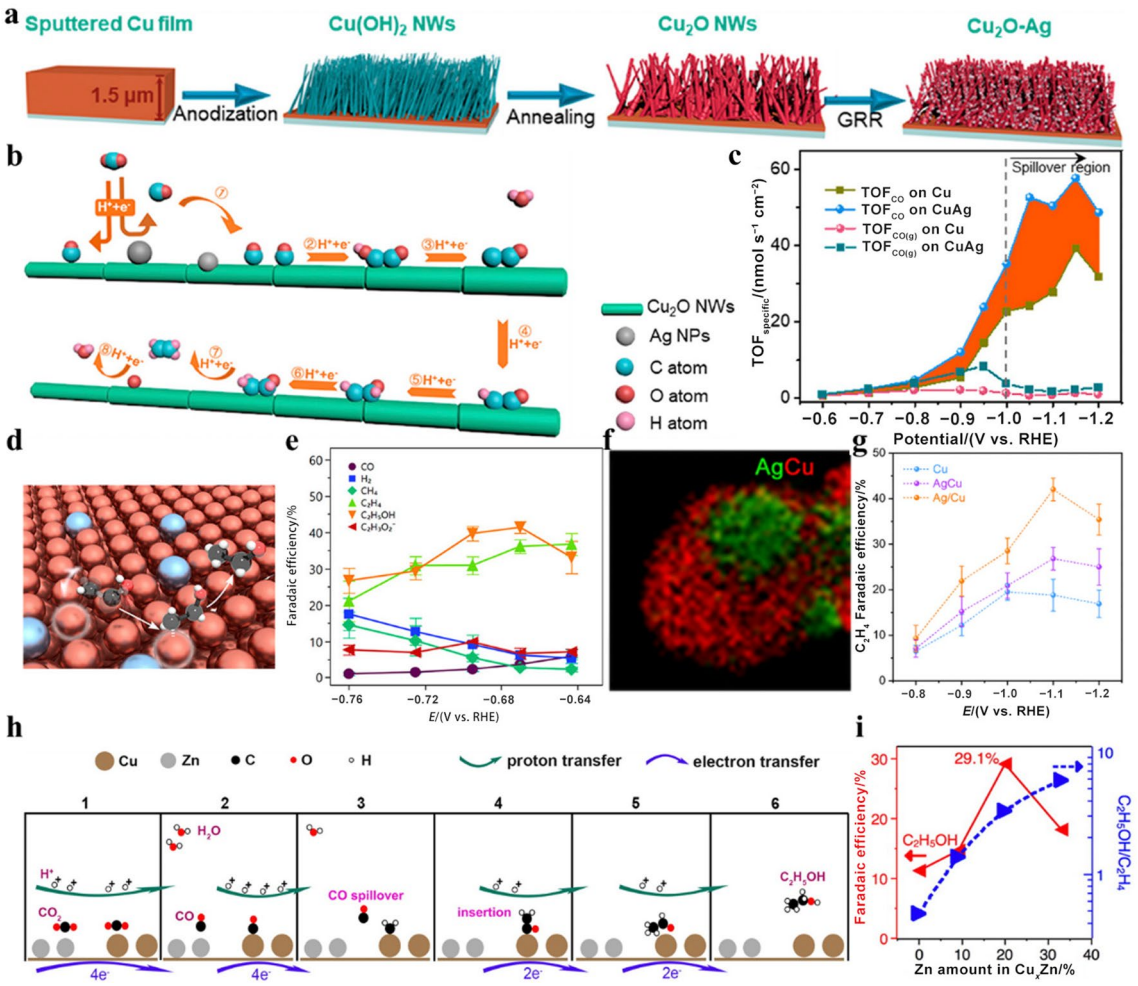

Fig. 5 **a** Presentation for the synthesis of Cu_2O and Cu_2O-Ag NWs. **b** Proposed mechanism of C_2H_4 formation on CuAg catalyst. **c** Quantitative analysis of CO generated on Ag sites. (**a**–**c**) Reproduced with permission from Ref. [234]. Copyright © 2019, American Chemical Society. **d** Binding illustration for Ag/Cu catalyst to produce EtOH and C_2H_4. **e** FEs for $Ag_{0.14}/Cu_{0.86}$ toward CO_2RR products. (**d**, **e**) Reproduced with permission from Ref. [23]. Copyright © 2019, American Chemical Society. **f** EDS mappings of Ag/Cu. **g** C_2H_4 FEs of Ag/Cu, AgCu, and Cu. (**f**, **g**) Reproduced with permission from Ref. [242]. Copyright © 2019, American Chemical Society. **h** Proposed mechanism for CO_2 reduction to EtOH on Cu_xZn catalysts. **i** FE of EtOH and the average $FE_{EtOH}/FE_{C_2H_4}$ ratio on Cu_xZn. (**h**, **i**) Reproduced with permission from Ref. [59]. Copyright © 2019, American Chemical Society

Ag/Cu catalyst prepared by co-sputtering deposition to stabilize the intermediates. Experimentally, the synthesizing Ag/Cu catalysts achieve an EtOH FE of 41%, which was higher than that of Cu (29%) in Fig. 5e. DFT calculations revealed that multiple bind sites on Ag/Cu surface made the C_2H_4 reaction pathway unstable, but promoted the formation of EtOH intermediates, thus improving the selectivity of EtOH. Zheng et al. [241] also revealed that electron transfer at the interface of Cu and Ag was favorable for the intermediates CH_3CHO^* and $CH_3CH_2O^*$ during CO_2RR based on DFT calculations, which resulted in 126-fold enhancement in the alcohol/C_2H_4 ratio. In addition, Zhang and coworkers found that the intermediate of $*CO_2^-$ bonded to the surface of Ag-decorated Cu strongly through C and weakly through O by using in situ Raman spectroscopy. This unique adsorption was conducive to the formation of C_2H_4. Furthermore, Wang et al. developed Ag-doped Cu to promote C_1–C_2 coupling, which was more conducive to improving the selectivity of PrOH during CORR. Experimentally, Ag-doped Cu catalyst achieved a PrOH FE of 33% at 4.5 mA cm^{-2} with a total C_{2+} FE of about 80%. DFT calculations showed that an asymmetric active site was provided due to strain and ligand effects, which contained two adjacent Cu atoms with distinct electronic structures to support both C_1–C_1 and C_1–C_2 coupling. Different from Ag–Cu alloy catalysts, Ag/Cu composites were investigated and showed excellent catalytic activity during CO_2RR. Du and coworkers constructed homogeneous Ag–Cu alloy and Ag/Cu composites by uniformly distributing tiny Ag NPs on the surface of large Cu NPs in Fig. 5f [242]. Compared with Ag–Cu alloy, Ag/Cu

catalyst was favorable to the formation of C_2 products due to the presence of Cu–Ag interface, especially C_2H_4 (Fig. 5g).

3.5.2 Cu–Zn Alloys

Cu–Zn bimetallic catalysts have been considered to be an effective way to improve the catalytic performance of CO_2RR, and attracted much attention due to their low cost and non-toxicity. Because of the high selectivity of Zn nanomaterials for CO_2RR to CO, it was expected that a bimetallic Cu–Zn bimetallic nanomaterial would generate hydrocarbons via the method of "relay catalysis". Several previous works reported that the main product of CuZn alloy catalysts was CO or HCOOH as the main product, which could probably be due to the reduced adsorption energy of both surface $*CO_2$ and *CO species due to the lower Cu contents in Zn-rich alloys [243, 244]. Recent studies have demonstrated enhanced C_{2+} products FE on Cu–Zn catalysts for CO_2RR. For instance, Ren et al. [59] reported that the selectivity of EtOH and C_2H_4 can be changed by tuning the content of Zn in the Cu_xZn film catalyst, in which the highest FE of CO_2 reduction to alcohols was 29.1% in Fig. 5h. The authors demonstrated that the amount of CO on Cu site could be increased due to the spillover of CO from Zn to Cu site, which was further reduced to *CHO or *CH (Fig. 5i). Furthermore, the weak adsorption energy of *CO on the Zn sites also can further reduce to EtOH by inserting the bond between Cu sites and $*CH_2$ to form $*COCH_2$. In addition, B–Cu–Zn catalysts were favorable toward the formation of high selectivity for EtOH versus C_2H_4, tunning from 0.57 to 1.04 with the increase in Zn content [245]. CuZn bimetallic catalysts prepared by in situ electrochemical reduction bimetal-oxide, achieved 41% FE for C_{2+} liquids at only − 0.68 V_{RHE} [246]. Operando Raman spectroscopy showed that the stretching modes of CO binding on Cu were changed by Zn compared to pristine Cu and the adsorbed $*CH_2$ or $*CH_3$ were believed to form $*COCH_3$ intermediate and further reduce to EtOH. It is worth noting that CuZn bimetallic was completely reduced [246], while B–Cu–Zn catalysts were partially reduced [245]. This difference may depend on the reduction time, zinc oxide thickness, and synthesis method.

Different from the higher FE of EtOH for Cu–Zn bimetallic catalysts, hydrocarbons containing no alcohols can also be formed. For instance, Du and coworkers proposed an engineering strategy to stabilize the Cu^+ species by constructing Cu/ZnO_x interfaces [247]. In situ Raman spectroscopy measurement demonstrated that OD-Cu is easier to be reduced than Cu/ZnO_x in a CO_2-saturated 0.1 M $KHCO_3$. They proposed that the higher FE of CH_4 and C_2H_4 on Cu/ZnO_x catalysts is attributed to the presence of the surface Cu^+ species. By tuning the concentration of Zn [248], size-controlled (~ 5 nm) $Cu_{100-x}Zn_x$ NPs showed a drastic increase in CH_4 selectivity (~ 70% FE) with trace amount of C_2H_4 for Zn contents from 10 to 50, while the H_2 production was suppressed. Hou reported that Zn@Cu NPs exhibited the highest C_2H_4 FE of 43.1% without alcohols [249]. In addition, The C_2H_4 FE was as high as 91.1% on Cu oxides/ZnO electrocatalysts. Furthermore, Du and coworkers also prepared Cu–Zn Alloy and Cu–Zn mixture catalysts [243]. Compared with Cu–Zn mixture, Cu–Zn material showed significant selectivity to C_2H_4 accompanied with the simultaneous decrease in CO, indicating that both stabilization of *CO and its transfer from Zn to neighboring Cu promoted the formation of C_2H_4.

3.5.3 Cu–Au/Pd/Ni/Al Alloys

Compared with Cu–Ag and Zn systems, the Cu–Au system has obvious similarities. As the Au content changes, the different components of the Cu–Au system show enhanced selective generation of CO [250, 251], C_2H_4 [252], and even alcohols [253–255]. For example, Luo reported AuCu alloy NPs embedded Cu submicrocone arrays [253]. Enhanced EtOH selectivity with an FE of ~ 31% was gained in $KHCO_3$ aqueous solution, while C_2H_4 formation was relatively inhibited. DFT calculation results indicated that the introduction of Au enhanced the binding energy of $*OCHCH_3$ intermediate to improve the selectivity of EtOH. In addition, Zhang and coworkers successfully synthesized heterophane 4H/fcc Au@Cu nanostructures, which achieved the $FE_{C_2H_4}$ of 46.7% at − 1.17 V_{RHE}. In addition, Cu–M (where M = Ni, Pt, Pd) generally leads to an increase in HER activity compared to pure Cu, but hydrocarbons and alcohols are also produced in some cases. For instance, Han and coworkers reported that Cu–Pd bimetallic catalysts with the C_2H_4 FE of 45.2% at − 1.2 V_{RHE} [256]. CO and CH_4 were also detected on Cu–Pd and Cu–Pt bimetallic catalysts [257–259]. For Cu–Ni bimetallic catalyst, Zhang et al. synthesized Ni–Cu NW by uniformly decorating atomic nickel clusters on the surface of defect-rich Cu, which reached the highest C_{2+} products FE of 62% for at − 0.88 V_{RHE} [260]. DFT calculations found that the binding sites changed from the Ni–Ni bridge of $*CO_2$ and *COOH to the Ni–Cu bridge of *CO, which favored the C–C coupling step. Importantly, it should be noted that Sargent and coworkers used machine learning (ML) and DFT calculations to construct a mutually feedback screening framework to study the CO_2RR performance of Cu-based alloy catalysts under different atomic configurations. The surface adsorption energy of key intermediate *CO on the surface of over 16 000 different metals or alloys with different atomic arrangements was studied. They found that the low Miller exponent surfaces of Cu–Al alloy containing 4%–20% Al had the optimal adsorption energy for *CO and *H, which significantly reduced the energy barrier of *COOH, C–C coupling and C–H, effectively promoting the formation of C_2H_4. Using the method of physical vapor

deposition, they prepared a series of large-area nano-porous Cu–Al catalysts on the gas diffusion electrodes by controlling the surface composition, achieving an 80% FE of C_2H_4 with an ultra-high current density of 600 mA cm^{-2}. This work provided deep understanding of the core physicochemical mechanisms of CO_2RR, improving the performance of electrocatalytic reduction of CO_2 to key multi-carbon products, and promoting the practical application of CO_2RR technology.

4 Advanced Tools for Investigating the Mechanism of CO_2RR

At present, research on the mechanism of CO_2RR in the literature is mostly based on spectroscopy characterization techniques, isotope labeling, and DFT calculations. The characterization of electrocatalysts during CO_2RR is particularly important because of the dramatic transformation. As described in the above sections, Cu oxide is reduced to form a metallic Cu interface during CO_2RR, resulting in the generation of more active sites. In order to investigate the active phase of the catalyst and the relationship between structure and performance during CO_2RR, in situ or operational spectroscopy characterization techniques under controlled conditions were used. In addition, isotope labeling and DFT calculations are used to determine active sites of the catalyst and pathways of the product. These techniques can contribute to a deeper understanding of the mechanism of CO_2RR by (1) identifying catalytic active sites, (2) detecting key intermediate configurations, and (3) exploring reaction pathways.

4.1 Raman Spectrum

Different from other vibrational spectroscopy techniques, Raman spectroscopy is not only widely used to characterize the adsorbed species due to no obvious interference signal at the interface of electrodes and electrolytes, but also used to detect the evolution of catalysts because of its high spatial resolution (< 1 μm) [29, 261]. However, Raman spectroscopy, based on molecular bond vibrations, is not suitable for the detection of pure metal catalytic systems. In addition, due to the low detection sensitivity of Raman spectroscopy, Electrochemical SERS (EC-SERS) was developed with high detection sensitivity by increasing the Raman cross section to obtain appropriate data, which was used to investigate the intermediate adsorption and the change of catalyst chemical states in electrocatalysis processes [29, 262].

Thanks to its high sensitivity and rapid response ability, in situ EC-SERS is more suitable for detecting reaction intermediates during CO_2RR. Based on the Raman spectroscopy of *CO on Cu surfaces during CO_2RR, *CO is known to be a key intermediate for CO_2 reduction into C_{2+} products. The related signals of *CO at 280–288 and 360–370 cm^{-1} could be assigned to the restricted rotation of adsorbed CO and Cu–CO stretching (Fig. 6a), respectively [59, 80, 234, 246, 263–265]. The wave numbers of CO stretching modes were complex and widely distributed, which mainly included CO_L and CO_B [39]. Remarkably, Xu's group systematically studied the correlation between the Raman band of *CO and pH (Fig. 6b–d). The CO_L would be converted into CO_B as the pH of the electrolyte increased [39]. The presence of microenvironment on two samples also caused the subtle differences of CO adsorption bands. This observation presented by Xu and coworkers was further corroborated by papers found as far as possible [16, 25, 234, 237, 238, 246, 265–267], while CO_L detected in 1 M KOH has also been reported at − 0.6 V [80, 185, 268, 269]. It is worth noting that the CO_L was detected in 2 M KOH at − 0.61 V due to the retention of Cu–O species in the catalyst and the peak strength of CO_L decreased with the decrease in Cu–O residues during CO_2RR [268].

In addition to *CO, CO_3^{2-}, *COOH, and *C–H_x were observed on various catalysts to demonstrate preferred reaction pathways by using in situ EC-SERS. For example, two peaks at 1 010–1 032 and 1 065–1 080 cm^{-1} corresponded to the C–OH stretching of HCO_3^- and the total symmetric C–O stretch of carbonate, respectively [240, 282, 283]. The bands observed at 1 640 cm^{-1} belonged to the COOH* band and shifted to lower wavenumbers of 1 510 cm^{-1} through ^{13}C isotopic substitution due to the isotopic effect. The adsorbed HCO_3^- species firstly saturated and could be further reduced to COOH*. These results suggest that COOH* played a key role during CO_2RR [284]. Based on operando EC-SERS and the systematic analysis of electrocatalytic behavior, Ren et al. reported that free CO and *CH_3 were believed to be capable of forming *$COCH_3$, further exclusively reducing to EtOH [246]. In addition, CH-containing intermediates in the region from 2 700 to 3 000 cm^{-1} (Fig. 6b) also were identified as the key intermediate of C_2H_4 and C_2H_6 [73, 234, 269, 271]. Importantly, it was a huge challenge to assign these mountains more precisely due to a variety of species and adsorption modes of reaction products containing complexity C–H bonds [265].

Recently, in situ EC-SERS has been widely used to detect the evolution of oxygen-containing species [i.e., CuO, Cu_2O, $CuO_x/(OH)_y$] on Cu-based catalysts during CO_2RR. Multiple Raman peaks around 218, 427, 528, and 616 cm^{-1} were attributable to Cu_2O [59, 202, 279, 280]. In clear contrast, CuO was known to have a high strength peak at 288 cm^{-1} and a low strength peak at 337 cm^{-1}, which was not detected. In addition, the Raman bands of $Cu(OH)_2$ located at about 292 and 483 cm^{-1} were also not detectable [265, 280]. Importantly, $CuO_x/(OH)_y$ on Cu-based catalysts could be detected during CO_2RR [25, 39, 42, 237].

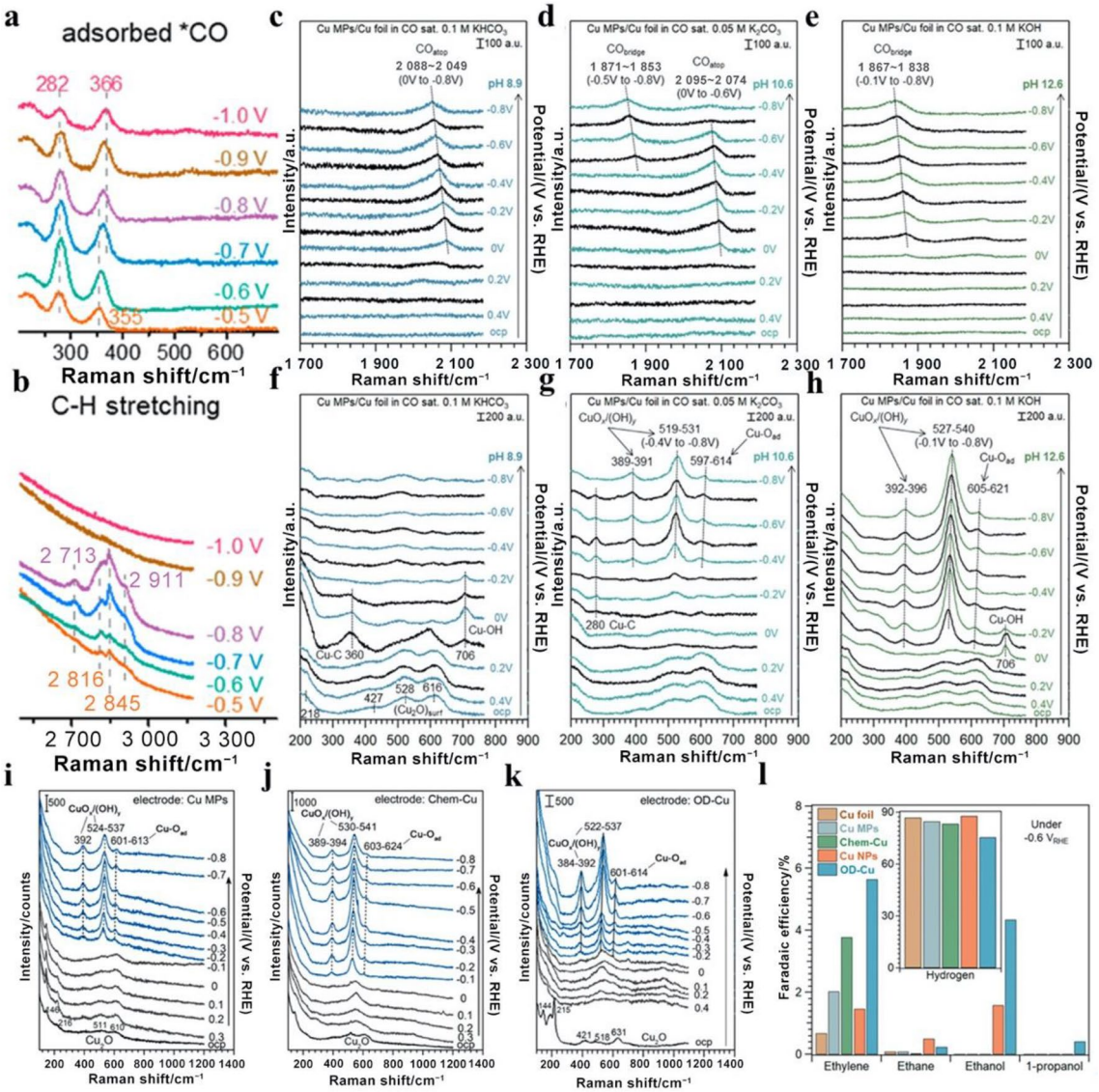

Fig. 6 Operando Raman spectra of **a** *CO and **b** *C–H during CO_2RR. (**a**, **b**) Reproduced with permission from Ref. [234]. Copyright © 2019, American Chemical Society. In situ SER spectra on polycrystalline Cu MPs in **c**, **f** 0.1 M $KHCO_3$, **d**, **g** 0.05 M K_2CO_3, **e**, **h** 0.1 M KOH. (**c**–**h**) Reproduced with permission from Ref. [39]. Copyright © 2020, American Chemical Society. Raman spectra of **i** Cu MPs, **j** Chem-Cu, and **k** OD-Cu in KOH electrolyte. **l** Comparison of product FE on four types of Cu. (**i**–**l**) Reproduced with permission from Ref. [25]. Copyright © 2020, American Chemical Society

Remarkably, Xu's group systematically studied the pH dependence of Cu surface speciation for the first time by in situ EC-SERS (Fig. 6f–i) [39]. Interestingly, the SERS band of Cu–O species is absent between − 0.4 and − 0.8 V_{RHE} in CO-saturated 0.1 M $KHCO_3$ (pH = 8.9), and their onset potential becomes more positive with the increase in pH values of electrolytes. Furthermore, the SERS band of the Cu_2O peak disappeared in CO_2-saturated 0.1 M $KHCO_3$ for all samples at − 0.4 V_{RHE} [238], which was consistent with the quasi-in situ XPS analysis. In addition, the peak strength of vibrational patterns located at 518 and 624 cm^{-1} from $Cu_x(OH)_y$ and Cu_2O specie on the catalyst surface has dropped to zero at potential < + 0.2 V_{RHE} in CO_2-saturated 0.5 M $KHCO_3$ (pH = 7.2) [237], which was even more corrected than the potential measured by the Operando X-ray diffraction (XRD) due to possible technical differences. The above studies showed that Cu–O species at low pH were completely reduced, which was consistent with recent reports in Table 2. However, the peaks of the Raman fingerprints of Cu–O species still existed and were not completely reduced in CO_2-saturated 0.5 M $KHCO_3$ [233, 245].

Importantly, recent studies have clarified that the presence of Cu–O species on the surface of Cu-based catalysts may not play a key role in the formation of C_{2+} products

Table 2 Summary of recently reported CORR/CO_2RR catalysts characterized by in situ/operando Raman spectroscopy

Catalysts	Electrolytes	Degree of reduction	Reduction potential/V_{RHE}	Reduction time	Reference
Cu MPs	CO 0.10 M $KHCO_3$	Full	−0.2	–	[39]
	CO 0.05 M K_2CO_3	Partial	–	–	
	CO 0.10 M KOH	Partial	–	–	
$Cu(OH)_2$	CO_2 0.10 M $KHCO_3$	Full	−0.5	Several minutes	[269]
Cu_2O NCs	CO_2 0.10 M $KHCO_3$	Full	−0.4	10 min	[238]
ID-Cu	CO_2 0.20 M $KHCO_3$	Full	−0.8	–	[73]
$Ag_{15}Cu_{85}$	0.50 M $KHCO_3$	Full	−0.1	–	[237]
ZnO/CuO	CO_2 0.10 M $KHCO_3$	Full	–	Immediately	[246]
Cu–Ag	CO_2 0.10 M $KHCO_3$	Full	−0.5	300 s	[234]
Cu	CO_2 0.10 M $KHCO_3$	Full	−0.4	–	[265]
Anodized Cu	CO_2 0.10 M $KHCO_3$	Full	−0.7	~1 s	[42]
Poly-Cu	CO_2 0.10 M $KHCO_3$	Full	−0.4	–	[263]
g-Cu	CO_2 0.10 M $KHCO_3$	Full	−0.65	1 min	[270]
CuO NPs	CO_2 0.50 M $KHCO_3$	Full	−0.1	–	[271]
CuOD	CO_2 0.10 M $KHCO_3$	Full	−0.4 V	Immediately	[272]
Cu/CoO	CO_2 1.00 M $KHCO_3$	Full	–	10 min	[273]
Cu_2O	CO_2 1.00 M KCl	Full	−0.6	220 s	[274]
Cu	CO_2 1.00 M KOH	Full	−0.1	–	[275]
Cu–Ag	CO_2 0.10 M $KHCO_3$	Full	−0.5	Immediately	[240]
Cu–In	CO_2 0.10 M $KHCO_3$	Full	−0.7	60 s	[266]
Cu	CO_2 1.00 M $KHCO_3$	Full	−0.39	–	[218]
Cu–Ce	CO_2 1.00 M $CsHCO_3$	Full	−0.35	–	[276]
Cu–Ag	CO_2 0.10 M $KHCO_3$	Full	−0.40	–	[277]
Cu–Sn	CO_2 0.10 M $KHCO_3$	Full	−0.75	–	[278]
Ag@CuO_x	CO_2 0.10 M $KHCO_3$	Partial	−0.55	–	[233]
CuS_x	CO_2 0.10 M $KHCO_3$	Full	−0.45	–	[279]
Cu_2O	CO_2 0.10 M $KHCO_3$	Full	–	10 s	[280]
Cu_2O films	CO_2 0.10 M $KHCO_3$	Full	−0.99	200 s	[202]
Cu–Zn	CO_2 0.10 M $KHCO_3$	Full	−0.85	300 s	[59]
Cu_2O	1.00 M $KHCO_3$	Full	–	10 min	[281]
B–Cu–Zn	CO_2 1.00 M $KHCO_3$	Partial	−1.43	–	[245]
Cu foil	CO 0.10 M KOH	Partial	−0.80	–	[25]
Cu GDE	CO_2 1.00 M KOH	Partial	–	–	[282]
Cu–P	CO_2 1.00 M KOH	Partial	–	–	[213]
Multi-hollow	CO_2 2.00 M KOH	Partial	–	–	[268]
Fragmental	CO_2 2.00 M KOH	Full	−0.60	20 min	[268]
Solid	CO_2 2.00 M KOH	Full	−0.60	20 min	[268]
Evaporated Cu	1.00 M KOH	Full	−0.67	60 s	[264]

during CO_2RR [25, 202, 280, 285]. For instance, Mandal et al. investigated the Cu oxidation state of Cu_2O catalysts with different morphologies (NWs, nanocrystals, and NPs) during CO_2RR by in situ Raman spectroscopy [280]. They found that CO_2RR products were observed only after the Cu_2O on the surface layer of catalysts was reduced to metallic Cu, which may be attributed to the fact that the reduction of Cu_2O was kinetically and energetically favorable than CO_2RR. Ren et al. and Dutta et al. have reported this similar phenomenon [202, 285]. Dutta et al. reported that the CO_2-related species during CO_2RR occurred preferentially on the metal Cu rather than the Cu–O species by using the operando Raman spectroscopy [285]. The disappearance XRD peaks of crystalline Cu_2O were observed by operando XRD, which happened before the transformation of Cu(I) to Cu(0) was completed by XAS detection. Through the in-depth analysis of XAS and XRD, it was further found that Cu_2O eventually formed metallic Cu due to lacking of long-range transitional order at most applied cathode potentials. Furthermore, Xu and coworkers also investigated the

speciation of commonly used Cu surfaces (including Cu foil, Cu MPs, Cu NPs, EP-Cu film, and OD-Cu) with the potentials of CO reduction reaction at CO-saturated 0.01 M KOH and 0.045 M K_2SO_4 (pH = 11.7) through in situ SERS (Fig. 6j–l) [25]. At negative potential, CuO_x and CuO_x/$(OH)_y$ species existed on all five catalysts, but the relative abundance of CuO_x on Cu foil was higher, whereas that of $Cu(OH)_y$ on Cu MPs or Cu NPs was higher. This suggested that the oxidized species were related to the initial degree of oxidation of Cu. The electrochemical CO reduction showed that the variation trend of product selectivity for five catalysts was different (Fig. 6m). Combining the variation trend of product selectivity and in situ SERS results on these catalysts, they concluded that Cu–O species were unlikely to be active in promoting C–C coupling pathways during CORR.

Apart from in situ EC-SERS, Cu–O species at low pH were completely reduced by using EELS and in situ TEM. For example, Lei et al. [41] prepared HQ-Cu (containing Cu, Cu_2O, CuO) and AN-Cu [containing Cu, $Cu(OH)_2$]. The distribution and evolution of Cu–O species were studied by electron microscopy and EELS and ultrathin specimens on an electrode were obtained through a focused ion beam. They found that Cu–O species on all electrodes have all been reduced to metallic Cu in CO_2-saturated 0.1 M $KHCO_3$ during the steady stage of the CO_2RR, regardless of the initial states, indicating that Cu–O species were not active sites for C_{2+} products. The pretreated electrode of HQ-Cu and AN-Cu, fully reducing to Metallic Cu by electroreduction at − 5.0 V vs. Ag/AgCl, showed even higher selectivity of C_{2+} products than the unpretreated. The grain boundaries and high exponent surfaces, resulting from the fragmentation process during the electrochemical oxidation–reduction cycle, promoted the C–C coupling. Furthermore, Peter and coworkers reported novel 2D CuO NS catalysts with high C_{2+} products and industrially relevant currents in gas diffusion electrodes at 0.1 M CO_2-saturated $KHCO_3$ solution [40]. The (001)-oriented CuO NS slowly evolved into highly branched Cu under applied bias by operando XAS and in situ TEM. The electrochemical transformation of CuO into disordered and undersaturated coordination metallic Cu took more than 2 h by operando XAS during CO_2RR, which were held responsible for high C_{2+} products.

4.2 IR Spectrum

Considering that the frequency of adsorbed functional groups is suitable to the range of IR spectroscopy, it has become an important tool to monitor adsorbed species on the surface of metal electrodes in the electrochemical process [286]. Four IR spectroscopy techniques can be accessible to investigate CO_2RR such as (1) transmission; (2) diffuse reflectance; (3) reflection–absorption, and (4) attenuated total reflection (ATR). The ATR-IR spectroscopy is commonly used for CO_2RR due to the minimization of electrolyte interference. The interactions between the attenuation waves and the adsorbed molecules enhance the absorption signal on the surface of thin metal electrodes, and this technique is often called SEIRAS.

Due to the higher IR absorption cross section of CO, ATR-SEIRAS is particularly sensitive to adsorbates containing C–O bonds. Waegele et al. reported that CO_B was an irreversible and inert surface adsorbed species under alkaline conditions during CO_2RR by using ATR-SEIRAS and DFT calculations [287]. Therefore, CO_B was rarely reported [227], while CO_L was generally reported and detected on the surface of higher C_{2+} products selectivity catalysts among the research papers [62, 227, 269, 288–290]. It was noted that only strong CO_B binding sites were detected on MP-Cu in 0.05 M $KHCO_3$ through in situ ATR-SEIRAS and were easily hydrogenated to produce CH_4 due to lower Cu–Cu coordination numbers [227], whereas the coexistence of CO_B and CO_L are apt to promote the formation of C_2H_4 (Fig. 7a, b). In addition, Xu's group investigate different sites available on surfaces of Cu-poly and OD-Cu using operando ATR-SEIRAS during CORR [291]. They identify that the CO_L located at 2 058 cm^{-1} on OD-Cu was different from that on Cu-poly (2 073 cm^{-1}) in Fig. 7c but resembled CO_L on Cu(100) observed by Hori et al. [292]. Combined reactivity studies and operando ATR-SEIRAS data, the distinct CO_L was most likely responsible for the OD-Cu's ability of facilitating C–C coupling, which was consistent with the conclusions of Hwang's group [289].

Beyond *CO, *CHO, *COOH, *HCO, *OCH_3 *OC_2H_5, *HCOO, *OCCOH, and *OCCOH were observed on various catalysts to demonstrate preferred reaction pathways through in situ ATR-SEIRAS [56, 62, 289, 290, 293]. For example, *COOH and bidentate COO^- species on Cu atoms were observed and possibly separated in the subsequent pathways to produce CO or HCOOH, respectively [293]. The CHO species from *CO hydrogenation at around ~ 1 754 cm^{-1} was the key intermediate for C–C coupling and replaced *O*CCO on the F–Cu(111) facets as the RDS based on DFT calculations [62]. In addition, Xiong et al. reported that *CHO served as not only the key intermediate for C–C coupling to form *OCCHO, but also the precursor of CH_4 at more negative bias based on in situ ATR-SEIRAS and DFT calculations [290]. Furthermore, in situ ATR-SEIRAS coupled with DFT calculations showed that two bands at 1 191 and 1 584 cm^{-1} are detected in Fig. 7d–f, corresponding to the C–O–H and C–O stretching of *OCCOH during CORR on Cu(100) electrodes at low overpotentials [56]. This observation directly confirmed for the first time the hypothesis that the C–C coupling to C_2 products on Cu(100) takes place through the CO–CO dimerization mechanism and the vibration characteristics of CO dimer cannot be observed on Cu(111). Together with ATR-SEIRAS, ambient-pressure

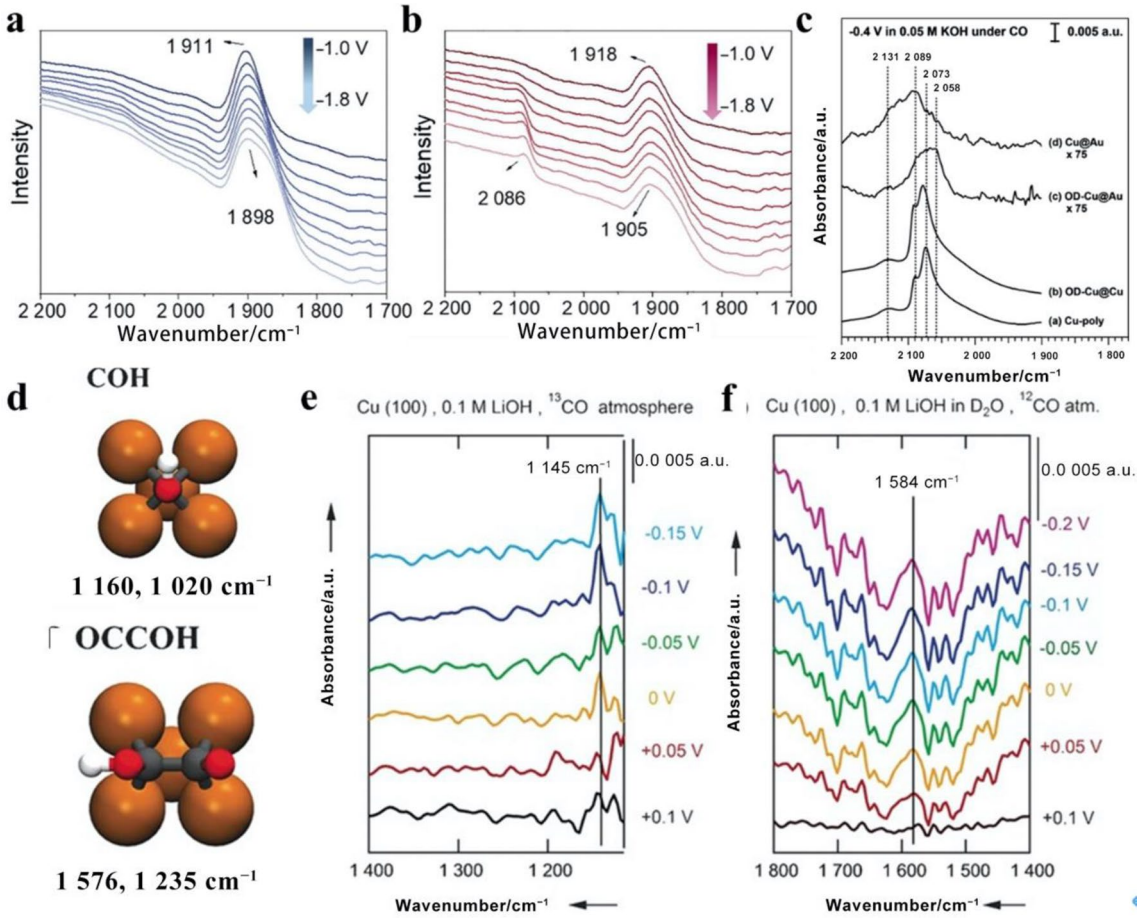

Fig. 7 In situ ATR-FTIR study of **a** MP-Cu and **b** EP-Cu. (**a**, **b**) Reproduced with permission from Ref. [227]. Copyright © 2021, Elsevier. **c** Operando ATR-SEIRAS spectra showing CO binding sites. Reproduced with permission from Ref. [291]. Copyright © 2019, American Chemical Society. **d** Schematic structures of adsorbed intermediates on Cu(100) and their calculated vibrational frequencies. Potential-dependent absorbance spectra for Cu(100) in the presence of **e** ^{13}CO and with **f** D_2O as electrolyte. (**d**–**f**) Reproduced with permission from Ref. [56]. Copyright © 2017, Wiley

XPS, and DFT calculation, Shao's group elucidated the mechanism of CO_2RR [294]. This work revealed that CH_4 and CH_3OH produced via $*OCH_3$ obtained from O-bound CO_3, while the formation of C_2 hydrocarbon products was suggested to result from the C–C coupling between *CO and *CHO. In addition, *OCCO was observed for the first time and identified as an intermediate of C_2 products pathway by using in situ ATR-SEIRAS [289]. Through the time-resolved IR analysis, CO dimerization occurred concurrently with CO adsorption (~ 5 s), while the conversion of *CO-to-*CHO has slower kinetics (~ 30 s), clearly indicating that C_1 path and C_2 path have different kinetics.

4.3 X-Ray Absorption Spectrum

The XAS spectra using synchrotron radiation sources is a powerful tool to probe the atom-specific geometry, valence states, and electronic structure of catalysts, thereby providing comprehensive understanding of the properties of the catalytic active sites and providing a valuable way for real-time reaction kinetics during CO_2RR [29, 295]. XAS spectra include X-ray absorption near-edge structures (XANES) and EXAFS. The former could quickly identify element species and the corresponding local structures. In addition, it is sensitive to the average oxidation state of elements, the unoccupied electron state, and charge transfer between occupied and unoccupied states. The latter provides local structural information including the bond distance and coordination number. Thus, operando XAS has been widely utilized to probe the active sites of electrodes and provide the real-time reaction dynamics under working conditions during CO_2RR.

The oxidation state of Cu in the process of CO_2RR was generally regarded as a key factor in determining the activity and selectivity of Cu-based catalysts, especially in promoting C–C coupling, which was well-characterized by

operating XAS under continuously varying cathode potential bias. However, there has been a long-lasting debate about the effect of (sub)surface oxygen due to the challenges in precisely and quantitatively distinguishing the Cu^+ species during CO_2RR. The presence of Cu^+ on Cu-based catalysts has been demonstrated by the evolution of the Cu K-edge. For instance, Yu and co-works' research showed that the content of Cu^+ species in multi-hollow Cu_2O was 32.1% after 20 min of reaction through linear-combination fitting of Cu K-edge spectra (Fig. 8a, b), which was consistent with the Raman measurements [268]. The retained Cu^+ species during CO_2RR were considered to be the key factor for the high C_{2+} selectivity, which was consistent with previous research (Fig. 8c) [184]. On the other hand, other reports have showed that the initial Cu^+ species could not affect the selectivity of C_{2+} products and were reduced to metallic Cu at the operating potential. Chang et al. observed that the reoxidation Cu may be the paramount key of products profile by employing in situ XAS and SERS [233]. Moreover, it was found that the amount of Cu^+ decreases with time due to the slow $Cu^+ \rightarrow Cu^0$ reduction process. It should be noted that the XAFS signal may be not sensitive to detect the trace amounts Cu^+ species on the surface of catalysts. For example, Mistry reported that the features of Cu and Cu_2O were still detected in the first 0.25 h [35], whereas only the characteristics of metallic Cu could be discernable after 1 h. Although the Cu^+ content of about 25%–28% on the surface of catalyst was detected by STEM–EDS, the XAFS signal was dominated by the signal for bulk metallic Cu.

Different from oxide-derived Cu-based catalysts, nonmetal elements (e.g., B, N, P, F, and S) substitution has been demonstrated to regulate the oxidation state of Cu-based catalysts [22, 53, 62, 309, 310]. During CO_2RR, in situ XANES was usually used to detect the average oxidation state of Cu. For instance, Zhou et al. prepared a series of B-doped Cu catalysts and used B as the dopant to tune the ratio of Cu^+ to

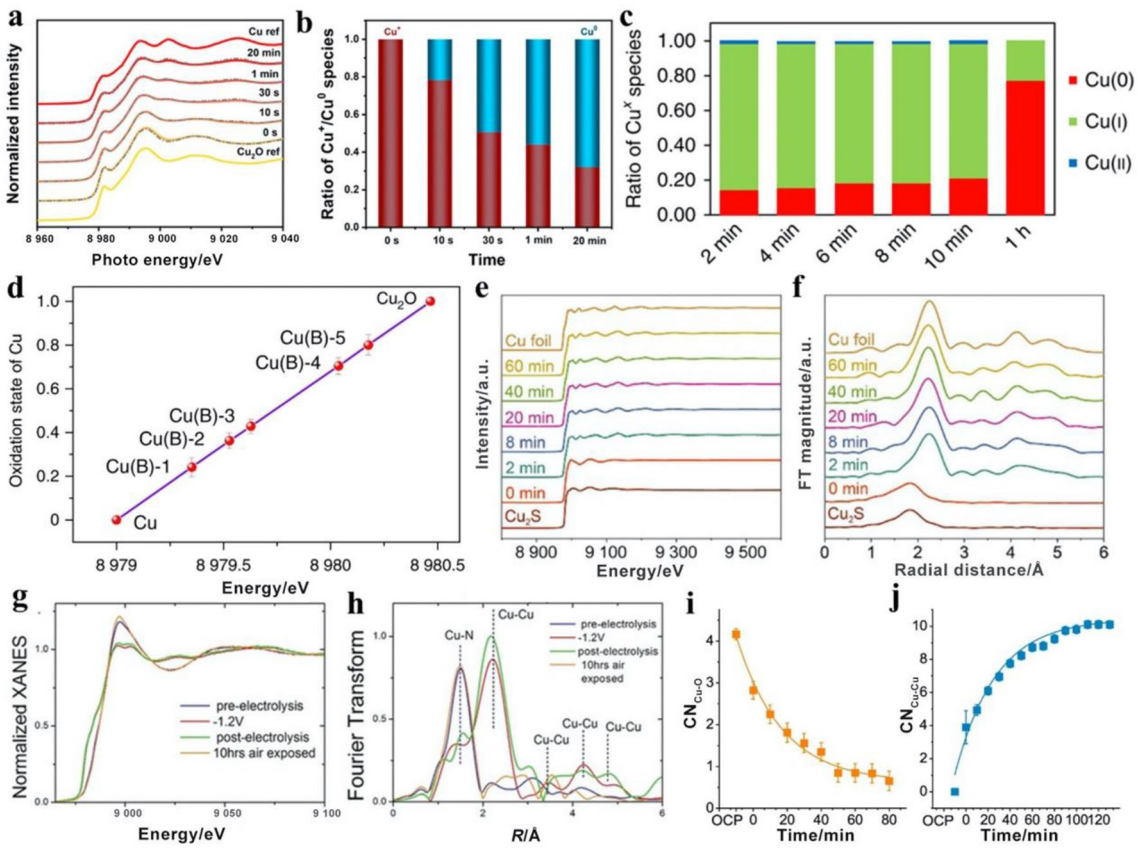

Fig. 8 **a** Cu K-edge XAS spectra of the multi-hollow Cu_2O catalyst at −0.61 V_{RHE}. **b** Change of the Cu^+/Cu^0 ratio with the reaction time at −0.61 V_{RHE}. (**a**, **b**) Reproduced with permission from Ref. [268]. Copyright © 2020, American Chemical Society. **c** Calculated the Cu^+/Cu^0 ratio with respect to time. Reproduced with permission from Ref. [184]. Copyright © 2020, Springer Nature. **d** Average oxidation state of Cu in Cu(B). Reproduced with permission from Ref. [53]. Copyright © 2018, Springer Nature. **e** Time-resolved in situ Cu K-edge XANES spectra of the $Cu_{2-x}S$ nanocrystals and **f** corresponding FT-EXAFS spectra. (**e**, **f**) Reproduced with permission from Ref. [312]. Copyright © 2021, Springer Nature. **g** The K-edge XANES of $Cu_{0.5}NC$. **h** Fourier transform of the EXAFS spectra of $Cu_{0.5}NC$. (**g**, **h**) Reproduced with permission from Ref. [145]. Copyright © 2021, Wiley. CNs of the first **i** Cu–O and **j** Cu–Cu. (**i**, **j**) Reproduced with permission from Ref. [40]. Copyright © 2021, Springer Nature

Cu^0, which achieved a maximum FE of ~ 80% for C_2 hydrocarbons. Due to the changes of surface geometry and the interaction between B and Cu, electrons transfer from Cu to B, resulting in the formation of Cu^+. In situ XANES results showed that the average oxidation states of Cu increased with the increase in B content during CO_2RR (Fig. 8d). DFT calculations indicated that the B dopant not only improved the reaction energy of the *CO + *H → *CHO step to inhibit the C_1 pathway, but also decreased the reaction energy of the C–C coupling step to enhance the C_2 pathway. Their theoretical and experimental results indicated that the Cu^+ sites played a key role in promoting the conversion of CO_2 to C_2 products. In addition, the average oxidation states of Cu in the F–Cu, Cu_2S–Cu–V, and Cu_3N catalysts were between 0 and + 1 during CO_2RR by using in situ XANES [22, 62, 309], which is beneficial to increase the FE of C_{2+} products. It was noteworthy that the Cu_2S and Cu_3N phases could be fully reduced into metallic Cu during CO_2RR [311, 312]. In particular, Xiong and coworkers reported polycrystalline Cu NPs prepared by the electrochemical desulfurization and surface reconstruction of $Cu_{2-x}S$ [312], which achieved the FE of 68.6% toward C_2H_4 production at − 1.2 V_{RHE}. In situ XAS and OH^- adsorption characterizations indicated that $Cu_{2-x}S$ was converted to the metal Cu with high-index facets during the continuous electroreduction reaction (Fig. 8e, f), which were the active sites for the C–C coupling.

In addition to detecting the average oxidation state of metal atoms, XAS can also be used to explore the coordination number of metal atoms. Molecular catalysts containing M–N_4 sites are also highly active and selective for CO_2RR as well, in which a reversible change between the atomically dispersed M–N_4 sites in M–N–C and NPs was confirmed with operando XAS during the CO_2RR [295, 306, 313]. The major products of molecular catalysts with a well-defined M–N_4 structure (MPcs: M = Mn, Fe, Co, and Ni) were CO [313], while that of CuPc were CH_4 [306]. Importantly, this phenomenon has also been reported on SACs [145], in which metallic Cu on Cu NPs are the active sites for CO_2 reduction to C_2 products. K. Dilan et al. reported that the isolated Cu sites in Cu–N–C material transiently and reversibly convert into metallic Cu NPs during electrolysis by operando XANES and EXAFS (Fig. 8g, h) [145]. Cu NPs were formed after prolonged electrolysis at − 1.2 V_{RHE}. A variety of products (CO, C_2H_4, EtOH, CH_4, etc.), especially higher FE of EtOH (55%), were detected due to the coexistence of the isolated Cu sites and Cu NPs. Moreover, Cu NPs have also been detected by ex situ XPS and are responsible for CO_2RR into C_2 products.

In addition, operando XAS has also been utilized to monitor the coordination number of a variety of Cu-based catalysts. The coordination number of Cu can affect catalytic activity of Cu-based catalysts, which can be subtle or significant, depending on the nature of the catalyst. It is worth noting that lowering the coordination number by introducing doping, defects, and grain boundary is also a strategy to enhance the adsorption of reaction intermediates and reduce the energy barrier of C–C coupling, allowing improving the selectivity of C_{2+} products during CO_2RR. In Table 3, the decrease in Cu–Cu coordination number showing enhanced CO_2RR performance has been observed. To prepare highly efficient CO_2RR electrocatalysts for the formation of C_{2+} products, several catalyst design strategies, such as O-D Cu, alloy, and halogen incorporation, have been demonstrated to lower the coordination number of Cu. For example, Peter and coworkers reported that CuO NS catalysts were completely chemically reduced to metallic Cu after 130 min at − 0.84 V_{RHE} during CO_2RR by using operando XAS [40]. Linear combination fittings revealed that the metallic Cu accounted for 99% and the remaining 1% was indeterminate. The CN value of Cu–Cu gradually increased during the reduction process and tended to be stable at 120 min (Fig. 8i–l). The obtained CN value of Cu (~10) was smaller than that of the bulk of Cu (12), indicating the presence of the undercoordinated Cu atoms.

In summary, operando XAS provides the information of average valence states, coordination numbers, and the evolution of catalysts under operating conditions, thus elucidating reaction active sites. However, the processes of CO_2RR occur at the electrode/electrolyte interface, and operando XAS measures the average structural information of samples. Therefore, operando XAS is very suitable for probing catalysts with a single active site. In addition, operando XAS was not sensitive for detecting Cu^+ species. To date, the oxidation state of Cu as the catalytic active center is controversial during CO_2RR, but the unsaturated state of Cu with higher C_{2+} selectivity has been fully confirmed. The OD-Cu and the nanostructured Cu catalysts show a lower CN through fitting the EXAFS curve, which may be the real reason for the increased catalytic activity of the OD-Cu.

4.4 Isotope Labeling

So far, Cu-based catalysts, as the most promising CO_2RR electrocatalysts, have great potential to directly convert CO_2 into valuable hydrocarbons and oxygenates at a reasonable current density to reduce carbon emissions. Although the products of carbon dioxide reduction are complex, up to 18 different possible products, it is commonly accepted that, except for HCOOH, other products are initiated by reducing CO_2 into *CO. Further protonation of *CO or *CO dimerization leads to a variety of products.

Since it is difficult to control the selectivity of a given product, in order to further improve the selectivity of catalysts, it is essential to first identify and understand the active sites and reaction pathways of products on Cu-based catalysts. It is noting that isotope labeling is an effective method to identify

Table 3 Summary of CN for recently reported CORR/CO_2RR catalysts fitted by EXAFS spectrum

Catalysts	Electrolytes	Potential/(V vs. RHE)	Major products (FE)	CN	Refs.
Plasma-Cu foil	0.1 M $KHCO_3$	−0.90	C_2H_4 (60.0%)	12.0 (set)	[35]
Ag@CuO_x-X	0.1 M $KHCO_3$	−1.20	EtOH (28.8%)	11.5	[233]
CuO NS	0.1 M $KHCO_3$	–	C_{2+} (65.0%)	10.1 ± 0.25	[40]
CuO MPNWs	0.5 M $KHCO_3$	−1.00	C_2H_4 (45.0%)	9.1	[296]
Cu@Cu_xO	0.1 M $KHCO_3$	−1.58	C_2H_4 (51.0%)	8.2	[297]
Cu_2O	0.1 M $CsHCO_3$	−1.20	C_2H_4 (50.6%)	8.1 ± 0.5	[298]
CuO microboxes	0.1 M K_2SO_4	−1.05	C_2H_4 (51.3%)	8.2	[299]
CuO_x-Vo	0.1 M $KHCO_3$	−1.40	C_2H_6 (63.0%)	6.1 ± 0.7	[300]
Plasma-Cu	0.1 M $KHCO_3$	−0.90	C_2–C_3 (45.0%)	11.3 ± 1.0	[301]
Cu	1.0 M KOH (CO)	−0.48	PrOH (23.0%)	10.8	[302]
HF-Cu	1.0 M KOH (CO)	−0.46	PrOH (20.0%)	11.4	[303]
$Cu_{100-x}Co_x$	0.1 M $KHCO_3$	−1.10	HCOOH (10.0%)	7.8 ± 0.6	[304]
Ag-doped Cu	1 M KOH (CO)	−0.56	C_{2+} (80.0%)	0.9 (2)	[239]
$Ce(OH)_x$/Cu	1 M KOH	−0.70	EtOH (43.0%)	11.2 (5)	[305]
CuPc	0.5 M $KHCO_3$	−1.05	CH_4 (66.0%)	6.5 (0.9)	[306]
CuPolyPc@CNT	0.1 M $CsHCO_3$	−0.70	CO (80.0%)	5.3 (6)	[307]
$Cu_{0.5}$NC	0.1 M $CsHCO_3$	−1.20	EtOH (55.0%)	3.2 (5)	[145]
MP-Cu	0.05 M $KHCO_3$	−1.70	C_2H_4 (93.0%)	6.8 ± 1.0	[227]
EP-Cu	0.05 M $KHCO_3$	−1.70	CH_4 (83.0%)	9.2 ± 1.4	[227]
Cu NSs	0.1 M $KHCO_3$	−1.18	C_2H_4 (83.2%)	9.7	[175]
Cu nanodendrites	0.1 M $KHCO_3$	−1.20	C_2H_4 (22.3%)	8.5	[183]
ID-Cu	0.1 M Na_2CO_3	–	C_2H_6 (72.0%)	1.1 (3)	[73]
F–Cu	1 M KOH	−0.80	C_2–C_4 (85.8%)	10.5 ± 1.2	[62]
CTF-Cu		−1.47	C_2H_4 (30.5%)	4.7	[308]
Cu_3Ag_1	0.5 M $KHCO_3$	−0.95	C_2H_5OH (63.0%)	7.0 (5)	[241]
Cu–CO_2	7 M KOH	−0.65	C_{2+} (90.0%)	10.9	[264]
Cu_I	0.1 M $KHCO_3$	−0.90	C_{2+} (80.0%)	8.5 (5)	[225]

active sites and determine reaction pathways, including ^{18}O, ^{13}C, and deuterium (D) isotope labeling. ^{18}O isotope labeling can not only confirm the residual O in OD-Cu during CO_2RR, but also determine the source of O in the products. For instances, Lum et al. synthesized ^{18}O enriched O-derived Cu by oxidation/reduction cycling in $H_2{}^{18}O$ [197]. Secondary-ion mass spectrometry showed that only a small fraction (< 1%) of ^{18}O content remains on the ^{18}O enriched O-D Cu in Fig. 9a, indicating the presence of rapid reoxidation during CO_2RR. Importantly, they determined for the first time that the O in EtOH originated from the solvent water rather than CO by reducing of $C^{16}O$ in $H_2{}^{18}O$ electrolytes (Fig. 9b) [20]. They proposed a new intermediate called Grotthuss chain ethynyl (C–CH) concerted hydrolysis to explain their experimental observations. The pathway involved C–CH, then rapidly reduced to EtOH as: CO → *COCO → *COCOH → *COHCOH → *CCOH → *CHCOH → *CCH → CHCHOH → ∗ CH_2CHOH → *CH_3CHOH → CH_3CHOH. However, Bell and coworkers clarified that the explanation of this observation did not require a novel mechanism of "C–CH" [148], which may be likely the result of isotopic competition between transiently produced AcH and solvent H_2O due to the formation of EtOH via the reduction of AcH during CORR or CO_2RR. This analysis was further confirmed by adding 0.2% of AcH to 98% $H_2{}^{18}O$ [99]. In addition, Jouny et al. reported the detected acetic acid with a signal of 62 amu (1 amu = $1.660\,5 \times 10^{-27}$ kg) when labeled $C^{18}O$ was used [99], in which one O came from the labeled $C^{18}O$ and one O originated from OH^- ions in the electrolyte (Fig. 9c), implying that the high acetate selectivity was attributable to the higher local pH at the triple-phase boundary. O exchange was not observed between acetic acid and $H_2{}^{18}O$, which indicated that *$COCH_2$ or *$COCH_3$ could be the intermediate of acetic acid. Further isotopic labeling studies clarified that *CO initially dimerized and further protonated to *CCOH and acetic acid was formed through direct OH attack of a ketene intermediate [314].

For ^{13}C isotopic labeling, the rapid equilibrium exchange between bicarbonate anions and CO_2 molecules was found by using in situ ATR-SEIRAS and isotopic labeling [315], which was further confirmed [46, 316]. In addition, by combining ATR-SEIRAS and isotopic labeling, Shao and coworkers found that the *CO was found to be consistent

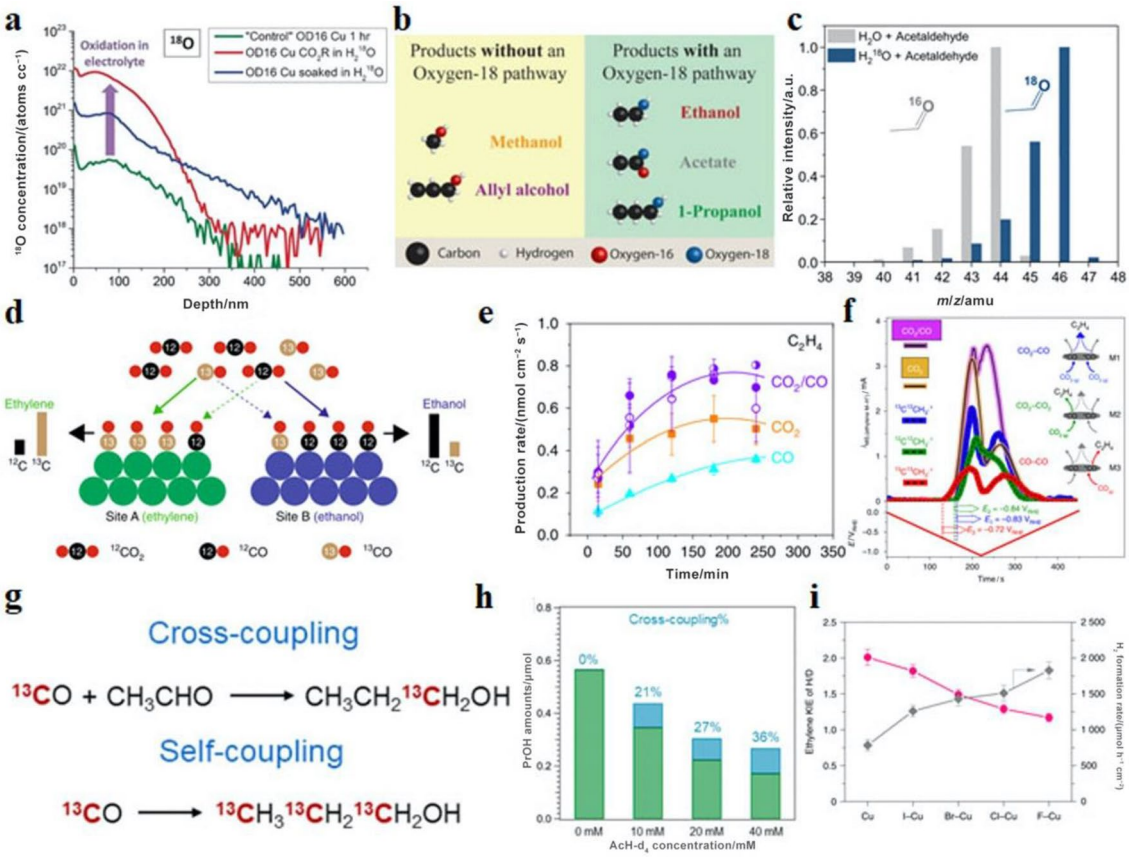

Fig. 9 **a** ^{18}O content in OD^{16} Cu 1 h, OD^{16} Cu with CO_2RR for 3 min in $H_2{}^{18}O$ electrolyte, and OD^{16} Cu that was soaked in $H_2{}^{18}O$ for 3 min. Reproduced with permission from Ref. [197]. Copyright © 2018, Wiley. **b** Chart showing products with an ^{18}O pathway and products without an ^{18}O pathway. Reproduced with permission from Ref. [20]. Copyright © 2018, American Chemical Society. **c** AcH in mixture of unlabeled H_2O and labeled $H_2{}^{18}O$. Reproduced with permission from Ref. [99]. Copyright © 2018, Springer Nature. **d** Hypothetical scenario in which the reduction of a mixture of ^{13}CO and $^{12}CO_2$ is carried out on a catalyst with two types of active sites. Reproduced with permission from Ref. [200]. Copyright © 2019, Springer Nature. **e** Time-dependent absolute product formation rates for C_2H_4. **f** Comparison of DEMS ion current sweeps over time for C_2H_4-related molecular fragment. (**e**, **f**) Reproduced with permission from Ref. [318]. Copyright © 2019, Springer Nature. **g** Reaction formulae for the cross-coupling between CO and AcH and the self-coupling during CORR. **h** Reaction formulas for cross-coupling and self-coupling. (**g**, **h**) Reproduced with permission from Ref. [81]. Copyright © 2020, American Chemical Society. **i** KIE of H/D in CO_2RR to C_2H_4 and HER performance. Reproduced with permission from Ref. [62]. Copyright © 2019, Springer Nature

with the bicarbonate anion rather than the CO_2 in the solution, indicating that the CO_2 reactant during CO_2RR came from the CO_2 molecule in equilibrium with the bicarbonate anion [81]. It was also worth noting that the carbon source of the CO_2RR product was indeed from the CO_2 molecule rather than the electrolyte or catalysts through the experiment of $^{13}CO_2$ isotope labeling [317]. More importantly, isotopic effects can be used to distinguish active sites based on the difference in the isotopic composition of the products [200, 318]. For example, by using isotopic labeling (Fig. 9d), OD-Cu catalysts have three types of active centers, which were used to selectively produce C_2H_4, EtOH/HAc, and PrOH, respectively [200]. In contrast, this phenomenon was not observed on the polycrystalline, (100), or (111) Cu catalysts. Strasser and coworkers found an unexpected increase of nearly 50% for C_2H_4 production under CO_2/CO co-feeds (Fig. 9e), which corresponded to a cross-coupled $^{12}CO_2$-^{13}CO reactive pathway through kinetic isotope belling experiments and operando DEMS capillary (Fig. 9f) [318]. They concluded that non-interfering, reactant-specific surface locations of CO_2 and CO were present. In addition, Xu and coworkers reported that the formation of PrOH came from self-coupling of CO and cross-coupling between CO and AcH by using isotope labeling [81], in which CO attacked the carbonyl group of AcH (Fig. 9g, h).

Similar to the isotopic effects of ^{13}C, the kinetic isotopic effect (KIE) was carried out by replacing the H_2O solvent with D_2O in the electrolyte during CO_2RR. Proton transfer occurring in RDS is usually affected by the KIE because the proton is too light. Therefore, KIE can be used to explore the

role of proton in RDS. During CO_2RR, as the value of KIE approaches 1, the impact on CO_2 reduction is negligible, while that is usually greater than 10 for HER [319]. This suggests that the KIE could be considerable when the RDS involved proton transfer, and vice versa. Wang and coworkers reported that the KIE value of H/D over the S_2-In catalyst was 1.9, which provided evidence that H_2O dissociation was involved in the RDS of CO_2RR to HCOOH [320]. Interestingly, by using DFT calculations, they found that the reaction from *CO-to-*CHO was the RDS for the CO_2RR to C_2H_4 [62]. To verify whether the RDS in CO_2RR to C_{2+} products involved proton transfer, they measured the KIE of catalysts. The KIEs over Cu, I–Cu, Br–Cu, Cl–Cu, and F–Cu catalysts, defined as the ratio of C_2H_4 formation rates in H_2O and D_2O, are 2, 1.8, 1.5, 1.3, and 1.2 (Fig. 9i), respectively. This results not only indicated that H_2O dissociation was involved in the RDS, but also implied that the presence of F accelerated the H_2O activation. In general, C_2H_4 has two different formation pathways, including the protonation of *CO and CO–CO coupling, which may be distinguished by direct experimental evidence provided through the KIE effect.

4.5 DFT Calculations

Due to the complex reaction networks, the corresponding reaction barrier, and cation effects, fully understanding the pathway of complex products and well establishing the structure-to-performance relation during CO_2RR are particularly challenging. In the past decades, DFT calculations with computational hydrogen electrode (CHE) model have been widely employed to study the reaction intermediates, verify experimental observations, and predict possible structure of catalysts [321, 322]. DFT calculations applied to the electrode/electrolyte interface are a huge challenge, but great progress has been made to describe reactions more accurately by improving models, including a few, one layer, and multiple layers of explicit water molecules [323–326]. A recent detailed review of the foundations, advanced computational models, H-shuttling approach, scaling relations, and suitable descriptor can be found elsewhere [96, 101, 327, 328]. In this part, we will focus on computational modeling of CO_2 and CO reduction to C_{2+} products, which generally includes three important processes: the protonation of *CO (e.g., *CHO and *COH), C–C coupling, and post-C–C-coupling steps.

The pathways for the formation of C_{2+} products are complex and controversial among DFT calculations, but it is generally accepted that *CO exists on Cu during CO_2RR or CORR. This intermediate can be further hydrogenated to *COH and *CHO by adding of H^+/e^- through the generation of an O–H or C–H bond, respectively. Based on DFT calculations with the CHE model, the *CHO species on Cu (211) was first proposed by Peterson and coworkers [57], but without considering reaction barriers and solvent. By building structure-sensitive maps of reaction intermediates, Calle-Vallejo and coworkers proposed that the stability of *COH and *CHO depended on the coordination number of Cu [329]. Cu tended to form * CHO more easily as the coordination number decreased. Therefore, it is fine to assume that CO reduction proceeds via *CHO on the surface of Cu. For Cu (100), Luo et al. concluded that the formation of *CHO was more favorable than that of *COH (TS barrier of 0.64 eV vs. 0.92 eV) [323], which was calculated by using the two-water solvation model. By building the model of full solvation, Cheng et al. also reported that *CHO formation was favored [330]. For Cu (111), Nie et al. found that the TS barrier of *CHO was higher than that of *COH with the two-water solvation model [331], which was consistent with the research of Xiao et al. [97]. In addition, by using explicit water with a full H coverage, Hussain et al. also reported that *COH formation was favored on Cu (111) [332]. Compared to Cu (111), *CHO becomes more stabilized relative to CO* on Cu_{55} [333]. Furthermore, the adsorption energy of intermediates increased with the decrease in the size of Cu NPs [334], but *CHO has always been stabler than *COH (Fig. 10a), which was consistent with others research [335]. In general, *CO mainly forms *CHO intermediate on the surface of Cu (100), Cu (211), and nanoclusters, while *COH intermediate on Cu (111) surface.

Apart from the effect of crystal facets, the formation of TS barrier of *COH and *CHO is affected by the proton source such as *H, $*H_2O$, and H_2O [90, 330, 336, 337]. For instance, Goodpaster et al. reported that the TS barrier of *CHO via reaction *CO with *H through a Tafel process was 0.75 eV, while that with water by a Heyrovsky reaction was 0.6 eV [90]. Furthermore, Cheng et al. calculated three alternative reactions to generate COH*, in which the protons came from *H, H_2O, or $*H_2O$. The corresponding TS barrier were 1.45, 0.70, and 0.74 eV, respectively. In addition, the effect of different explicit solvation models should be noted. For the Cu (111) surface [324], *COH was more stabilized (0.10 eV) than *CHO upon the addition of 1 H_2O with the presence of a H_2O bilayer, and relative stability of *COH further increased (relative to the no-water model) by 0.29 eV. *CHO was more favored over *COH on the Cu (100) surface by using explicit or implicit solvation models, which was consistent with recent research [338].

The formation of C–C bonds by coupling of two C_1 intermediates is a key step to produce C_{2+} products during CO_2RR. As shown in Scheme 2, C–C bonds can be formed from the coupling of various C_1 intermediates via a L–H mechanism. First of all, the *CO–*CO coupling is in competition with the protonation of *CO (e.g., *CHO and *COH) due to its high formation kinetic barrier. For example, by using the display solvent model, Cheng et al. reported that the energy barrier of C–C bonds formed by coupling of

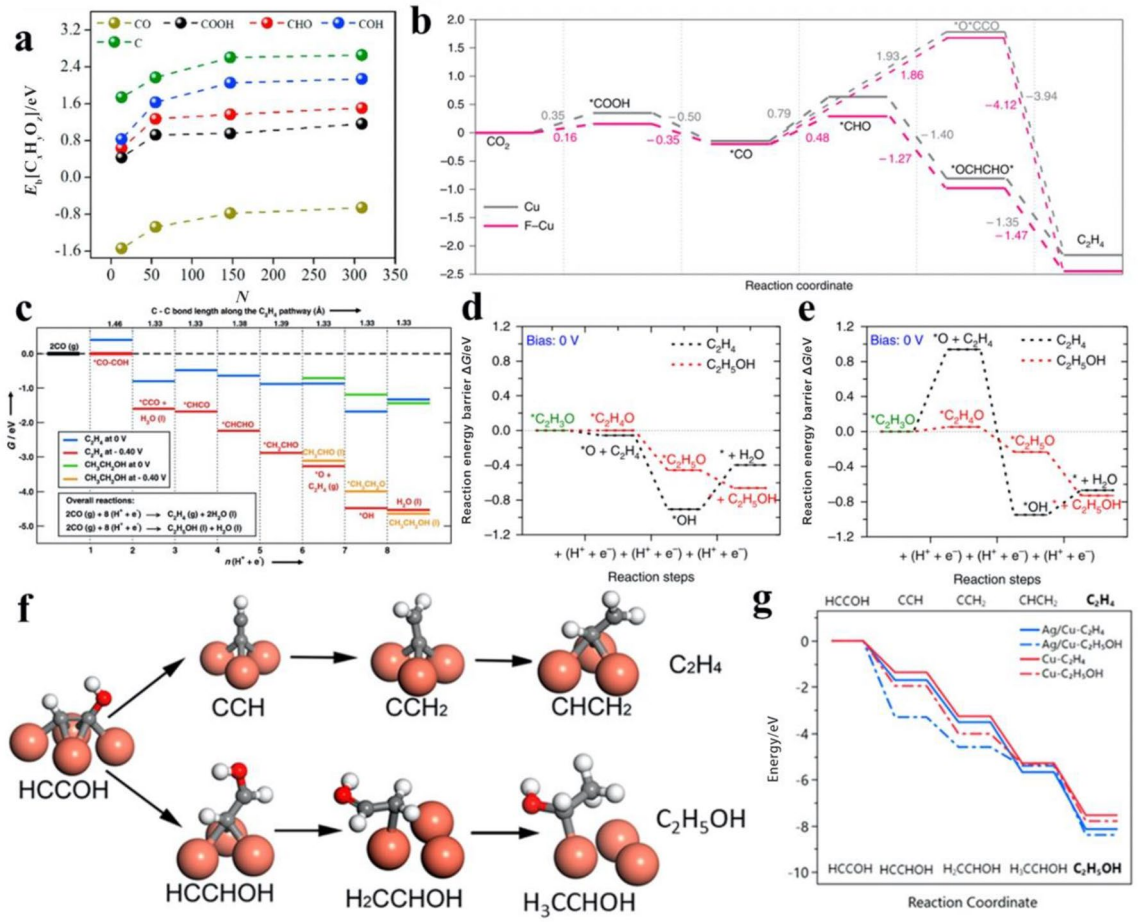

Fig. 10 **a** The binding energies of intermediates at various sizes of Cu NPs. Reproduced with permission from Ref. [334]. Copyright © 2019, Elsevier. **b** ^{18}O reaction energy diagram for CO_2RR to C_2H_4 on Cu(111) and F-Cu(111) facet. Reproduced with permission from Ref. [62]. Copyright © 2020, Springer Nature. **c** Lowest energy pathways for the electroreduction of CO to C_2H_4, MeCHO/EtOH. Reproduced with permission from Ref. [21]. Copyright © 2013, Wiley. Reaction energy diagram from the adsorbed C_2H_3O intermediate to C_2H_4 and EtOH for **d** pristine Cu and **e** Cu with Cu vacancy and subsurface S. (**d**, **e**) Reproduced with permission from Ref. [22]. Copyright © 2018, Springer Nature. **f** Reaction paths for C_2H_4 vs. EtOH on Cu(111). **g** Energy profiles of all intermediates toward C_2H_4 and EtOH on Cu and Ag/Cu catalysts. (**f**, **g**) Reproduced with permission from Ref. [23]. Copyright © 2019, American Chemical Society

two *CO is 0.69 eV on the Cu (100) surface [336], which is much lower than that of *CHO (0.96 eV). Furthermore, Martin and coworkers used a model that included the effects of electrochemical potentials, solvents, and electrolytes to investigate into the pathways by which C–C bonds [90]. Their results suggested that the formation of C–C bonds proceeded via formation of a CO dimer at low overpotentials on Cu (100) surfaces, whereas at high overpotentials, the C–C bond was formed by coupling of *CO and *CHO. However, the electrochemical reduction of *CO followed a thermodynamics-controlled *COH or *CHO pathway instead of *CO–*CO coupling on Cu (100), Cu (110), and Cu (111) surfaces when using an implicit solvation model or two-water model [62, 97, 323, 338].

By combining experiment with DFT calculations, the direct dimerization of *CO was proposed as the key step toward C_{2+} products at low overpotentials on the Cu electrode. The energy barrier of *CO–*CO coupling was fully explored by using theoretical calculations with different solvent models [19, 44, 45, 78, 264, 303, 338–340], in which that on Cu (100) surface was lowest in different Cu crystal planes [e.g., Cu (211), Cu (110) and Cu (111)]. The energy barrier of C–C bonds by coupling of various C_1 intermediates (e.g., *CO, *CHO, and *COH) was investigated in detail, which included OC–CO, OC–COH, OHC–CO, HOC–COH, and OHC–CHO. On the whole, the energy barrier of *CO–*CO coupling was higher than other C–C coupling on the surface of different Cu crystal planes [62, 90, 97, 323, 336, 340, 341]. In particular, Wang and coworkers reported that the formation of *OHCCH*O was thermodynamically favorable (Fig. 10b) [62]. In addition, Luo et al. reported that the energy barrier of *CO–*CO coupling was

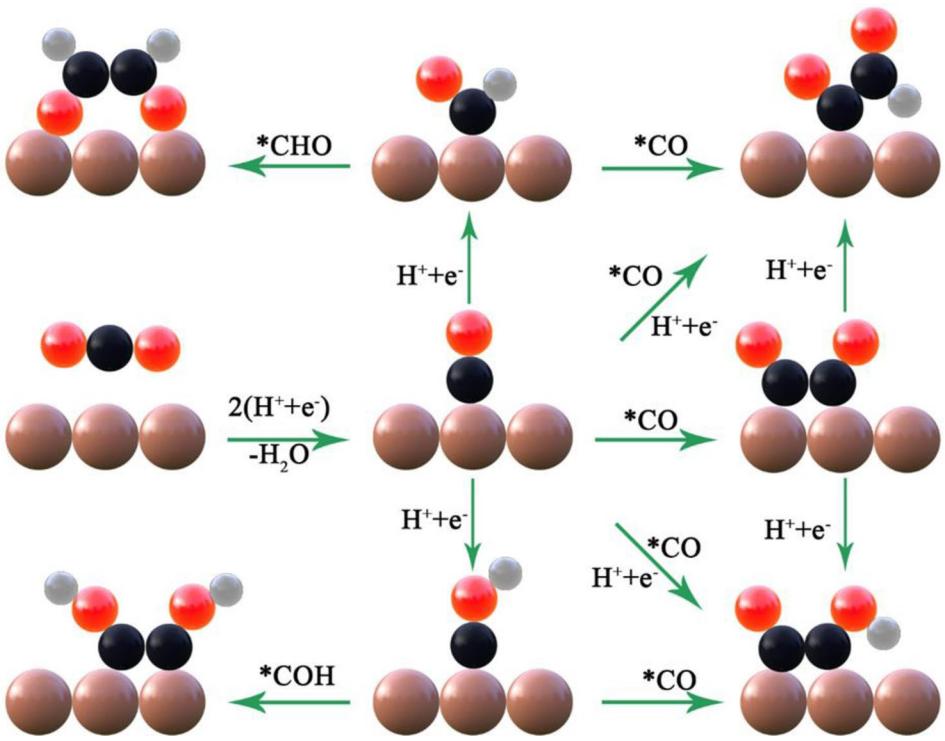

Scheme 2 Separation of C_1 and C_2 pathways from the *CO intermediate

1.22 eV on the Cu (100) surface, which was higher than that of CHO* (0.64 eV) and the dimerization of CHO* (0.22 eV) [323]. They proposed that the major route of C_2H_4/EtOH at low potential may be *CHO and subsequent the dimerization of *CHO, rather than the previously reported *CO–*CO coupling mechanism.

Due to the presence of the repulsion interaction among the *CO adsorbates, the increasing of *CO coverage not only reduces the binding energy of *CO, but also affects the energy barrier of *CO dimerization and hydrogenation. It is generally accepted that with the increase in *CO coverage, the binding energy of *CO and the energy barrier of *CO dimerization decrease significantly [62, 218, 339, 340, 342]. For the *CO hydrogenation, Ou et al. reported that the increase in *CO coverage may be easier to form *CHO on Cu (111), but vice versa on Cu (100) [44]. Furthermore, Huang and coworkers found that with the enrichment of *CO concentration on Cu surface, the energy barrier of *OC–CHO decreased from 0.44 to 0.30 eV, while that of *CO hydrogenation increased from 0.36 to 0.54 eV [158]. Their DFT calculations clarified that the formation of CH_4 was thermodynamically favorable at low CO coverage and *CHO becomes a common intermediate for the generation of CH_4 and C_2H_4 at high CO coverage, explaining the high FE of C_2H_4 and the inhibition of CH_4 at higher potentials. However, Xu et al. proposed that there was no quantitative relationship between CO partial pressure and surface CO coverage [343], and the hydrogenation of CO via an E–R mechanism is the RDS in the CORR rather than CO–CO coupling by using CO adsorption isotherms on Cu measured by in situ SERS.

Although understanding the initial C–C coupling steps has made much progress, only a few studies have addressed the basic steps of post-C–C coupling. However, some research groups and some researchers have begun to summarize the post-C–C coupling steps [26, 96]. On Cu-based catalysts, the distribution of C_{2+} products is complex and diverse. Since C_2H_4 and EtOH are the main C_{2+} products, recent DFT calculations have focused on providing an understanding of the key intermediates that control the C_2H_4 vs. EtOH selectivity. Therefore, we address recent progress on the theoretical understanding of their formation in the following sections. Based on the detailed analysis of the current research, we found that the relative stability of the bifurcated intermediate is the key to regulating the selectivity of C_2H_4 and EtOH.

It is generally accepted that the formation of C_2H_4 was thermodynamically favorable compared to EtOH on the regular Cu surface [21, 22, 80, 241, 323]. For instance, Koper and coworkers calculated the pathways for the CO reduction to C_2H_4, AcH, and EtOH [21]. DFT calculations clarified that the favorability of the *CH_2CHO hydrogenation step was inclined toward C_2H_4 formation by approximately 0.2 eV (Fig. 10c). Therefore, regulating the stability of shared intermediates may help to develop strategies tuning the proportion between C_2H_4 and EtOH. For example, Zhang et al. investigated the effects of energetics seen by the adsorbed bifurcated intermediates on the selectivity of C_2H_4

and EtOH by using DFT because they share a common intermediate state (*$OCHCH_2$) [22]. Their DFT results found that the intermediate of *$OCHCH_3$ was stabler than that of *O + C_2H_4 on a Cu_2S–Cu core–shell model with an atomic vacancy, whereas the opposite calculation results were presented on a pristine Cu slab (Fig. 10d, e). Therefore, the relative stability of *$OCHCH_3$ shifts the balance to enhance the selectivity of EtOH by suppressing C_2H_4 production, which was consistent with relevant reports [73, 241, 344]. Different from the scheme of *$OCHCH_3$, Luo et al. found that the breaking of C–O bond in ethylene oxide (CH_2–CH_2O*) required a higher barrier (1.01 eV) than the generation of ethylene hydroxide (CH_2–CH_2OH*) (0.85 eV) [323], from which C_2H_4 formation has a lower barrier in comparison with EtOH formation. Furthermore, Calle-Vallejo and coworkers provide a computational–experimental study of EOR to C_2H_4 and EtOH [345]. The adsorption energy of *OCH_2CH_2 was coordination number dependent, which became stabler as the coordination number decreases, thus promoting the production of EtOH.

In addition to the share intermediate of *$OCHCH_2$, the selectivity of between C_2H_4 and EtOH is determined by that of *CHCOH (denoted IM) rather close to C–C coupling [23, 218, 336, 346–348]. Specifically, the hydroxyl group of IM can be deoxidized to form *CCH (IM-C), leading to produce C_2H_4, while the hydrogenation of IM to *CHCHOH (IM-O) instead enhanced the formation of EtOH. For example, Cheng et al. reported that the reaction energy barrier of C_2H_4 including IM to IM-C via the E–R mechanism was 0.61 eV on Cu (100) [336], which was lower than that of EtOH including IM to IM-O (1.14 eV). They find that as the CO coverage increased, the barriers to both IM-C and IM-O pathways increased. At low CO coverage, the IM-C pathway was kinetically superior to the IM-O pathway, while the IM-O pathway was more favorable at 3/9 ML. In addition, they also reported that the relative stability of IM-C versus IM-O can be tuned by introducing diverse binding sites [23]. DFT calculations showed that multiple bind sites on the Ag/Cu surface had weaker bonding ability for IM-C relative to IM-O, indicating that the EtOH pathway became more favorable compared that on pure Cu (111) (Fig. 10f, g). It should be noted that the O in EtOH generated by the IM-O pathway must have come from CO.

5 Summary and Outlook

Although CO_2RR powered by renewable electricity is important in achieving carbon cycling and utilizing intermittent renewable energy sources, the technology is not yet commercially available due to the limitations of products selectivity, energy efficiency, and catalytic stability. In the past decade, the rapid development of advanced electrocatalysts has attracted a lot of attention and greatly improved the efficiency and selectivity of CO_2RR. However, C–C coupling of C_{2+} products through CO_2RR is far from ready for practical application, and the dominant factors that really dominate the reaction pathway are still controversial. In this progress report, we provide an overview of recent engineering strategies for enhancing the structure and composition of CO_2RR catalysts for C_{2+} products, and review advanced tools in understanding CO_2RR reactions, with a focus on the active sites and product generation pathways. These research issues and future research efforts to further understand the mechanism of CO_2RR are listed as below.

1. Further identification of true active sites. The performance of CO_2RR electrocatalysts and the understanding of the active sites have made great progress and been discussed in depth. Although the role of Cu^+ species in promoting CO_2RR selectivity toward a specific product has been highlighted in some studies, recent studies have shown that Cu oxide was completely reduced under neutral conditions and Cu–O species were unlikely to be the active sites facilitating the formation of C_{2+} products during CO_2RR. Furthermore, in situ/operando spectroscopic characterizations can be used not only to explore the active phase of the dynamic catalyst but also to distinguish the active sites during CO_2RR. Further understanding active phases and active sites of structural evolution of Cu-based electrocatalysts under operando reaction conditions is of great interest, which may help to establish the structure–activity relationship and accelerate the design of more advanced catalytic materials.
2. Further determining the possible pathways of C_{2+} products. Completely understanding and determining the possible pathways of C_{2+} products on Cu-based electrocatalysts during CO_2RR is critical for designing useful principles for the design of highly selective and active catalytic materials for C_{2+} products. Despite a great deal of research has been reported in the past decades, the reaction mechanism of CO_2RR, especially the formation pathway of C_{2+} products, has not been fully revealed due to the extremely complex reaction pathway network. It is one of the most challenging tasks to accurately determine pathway of C_{2+} products. Combining advanced spectroscopic characterizations and isotope labeling can provide direct evidence of the intermediate states of the products, which is expected to speed up the research journey. Future work should focus on correctly identifying the intermediate states and improving the temporal and spatial resolution of the operational/in situ techniques to capture key intermediate states not detected in previous experiments.
3. Understanding the mechanism of CO_2RR with the aid of DFT calculations. Currently, DFT calculations are

typically used to provide atomic-scale insights based on the calculated energy barrier of different product pathways over a variety of Cu-based catalysts. However, in most studies, computational models are ideal and simplified atomic configurations based on the initial structure of the catalyst, neglecting the dynamic changes of the catalyst structure during the reaction process, which may result in inappropriate reaction centers and is not conducive to providing correct theoretical guidance. In addition, DFT calculations can only provide the possible reaction pathway due to the complex pathways and intermediate states. Therefore, a computational framework should consider both structural changes and intermediate states. In situ/operando spectroscopy and isotope labeling can not only provide the evolution of catalyst structure, but also determine the adsorption of the key intermediate states. DFT Calculations are able to accurately interpret the spectral data of the catalyst, which makes it possible to establish a link between experimental spectral characteristics and theoretical models. Importantly, ML can use an ever-growing data set to understand the adsorption energies of different reaction intermediates to train the model to predict higher selective CO_2RR catalysts. Hence, DFT calculations based on the advanced experimental tools and intelligent ML should be an important research direction of CO_2RR in the future, which can provide a correct understanding of the catalytic mechanism to accelerate the design of high activity and high selectivity C_{2+} product catalysts.

Acknowledgements This work is supported by the National Natural Science Foundation (NNSF) of China (U21A20312, 21975162, and 21574084), Shenzhen Science and Technology Program (JCYJ20200109105803806, RCYX20200714114535052, and JCYJ20190808142219049) and Science & Technology Research Program of Chongqing University of Arts and Sciences (R2021SDQ06).

Declarations

Conflict of interest There are no conflicts to declare.

Ethics Approval and Consent to Participate Not applicable.

References

1. Liu, H.L., Zhu, Y.T., Ma, J.M., et al.: Recent advances in atomic-level engineering of nanostructured catalysts for electrochemical CO_2 reduction. Adv. Funct. Mater. **30**, 1910534 (2020). https://doi.org/10.1002/adfm.202070107
2. Fan, L., Xia, C., Yang, F.Q., et al.: Strategies in catalysts and electrolyzer design for electrochemical CO_2 reduction toward C_{2+} products. Sci. Adv. **6**, eaay3111 (2020). https://doi.org/10.1126/sciadv.aay3111
3. Daiyan, R., Lu, X.Y., Ng, Y.H., et al.: Liquid hydrocarbon production from CO_2: recent development in metal-based electrocatalysis. ChemSusChem **10**, 4342–4358 (2017). https://doi.org/10.1002/cssc.201701631
4. Xie, H., Wang, T.Y., Liang, J.S., et al.: Cu-based nanocatalysts for electrochemical reduction of CO_2. Nano Today **21**, 41–54 (2018). https://doi.org/10.1016/j.nantod.2018.05.001
5. Zhu, S.Q., Delmo, E.P., Li, T.H., et al.: Recent advances in catalyst structure and composition engineering strategies for regulating CO_2 electrochemical reduction. Adv. Mater. **33**, 2005484 (2021). https://doi.org/10.1002/adma.202005484
6. Zheng, Y., Chen, Z.W., Zhang, J.J.: Solid oxide electrolysis of H_2O and CO_2 to produce hydrogen and low-carbon fuels. Electrochem. Energy Rev. **4**, 508–517 (2021). https://doi.org/10.1007/s41918-021-00097-4
7. Li, W.P., Luo, J.L.: Correction to: High-temperature electrochemical devices based on dense ceramic membranes for CO_2 conversion and utilization. Electrochem. Energy Rev. (2021). https://doi.org/10.1007/s41918-021-00123-5
8. Zhu, Y.T., Cui, X.Y., Liu, H.L., et al.: Tandem catalysis in electrochemical CO_2 reduction reaction. Nano Res. **14**, 4471–4486 (2021). https://doi.org/10.1007/s12274-021-3448-2
9. Karapinar, D., Creissen, C.E., Rivera de la Cruz, J.G., et al.: Electrochemical CO_2 reduction to ethanol with copper-based catalysts. ACS Energy Lett. **6**, 694–706 (2021). https://doi.org/10.1021/acsenergylett.0c02610
10. Xiao, C.L., Zhang, J.: Architectural design for enhanced C_2 product selectivity in electrochemical CO_2 reduction using Cu-based catalysts: a review. ACS Nano **15**, 7975–8000 (2021). https://doi.org/10.1021/acsnano.0c10697
11. Wu, Z.Z., Gao, F.Y., Gao, M.R.: Regulating the oxidation state of nanomaterials for electrocatalytic CO_2 reduction. Energy Environ. Sci. **14**, 1121–1139 (2021). https://doi.org/10.1039/d0ee02747b
12. He, J.F., Li, Y.L., Huang, A.X., et al.: Electrolyzer and catalysts design from carbon dioxide to carbon monoxide electrochemical reduction. Electrochem. Energy Rev. **4**, 680–717 (2021). https://doi.org/10.1007/s41918-021-00100-y
13. Hori, Y., Murata, A., Takahashi, R.: Formation of hydrocarbons in the electrochemical reduction of carbon dioxide at a copper electrode in aqueous solution. J. Chem. Soc. Faraday Trans. 1 **85**, 2309–2326 (1989). https://doi.org/10.1039/f19898502309
14. Raciti, D., Wang, C.: Recent advances in CO_2 reduction electrocatalysis on copper. ACS Energy Lett. **3**, 1545–1556 (2018). https://doi.org/10.1021/acsenergylett.8b00553
15. Guzmán, H., Russo, N., Hernández, S.: CO_2 valorisation towards alcohols by Cu-based electrocatalysts: challenges and perspectives. Green Chem. **23**, 1896–1920 (2021). https://doi.org/10.1039/d0gc03334k
16. Wang, S., Kou, T., Baker, S.E., et al.: Recent progress in electrochemical reduction of CO_2 by oxide-derived copper catalysts. Mater. Today Nano **12**, 100096 (2020). https://doi.org/10.1016/j.mtnano.2020.100096
17. Birhanu, M.K., Tsai, M.C., Kahsay, A.W., et al.: Copper and copper-based bimetallic catalysts for carbon dioxide electroreduction. Adv. Mater. Interfaces **5**, 1800919 (2018). https://doi.org/10.1002/admi.201800919
18. Niu, Z.Z., Chi, L.P., Liu, R., et al.: Rigorous assessment of CO_2 electroreduction products in a flow cell. Energy Environ. Sci. **14**, 4169–4176 (2021). https://doi.org/10.1039/d1ee01664d
19. Garza, A.J., Bell, A.T., Head-Gordon, M.: Mechanism of CO_2 reduction at copper surfaces: pathways to C_2 products. ACS Catal. **8**, 1490–1499 (2018). https://doi.org/10.1021/acscatal.7b03477
20. Lum, Y., Cheng, T., Goddard, W.A., III., et al.: Electrochemical CO reduction builds solvent water into oxygenate products. J. Am. Chem. Soc. **140**, 9337–9340 (2018). https://doi.org/10.1021/jacs.8b03986

21. Calle-Vallejo, F., Koper, M.T.M.: Theoretical considerations on the electroreduction of CO to C_2 species on Cu(100) electrodes. Angew. Chem. Int. Ed. **52**, 7282–7285 (2013). https://doi.org/10.1002/anie.201301470
22. Zhuang, T.T., Liang, Z.Q., Seifitokaldani, A., et al.: Steering post-C–C coupling selectivity enables high efficiency electroreduction of carbon dioxide to multi-carbon alcohols. Nat. Catal. **1**, 421–428 (2018). https://doi.org/10.1038/s41929-018-0084-7
23. Li, Y.C., Wang, Z.Y., Yuan, T.G., et al.: Binding site diversity promotes CO_2 electroreduction to ethanol. J. Am. Chem. Soc. **141**, 8584–8591 (2019). https://doi.org/10.1021/jacs.9b02945
24. Wang, J.L., Tan, H.Y., Zhu, Y.P., et al.: Linking the dynamic chemical state of catalysts with the product profile of electrocatalytic CO_2 reduction. Angew. Chem. Int. Ed. **60**, 17254–17267 (2021). https://doi.org/10.1002/anie.202017181
25. Zhao, Y.R., Chang, X.X., Malkani, A.S., et al.: Speciation of Cu surfaces during the electrochemical CO reduction reaction. J. Am. Chem. Soc. (2020). https://doi.org/10.1021/jacs.0c02354
26. Wang, Y.H., Liu, J.L., Zheng, G.F.: Designing copper-based catalysts for efficient carbon dioxide electroreduction. Adv. Mater. **33**, 2005798 (2021). https://doi.org/10.1002/adma.202005798
27. Tomboc, G.M., Choi, S., Kwon, T., et al.: Potential link between Cu surface and selective CO_2 electroreduction: perspective on future electrocatalyst designs. Adv. Mater. **32**, 1908398 (2020). https://doi.org/10.1002/adma.201908398
28. Li, M.R., Garg, S., Chang, X.X., et al.: Toward excellence of transition metal-based catalysts for CO_2 electrochemical reduction: an overview of strategies and rationales. Small Methods **4**, 2000033 (2020). https://doi.org/10.1002/smtd.202000033
29. Daiyan, R., Saputera, W.H., Masood, H., et al.: A disquisition on the active sites of heterogeneous catalysts for electrochemical reduction of CO_2 to value-added chemicals and fuel. Adv. Energy Mater. **10**, 1902106 (2020). https://doi.org/10.1002/aenm.201902106
30. Feng, G.H., Chen, W., Wang, B.Y., et al.: Oxygenates from the electrochemical reduction of carbon dioxide. Chem. Asian J. **13**, 1992–2008 (2018). https://doi.org/10.1002/asia.201800637
31. Wang, L.M., Chen, W.L., Zhang, D.D., et al.: Surface strategies for catalytic CO_2 reduction: from two-dimensional materials to nanoclusters to single atoms. Chem. Soc. Rev. **48**, 5310–5349 (2019). https://doi.org/10.1039/c9cs00163h
32. Fan, Q., Zhang, M.L., Jia, M.W., et al.: Electrochemical CO_2 reduction to C_{2+} species: heterogeneous electrocatalysts, reaction pathways, and optimization strategies. Mater. Today Energy **10**, 280–301 (2018). https://doi.org/10.1016/j.mtener.2018.10.003
33. Pander, J.E.I., Ren, D., Huang, Y., et al.: Understanding the heterogeneous electrocatalytic reduction of carbon dioxide on oxide-derived catalysts. ChemElectroChem **5**, 219–237 (2018). https://doi.org/10.1002/celc.201701100
34. Zhao, J., Xue, S., Barber, J., et al.: An overview of Cu-based heterogeneous electrocatalysts for CO_2 reduction. J. Mater. Chem. A **8**, 4700–4734 (2020). https://doi.org/10.1039/c9ta11778d
35. Mistry, H., Varela, A.S., Bonifacio, C.S., et al.: Highly selective plasma-activated copper catalysts for carbon dioxide reduction to ethylene. Nat. Commun. **7**, 12123 (2016). https://doi.org/10.1038/ncomms12123
36. Xiao, H., Goddard, W.A., III., Cheng, T., et al.: Cu metal embedded in oxidized matrix catalyst to promote CO_2 activation and CO dimerization for electrochemical reduction of CO_2. Proc. Natl. Acad. Sci. USA **114**, 6685–6688 (2017). https://doi.org/10.1073/pnas.1702405114
37. Kim, J.Y., Kim, G., Won, H., et al.: Synergistic effect of Cu_2O mesh pattern on high-facet Cu surface for selective CO_2 electroreduction to ethanol. Adv. Mater. **34**, 2106028 (2022). https://doi.org/10.1002/adma.202106028
38. Capdevila-Cortada, M.: Probing the speciation. Nat. Catal. **3**, 419–419 (2020). https://doi.org/10.1038/s41929-020-0464-7
39. Chang, X.X., Zhao, Y.R., Xu, B.J.: pH dependence of Cu surface speciation in the electrochemical CO reduction reaction. ACS Catal. **10**, 13737–13747 (2020). https://doi.org/10.1021/acscatal.0c03108
40. Wang, X., Klingan, K., Klingenhof, M., et al.: Morphology and mechanism of highly selective Cu(II) oxide nanosheet catalysts for carbon dioxide electroreduction. Nat. Commun. **12**, 794 (2021). https://doi.org/10.1038/s41467-021-20961-7
41. Lei, Q., Zhu, H., Song, K.P., et al.: Investigating the origin of enhanced C_{2+} selectivity in oxide-/hydroxide-derived copper electrodes during CO_2 electroreduction. J. Am. Chem. Soc. **142**, 4213–4222 (2020). https://doi.org/10.1021/jacs.9b11790
42. An, H.Y., Wu, L.F., Mandemaker, L.D.B., et al.: Sub-second time-resolved surface-enhanced Raman spectroscopy reveals dynamic CO intermediates during electrochemical CO_2 reduction on copper. Angew. Chem. Int. Ed. **60**, 16576–16584 (2021). https://doi.org/10.1002/anie.202104114
43. Ma, T., Fan, Q., Li, X., et al.: Graphene-based materials for electrochemical CO_2 reduction. J. CO_2 Util. **30**, 168–182 (2019). https://doi.org/10.1016/j.jcou.2019.02.001
44. Ou, L.H., Chen, Y.D., Jin, J.L.: The origin of CO_2 electroreduction into C_1 and C_2 species: mechanistic understanding on the product selectivity of Cu single-crystal faces. Chem. Phys. Lett. **710**, 175–179 (2018). https://doi.org/10.1016/j.cplett.2018.09.008
45. Montoya, J.H., Shi, C., Chan, K.R., et al.: Theoretical insights into a CO dimerization mechanism in CO_2 electroreduction. J. Phys. Chem. Lett. **6**, 2032–2037 (2015). https://doi.org/10.1021/acs.jpclett.5b00722
46. Li, J., Chang, K., Zhang, H.C., et al.: Effectively increased efficiency for electroreduction of carbon monoxide using supported polycrystalline copper powder electrocatalysts. ACS Catal. **9**, 4709–4718 (2019). https://doi.org/10.1021/acscatal.9b00099
47. Zhang, H.C., Li, J., Cheng, M.J., et al.: CO electroreduction: current development and understanding of Cu-based catalysts. ACS Catal. **9**, 49–65 (2019). https://doi.org/10.1021/acscatal.8b03780
48. Schreier, M., Yoon, Y., Jackson, M.N., et al.: Competition between H and CO for active sites governs copper-mediated electrosynthesis of hydrocarbon fuels. Angew. Chem. Int. Ed. **57**, 10221–10225 (2018). https://doi.org/10.1002/anie.201806051
49. Zheng, Y., Vasileff, A., Zhou, X.L., et al.: Understanding the roadmap for electrochemical reduction of CO_2 to multi-carbon oxygenates and hydrocarbons on copper-based catalysts. J. Am. Chem. Soc. **141**, 7646–7659 (2019). https://doi.org/10.1021/jacs.9b02124
50. Kibria, M.G., Edwards, J.P., Gabardo, C.M., et al.: Electrochemical CO_2 reduction into chemical feedstocks: from mechanistic electrocatalysis models to system design. Adv. Mater. **31**, 1807166 (2019). https://doi.org/10.1002/adma.201807166
51. Kou, Z.K., Li, X., Wang, T.T., et al.: Fundamentals, on-going advances and challenges of electrochemical carbon dioxide reduction. Electrochem. Energy Rev. **5**, 82–111 (2022). https://doi.org/10.1007/s41918-021-00096-5
52. Friebe, P., Bogdanoff, P., Alonso-Vante, N., et al.: A real-time mass spectroscopy study of the (electro)chemical factors affecting CO_2 reduction at copper. J. Catal. **168**, 374–385 (1997). https://doi.org/10.1006/jcat.1997.1606
53. Zhou, Y., Che, F., Liu, M., et al.: Dopant-induced electron localization drives CO_2 reduction to C_2 hydrocarbons. Nat. Chem. **10**, 974–980 (2018). https://doi.org/10.1038/s41557-018-0092-x
54. Schouten, K.J.P., Kwon, Y., van der Ham, C.J.M., et al.: A new mechanism for the selectivity to C_1 and C_2 species in the electrochemical reduction of carbon dioxide on copper electrodes. Chem. Sci. **2**, 1902 (2011). https://doi.org/10.1039/c1sc00277e

55. Schouten, K.J.P., Qin, Z.S., Pérez Gallent, E., et al.: Two pathways for the formation of ethylene in CO reduction on single-crystal copper electrodes. J. Am. Chem. Soc. **134**, 9864–9867 (2012). https://doi.org/10.1021/ja302668n
56. Pérez-Gallent, E., Figueiredo, M.C., Calle-Vallejo, F., et al.: Spectroscopic observation of a hydrogenated CO dimer intermediate during CO reduction on Cu(100) electrodes. Angew. Chem. Int. Ed. **56**, 3621–3624 (2017). https://doi.org/10.1002/anie.201700580
57. Peterson, A.A., Abild-Pedersen, F., Studt, F., et al.: How copper catalyzes the electroreduction of carbon dioxide into hydrocarbon fuels. Energy Environ. Sci. **3**, 1311–1315 (2010). https://doi.org/10.1039/c0ee00071j
58. Hori, Y., Takahashi, R., Yoshinami, Y., et al.: Electrochemical reduction of CO at a copper electrode. J. Phys. Chem. B **101**, 7075–7081 (1997). https://doi.org/10.1021/jp970284i
59. Ren, D., Ang, B.S.H., Yeo, B.S.: Tuning the selectivity of carbon dioxide electroreduction toward ethanol on oxide-derived Cu_xZn catalysts. ACS Catal. **6**, 8239–8247 (2016). https://doi.org/10.1021/acscatal.6b02162
60. Ma, S.C., Sadakiyo, M., Luo, R., et al.: One-step electrosynthesis of ethylene and ethanol from CO_2 in an alkaline electrolyzer. J. Power Sources **301**, 219–228 (2016). https://doi.org/10.1016/j.jpowsour.2015.09.124
61. Ting, L.R.L., Piqué, O., Lim, S.Y., et al.: Enhancing CO_2 electroreduction to ethanol on copper-silver composites by opening an alternative catalytic pathway. ACS Catal. **10**, 4059–4069 (2020). https://doi.org/10.1021/acscatal.9b05319
62. Ma, W., Xie, S., Liu, T., et al.: Electrocatalytic reduction of CO_2 to ethylene and ethanol through hydrogen-assisted C–C coupling over fluorine-modified copper. Nat. Catal. **3**, 478–487 (2020). https://doi.org/10.1038/s41929-020-0450-0
63. Zhang, G.R., Straub, S.D., Shen, L.L., et al.: Probing CO_2 reduction pathways for copper catalysis using an ionic liquid as a chemical trapping agent. Angew. Chem. Int. Ed. **59**, 18095–18102 (2020). https://doi.org/10.1002/anie.202009498
64. Ledezma-Yanez, I., Gallent, E.P., Koper, M.T.M., et al.: Structure-sensitive electroreduction of acetaldehyde to ethanol on copper and its mechanistic implications for CO and CO_2 reduction. Catal. Today **262**, 90–94 (2016). https://doi.org/10.1016/j.cattod.2015.09.029
65. Ma, M., Djanashvili, K., Smith, W.A.: Controllable hydrocarbon formation from the electrochemical reduction of CO_2 over Cu nanowire arrays. Angew. Chem. Int. Ed. **55**, 6680–6684 (2016). https://doi.org/10.1002/anie.201601282
66. Handoko, A.D., Chan, K.W., Yeo, B.S.: $-CH_3$ mediated pathway for the electroreduction of CO_2 to ethane and ethanol on thick oxide-derived copper catalysts at low overpotentials. ACS Energy Lett. **2**, 2103–2109 (2017). https://doi.org/10.1021/acsenergylett.7b00514
67. Sen, S., Liu, D., Palmore, G.T.R.: Electrochemical reduction of CO_2 at copper nanofoams. ACS Catal. **4**, 3091–3095 (2014). https://doi.org/10.1021/cs500522g
68. Li, C.W., Kanan, M.W.: CO_2 reduction at low overpotential on Cu electrodes resulting from the reduction of thick Cu_2O films. J. Am. Chem. Soc. **134**, 7231–7234 (2012). https://doi.org/10.1021/ja3010978
69. Tang, W., Peterson, A.A., Varela, A.S., et al.: The importance of surface morphology in controlling the selectivity of polycrystalline copper for CO_2 electroreduction. Phys. Chem. Chem. Phys. **14**, 76–81 (2012). https://doi.org/10.1039/c1cp22700a
70. Kas, R., Kortlever, R., Milbrat, A., et al.: Electrochemical CO_2 reduction on Cu_2O-derived copper nanoparticles: controlling the catalytic selectivity of hydrocarbons. Phys. Chem. Chem. Phys. **16**, 12194–12201 (2014). https://doi.org/10.1039/c4cp01520g
71. Wang, H., Matios, E., Wang, C.L., et al.: Rapid and scalable synthesis of cuprous halide-derived copper nano-architectures for selective electrochemical reduction of carbon dioxide. Nano Lett. **19**, 3925–3932 (2019). https://doi.org/10.1021/acs.nanolett.9b01197
72. Chen, C.S., Wan, J.H., Yeo, B.S.: Electrochemical reduction of carbon dioxide to ethane using nanostructured Cu_2O-derived copper catalyst and palladium(II) chloride. J. Phys. Chem. C **119**, 26875–26882 (2015). https://doi.org/10.1021/acs.jpcc.5b09144
73. Vasileff, A., Zhu, Y.P., Zhi, X., et al.: Electrochemical reduction of CO_2 to ethane through stabilization of an ethoxy intermediate. Angew. Chem. Int. Ed. **59**, 19649–19653 (2020). https://doi.org/10.1002/anie.202004846
74. Bertheussen, E., Verdaguer-Casadevall, A., Ravasio, D., et al.: Acetaldehyde as an intermediate in the electroreduction of carbon monoxide to ethanol on oxide-derived copper. Angew. Chem. Int. Ed. **55**, 1450–1454 (2016). https://doi.org/10.1002/anie.201508851
75. Ren, D., Wong, N.T., Handoko, A.D., et al.: Mechanistic insights into the enhanced activity and stability of agglomerated Cu nanocrystals for the electrochemical reduction of carbon dioxide to n-propanol. J. Phys. Chem. Lett. **7**, 20–24 (2016). https://doi.org/10.1021/acs.jpclett.5b02554
76. Kim, D., Kley, C.S., Li, Y.F., et al.: Copper nanoparticle ensembles for selective electroreduction of CO_2 to C_2–C_3 products. PNAS **114**, 10560–10565 (2017). https://doi.org/10.1073/pnas.1711493114
77. Rahaman, M., Dutta, A., Zanetti, A., et al.: Electrochemical reduction of CO_2 into multicarbon alcohols on activated Cu mesh catalysts: an identical location (IL) study. ACS Catal. **7**, 7946–7956 (2017). https://doi.org/10.1021/acscatal.7b02234
78. Jiang, K., Sandberg, R.B., Akey, A.J., et al.: Metal ion cycling of Cu foil for selective C–C coupling in electrochemical CO_2 reduction. Nat. Catal. **1**, 111–119 (2018). https://doi.org/10.1038/s41929-017-0009-x
79. Zhuang, T.T., Pang, Y.J., Liang, Z.Q., et al.: Copper nanocavities confine intermediates for efficient electrosynthesis of C_3 alcohol fuels from carbon monoxide. Nat. Catal. **1**, 946–951 (2018). https://doi.org/10.1038/s41929-018-0168-4
80. Chen, C.J., Yan, X.P., Liu, S.J., et al.: Highly efficient electroreduction of CO_2 to C_{2+} alcohols on heterogeneous dual active sites. Angew. Chem. Int. Ed. **59**, 16459–16464 (2020). https://doi.org/10.1002/anie.202006847
81. Chang, X.X., Malkani, A., Yang, X., et al.: Mechanistic insights into electroreductive C–C coupling between CO and acetaldehyde into multicarbon products. J. Am. Chem. Soc. **142**, 2975–2983 (2020). https://doi.org/10.1021/jacs.9b11817
82. Rosen, B.A., Salehi-Khojin, A., Thorson, M.R., et al.: Ionic liquid-mediated selective conversion of CO_2 to CO at low overpotentials. Science **334**, 643–644 (2011). https://doi.org/10.1126/science.1209786
83. Sun, L.Y., Ramesha, G.K., Kamat, P.V., et al.: Switching the reaction course of electrochemical CO_2 reduction with ionic liquids. Langmuir **30**, 6302–6308 (2014). https://doi.org/10.1021/la5009076
84. Li, J.W., Prentice, G.: Electrochemical synthesis of methanol from CO_2 in high-pressure electrolyte. J. Electrochem. Soc. **144**, 4284–4288 (1997). https://doi.org/10.1149/1.1838179
85. Kaneco, S., Iiba, K., Katsumata, H., et al.: Electrochemical reduction of high pressure CO_2 at a Cu electrode in cold methanol. Electrochim. Acta **51**, 4880–4885 (2006). https://doi.org/10.1016/j.electacta.2006.01.032
86. Wang, Y.H., Liu, J.L., Wang, Y.F., et al.: Tuning of CO_2 reduction selectivity on metal electrocatalysts. Small **13**, 1701809 (2017). https://doi.org/10.1002/smll.201701809

87. Varela, A.S.: The importance of pH in controlling the selectivity of the electrochemical CO_2 reduction. Curr. Opin. Green Sustain. Chem. **26**, 100371 (2020). https://doi.org/10.1016/j.cogsc.2020.100371
88. Dinh, C.T., Burdyny, T., Kibria, M.G., et al.: CO_2 electroreduction to ethylene via hydroxide-mediated copper catalysis at an abrupt interface. Science **360**, 783–787 (2018). https://doi.org/10.1126/science.aas9100
89. Wang, L., Nitopi, S.A., Bertheussen, E., et al.: Electrochemical carbon monoxide reduction on polycrystalline copper: effects of potential, pressure, and pH on selectivity toward multicarbon and oxygenated products. ACS Catal. **8**, 7445–7454 (2018). https://doi.org/10.1021/acscatal.8b01200
90. Goodpaster, J.D., Bell, A.T., Head-Gordon, M.: Identification of possible pathways for C–C bond formation during electrochemical reduction of CO_2: new theoretical insights from an improved electrochemical model. J. Phys. Chem. Lett. **7**, 1471–1477 (2016). https://doi.org/10.1021/acs.jpclett.6b00358
91. Hori, Y., Takahashi, I., Koga, O., et al.: Selective formation of C_2 compounds from electrochemical reduction of CO_2 at a series of copper single crystal electrodes. J. Phys. Chem. B **106**, 15–17 (2002). https://doi.org/10.1021/jp013478d
92. Schouten, K.J.P., Pérez Gallent, E., Koper, M.T.M.: The influence of pH on the reduction of CO and CO_2 to hydrocarbons on copper electrodes. J. Electroanal. Chem. **716**, 53–57 (2014). https://doi.org/10.1016/j.jelechem.2013.08.033
93. Dunwell, M., Yang, X., Setzler, B.P., et al.: Examination of near-electrode concentration gradients and kinetic impacts on the electrochemical reduction of CO_2 using surface-enhanced infrared spectroscopy. ACS Catal. **8**, 3999–4008 (2018). https://doi.org/10.1021/acscatal.8b01032
94. Kas, R., Kortlever, R., Yılmaz, H., et al.: Manipulating the hydrocarbon selectivity of copper nanoparticles in CO_2 electroreduction by process conditions. ChemElectroChem **2**, 354–358 (2015). https://doi.org/10.1002/celc.201402373
95. Varela, A.S., Kroschel, M., Reier, T., et al.: Controlling the selectivity of CO_2 electroreduction on copper: the effect of the electrolyte concentration and the importance of the local pH. Catal. Today **260**, 8–13 (2016). https://doi.org/10.1016/j.cattod.2015.06.009
96. Todorova, T.K., Schreiber, M.W., Fontecave, M.: Mechanistic understanding of CO_2 reduction reaction (CO_2RR) toward multicarbon products by heterogeneous copper-based catalysts. ACS Catal. **10**, 1754–1768 (2020). https://doi.org/10.1021/acscatal.9b04746
97. Xiao, H., Cheng, T., Goddard, W.A., III., et al.: Mechanistic explanation of the pH dependence and onset potentials for hydrocarbon products from electrochemical reduction of CO on Cu (111). J. Am. Chem. Soc. **138**, 483–486 (2016). https://doi.org/10.1021/jacs.5b11390
98. Garg, S., Li, M.R., Weber, A.Z., et al.: Advances and challenges in electrochemical CO_2 reduction processes: an engineering and design perspective looking beyond new catalyst materials. J. Mater. Chem. A **8**, 1511–1544 (2020). https://doi.org/10.1039/c9ta13298h
99. Jouny, M., Luc, W., Jiao, F.: High-rate electroreduction of carbon monoxide to multi-carbon products. Nat. Catal. **1**, 748–755 (2018). https://doi.org/10.1038/s41929-018-0133-2
100. Li, J., Wu, D.H., Malkani, A.S., et al.: Hydroxide is not a promoter of C_{2+} product formation in the electrochemical reduction of CO on copper. Angew. Chem. Int. Ed. **59**, 4464–4469 (2020). https://doi.org/10.1002/anie.201912412
101. Nitopi, S., Bertheussen, E., Scott, S.B., et al.: Progress and perspectives of electrochemical CO_2 reduction on copper in aqueous electrolyte. Chem. Rev. **119**, 7610–7672 (2019). https://doi.org/10.1021/acs.chemrev.8b00705
102. Murata, A., Hori, Y.: Product selectivity affected by cationic species in electrochemical reduction of CO_2 and CO at a Cu electrode. Bull. Chem. Soc. Jpn. **64**, 123–127 (1991). https://doi.org/10.1246/bcsj.64.123
103. Thorson, M.R., Siil, K.I., Kenis, P.J.A.: Effect of cations on the electrochemical conversion of CO_2 to CO. J. Electrochem. Soc. **160**, F69–F74 (2012). https://doi.org/10.1149/2.052301jes
104. Kim, H., Park, H.S., Hwang, Y.J., et al.: Surface-morphology-dependent electrolyte effects on gold-catalyzed electrochemical CO_2 reduction. J. Phys. Chem. C **121**, 22637–22643 (2017). https://doi.org/10.1021/acs.jpcc.7b06286
105. Liu, M., Pang, Y., Zhang, B., et al.: Enhanced electrocatalytic CO_2 reduction via field-induced reagent concentration. Nature **537**, 382–386 (2016). https://doi.org/10.1038/nature19060
106. Chen, L.D., Urushihara, M., Chan, K.R., et al.: Electric field effects in electrochemical CO_2 reduction. ACS Catal. **6**, 7133–7139 (2016). https://doi.org/10.1021/acscatal.6b02299
107. Bagger, A., Arnarson, L., Hansen, M.H., et al.: Electrochemical CO reduction: a property of the electrochemical interface. J. Am. Chem. Soc. **141**, 1506–1514 (2019). https://doi.org/10.1021/jacs.8b08839
108. Ringe, S., Clark, E.L., Resasco, J., et al.: Understanding cation effects in electrochemical CO_2 reduction. Energy Environ. Sci. **12**, 3001–3014 (2019). https://doi.org/10.1039/c9ee01341e
109. Pérez-Gallent, E., Marcandalli, G., Figueiredo, M.C., et al.: Structure- and potential-dependent cation effects on CO reduction at copper single-crystal electrodes. J. Am. Chem. Soc. **139**, 16412–16419 (2017). https://doi.org/10.1021/jacs.7b10142
110. Gao, D.F., McCrum, I.T., Deo, S., et al.: Activity and selectivity control in CO_2 electroreduction to multicarbon products over CuO_x catalysts via electrolyte design. ACS Catal. **8**, 10012–10020 (2018). https://doi.org/10.1021/acscatal.8b02587
111. Lum, Y., Yue, B.B., Lobaccaro, P., et al.: Optimizing C–C coupling on oxide-derived copper catalysts for electrochemical CO_2 reduction. J. Phys. Chem. C **121**, 14191–14203 (2017). https://doi.org/10.1021/acs.jpcc.7b03673
112. Bohra, D., Chaudhry, J.H., Burdyny, T., et al.: Modeling the electrical double layer to understand the reaction environment in a CO_2 electrocatalytic system. Energy Environ. Sci. **12**, 3380–3389 (2019). https://doi.org/10.1039/c9ee02485a
113. Singh, M.R., Kwon, Y., Lum, Y., et al.: Hydrolysis of electrolyte cations enhances the electrochemical reduction of CO_2 over Ag and Cu. J. Am. Chem. Soc. **138**, 13006–13012 (2016). https://doi.org/10.1021/jacs.6b07612
114. Roth, J.D., Weaver, M.J.: Role of double-layer cation on the potential-dependent stretching frequencies and binding geometries of carbon monoxide at platinum-nonaqueous interfaces. Langmuir **8**, 1451–1458 (1992). https://doi.org/10.1021/la00041a034
115. Li, J.Y., Li, X., Gunathunge, C.M., et al.: Hydrogen bonding steers the product selectivity of electrocatalytic CO reduction. PNAS **116**, 9220–9229 (2019). https://doi.org/10.1073/pnas.1900761116
116. Malkani, A.S., Li, J., Oliveira, N.J., et al.: Understanding the electric and nonelectric field components of the cation effect on the electrochemical CO reduction reaction. Sci. Adv. **6**, eabd2569 (2020). https://doi.org/10.1126/sciadv.abd2569
117. Gu, Z.X., Shen, H., Shang, L.M., et al.: Nanostructured copper-based electrocatalysts for CO_2 reduction. Small Methods **2**, 1800121 (2018). https://doi.org/10.1002/smtd.201800121
118. Ross, M.B., de Luna, P., Li, Y., et al.: Designing materials for electrochemical carbon dioxide recycling. Nat. Catal. **2**, 648–658 (2019). https://doi.org/10.1038/s41929-019-0306-7
119. Roberts, F.S., Kuhl, K.P., Nilsson, A.: High selectivity for ethylene from carbon dioxide reduction over copper nanocube

electrocatalysts. Angew. Chem. Int. Ed. **54**, 5179–5182 (2015). https://doi.org/10.1002/anie.201412214
120. Durand, W.J., Peterson, A.A., Studt, F., et al.: Structure effects on the energetics of the electrochemical reduction of CO_2 by copper surfaces. Surf. Sci. **605**, 1354–1359 (2011). https://doi.org/10.1016/j.susc.2011.04.028
121. Wang, Y.F., Han, P., Lv, X.M., et al.: Defect and interface engineering for aqueous electrocatalytic CO_2 reduction. Joule **2**, 2551–2582 (2018). https://doi.org/10.1016/j.joule.2018.09.021
122. Baturina, O.A., Lu, Q., Padilla, M.A., et al.: CO_2 electroreduction to hydrocarbons on carbon-supported Cu nanoparticles. ACS Catal. **4**, 3682–3695 (2014). https://doi.org/10.1021/cs500537y
123. Choi, C., Kwon, S., Cheng, T., et al.: Highly active and stable stepped Cu surface for enhanced electrochemical CO_2 reduction to C_2H_4. Nat. Catal. **3**, 804–812 (2020). https://doi.org/10.1038/s41929-020-00504-x
124. Hori, Y., Takahashi, I., Koga, O., et al.: Electrochemical reduction of carbon dioxide at various series of copper single crystal electrodes. J. Mol. Catal. A Chem. **199**, 39–47 (2003). https://doi.org/10.1016/S1381-1169(03)00016-5
125. Schouten, K.J.P., Pérez Gallent, E., Koper, M.T.M.: Structure sensitivity of the electrochemical reduction of carbon monoxide on copper single crystals. ACS Catal. **3**, 1292–1295 (2013). https://doi.org/10.1021/cs4002404
126. Hahn, C., Hatsukade, T., Kim, Y.G., et al.: Engineering Cu surfaces for the electrocatalytic conversion of CO_2: controlling selectivity toward oxygenates and hydrocarbons. PNAS **114**, 5918–5923 (2017). https://doi.org/10.1073/pnas.1618935114
127. Arán-Ais, R.M., Scholten, F., Kunze, S., et al.: The role of in situ generated morphological motifs and Cu(I) species in C_{2+} product selectivity during CO_2 pulsed electroreduction. Nat. Energy **5**, 317–325 (2020). https://doi.org/10.1038/s41560-020-0594-9
128. Chen, C.J., Sun, X.F., Yan, X.P., et al.: A strategy to control the grain boundary density and Cu^+/Cu^0 ratio of Cu-based catalysts for efficient electroreduction of CO_2 to C_2 products. Green Chem. **22**, 1572–1576 (2020). https://doi.org/10.1039/d0gc00247j
129. Yang, W.F., Dastafkan, K., Jia, C., et al.: Design of electrocatalysts and electrochemical cells for carbon dioxide reduction reactions. Adv. Mater. Technol. **3**, 1700377 (2018). https://doi.org/10.1002/admt.201700377
130. Chen, Z.Q., Wang, T., Liu, B., et al.: Grain-boundary-rich copper for efficient solar-driven electrochemical CO_2 reduction to ethylene and ethanol. J. Am. Chem. Soc. **142**, 6878–6883 (2020). https://doi.org/10.1021/jacs.0c00971
131. Feng, H.F., Xu, X., Du, Y., et al.: Application of scanning tunneling microscopy in electrocatalysis and electrochemistry. Electrochem. Energy Rev. **4**, 249–268 (2021). https://doi.org/10.1007/s41918-020-00074-3
132. Lai, W.C., Ma, Z.S., Zhang, J.W., et al.: Dynamic evolution of active sites in electrocatalytic CO_2 reduction reaction: fundamental understanding and recent progress. Adv. Funct. Mater. (2022). https://doi.org/10.1002/adfm.202111193
133. Kim, Y.G., Baricuatro, J.H., Javier, A., et al.: The evolution of the polycrystalline copper surface, first to Cu(111) and then to Cu(100), at a fixed CO_2RR potential: a study by operando EC-STM. Langmuir **30**, 15053–15056 (2014). https://doi.org/10.1021/la504445g
134. Kwon, S., Kim, Y.G., Baricuatro, J.H., et al.: Dramatic change in the step edges of the Cu(100) electrocatalyst upon exposure to CO: operando observations by electrochemical STM and explanation using quantum mechanical calculations. ACS Catal. **11**, 12068–12074 (2021). https://doi.org/10.1021/acscatal.1c02844
135. Kim, Y.G., Baricuatro, J.H., Soriaga, M.P.: Surface reconstruction of polycrystalline Cu electrodes in aqueous $KHCO_3$ electrolyte at potentials in the early stages of CO_2 reduction. Electrocatalysis **9**, 526–530 (2018). https://doi.org/10.1007/s12678-018-0469-z
136. Grosse, P., Gao, D.F., Scholten, F., et al.: Dynamic changes in the structure, chemical state and catalytic selectivity of Cu nanocubes during CO_2 electroreduction: size and support effects. Angew. Chem. Int. Ed. **57**, 6192–6197 (2018). https://doi.org/10.1002/anie.201802083
137. Simon, G.H., Kley, C.S., Roldan Cuenya, B.: Potential-dependent morphology of copper catalysts during CO_2 electroreduction revealed by in situ atomic force microscopy. Angew. Chem. Int. Ed. **60**, 2561–2568 (2021). https://doi.org/10.1002/anie.202010449
138. Zhu, C.Y., Zhang, Z.B., Zhong, L.X., et al.: Product-specific active site motifs of Cu for electrochemical CO_2 reduction. Chem **7**, 406–420 (2021). https://doi.org/10.1016/j.chempr.2020.10.018
139. Vavra, J., Shen, T.H., Stoian, D., et al.: Real-time monitoring reveals dissolution/redeposition mechanism in copper nanocatalysts during the initial stages of the CO_2 reduction reaction. Angew. Chem. Int. Ed. **60**, 1347–1354 (2021). https://doi.org/10.1002/anie.202011137
140. Scholten, F., Nguyen, K.L.C., Bruce, J.P., et al.: Identifying structure-selectivity correlations in the electrochemical reduction of CO_2: a comparison of well-ordered atomically clean and chemically etched copper single-crystal surfaces. Angew. Chem. Int. Ed. **60**, 19169–19175 (2021). https://doi.org/10.1002/anie.202103102
141. Wu, Y.Z., Cao, S.Y., Hou, J.G., et al.: Rational design of nanocatalysts with nonmetal species modification for electrochemical CO_2 reduction. Adv. Energy Mater. **10**, 2070123 (2020). https://doi.org/10.1002/aenm.202070123
142. Long, C., Li, X., Guo, J., et al.: Electrochemical reduction of CO_2 over heterogeneous catalysts in aqueous solution: recent progress and perspectives. Small Methods (2018). https://doi.org/10.1002/smtd.201800369
143. Guan, A.X., Chen, Z., Quan, Y.L., et al.: Boosting CO_2 electroreduction to CH_4 via tuning neighboring single-copper sites. ACS Energy Lett. **5**, 1044–1053 (2020). https://doi.org/10.1021/acsenergylett.0c00018
144. Yang, H.P., Lin, Q., Zhang, C., et al.: Carbon dioxide electroreduction on single-atom nickel decorated carbon membranes with industry compatible current densities. Nat. Commun. **11**, 593 (2020). https://doi.org/10.1038/s41467-020-14402-0
145. Karapinar, D., Huan, N.T., Ranjbar Sahraie, N., et al.: Electroreduction of CO_2 on single-site copper-nitrogen-doped carbon material: selective formation of ethanol and reversible restructuration of the metal sites. Angew. Chem. Int. Ed. **58**, 15098–15103 (2019). https://doi.org/10.1002/anie.201907994
146. Yang, H.P., Lin, Q., Wu, Y., et al.: Highly efficient utilization of single atoms via constructing 3D and free-standing electrodes for CO_2 reduction with ultrahigh current density. Nano Energy **70**, 104454 (2020). https://doi.org/10.1016/j.nanoen.2020.104454
147. Jiao, Y., Zheng, Y., Chen, P., et al.: Molecular scaffolding strategy with synergistic active centers to facilitate electrocatalytic CO_2 reduction to hydrocarbon/alcohol. J. Am. Chem. Soc. **139**, 18093–18100 (2017). https://doi.org/10.1021/jacs.7b10817
148. Zhang, Z., Xiao, J.P., Chen, X.J., et al.: Reaction mechanisms of well-defined metal-N_4 sites in electrocatalytic CO_2 reduction. Angew. Chem. Int. Ed. **57**, 16339–16342 (2018). https://doi.org/10.1002/anie.201808593
149. Yang, H.P., Wu, Y., Li, G.D., et al.: Scalable production of efficient single-atom copper decorated carbon membranes for CO_2 electroreduction to methanol. J. Am. Chem. Soc. **141**, 12717–12723 (2019). https://doi.org/10.1021/jacs.9b04907
150. Zhao, K., Nie, X., Wang, H., et al.: Selective electroreduction of CO_2 to acetone by single copper atoms anchored on N-doped

porous carbon. Nat. Commun. **11**, 2455 (2020). https://doi.org/10.1038/s41467-020-16381-8
151. Wang, J., Gan, L.Y., Zhang, Q.W., et al.: A water-soluble Cu complex as molecular catalyst for electrocatalytic CO_2 reduction on graphene-based electrodes. Adv. Energy Mater. **9**, 1803151 (2019). https://doi.org/10.1002/aenm.201803151
152. Jiang, Z.L., Wang, T., Pei, J.J., et al.: Discovery of main group single Sb–N_4 active sites for CO_2 electroreduction to formate with high efficiency. Energy Environ. Sci. **13**, 2856–2863 (2020). https://doi.org/10.1039/d0ee01486a
153. Zhang, J.C., Cai, W.Z., Hu, F.X., et al.: Recent advances in single atom catalysts for the electrochemical carbon dioxide reduction reaction. Chem. Sci. **12**, 6800–6819 (2021). https://doi.org/10.1039/d1sc01375k
154. Zhang, X., Liu, J.X., Zijlstra, B., et al.: Optimum Cu nanoparticle catalysts for CO_2 hydrogenation towards methanol. Nano Energy **43**, 200–209 (2018). https://doi.org/10.1016/j.nanoen.2017.11.021
155. Dong, H.L., Liu, C., Li, Y.Y., et al.: Computational screening of M/Cu core/shell nanoparticles and their applications for the electro-chemical reduction of CO_2 and CO. Nanoscale **11**, 11351–11359 (2019). https://doi.org/10.1039/c9nr01936g
156. Hu, Q., Han, Z., Wang, X.D., et al.: Facile synthesis of sub-nanometric copper clusters by double confinement enables selective reduction of carbon dioxide to methane. Angew. Chem. Int. Ed. **59**, 19054–19059 (2020). https://doi.org/10.1002/anie.202009277
157. Reske, R., Mistry, H., Behafarid, F., et al.: Particle size effects in the catalytic electroreduction of CO_2 on Cu nanoparticles. J. Am. Chem. Soc. **136**, 6978–6986 (2014). https://doi.org/10.1021/ja500328k
158. Choi, C., Cheng, T., Flores Espinosa, M., et al.: A highly active star decahedron Cu nanocatalyst for hydrocarbon production at low overpotentials. Adv. Mater. **31**, e1805405 (2019). https://doi.org/10.1002/adma.201805405
159. Loiudice, A., Lobaccaro, P., Kamali, E.A., et al.: Tailoring copper nanocrystals towards C_2 products in electrochemical CO_2 reduction. Angew. Chem. Int. Ed. **55**, 5789–5792 (2016). https://doi.org/10.1002/anie.201601582
160. Zhang, H.Y., Zhang, Y.J., Li, Y.Y., et al.: Cu nanowire-catalyzed electrochemical reduction of CO or CO_2. Nanoscale **11**, 12075–12079 (2019). https://doi.org/10.1039/c9nr03170g
161. Zhang, Y.S., Cai, Z., Zhao, Y.X., et al.: Superaerophilic copper nanowires for efficient and switchable CO_2 electroreduction. Nanoscale Horizons **4**, 490–494 (2019). https://doi.org/10.1039/c8nh00259b
162. Lyu, Z.H., Zhu, S.Q., Xie, M.H., et al.: Controlling the surface oxidation of cu nanowires improves their catalytic selectivity and stability toward C_{2+} products in CO_2 reduction. Angew. Chem. Int. Ed. **60**, 1909–1915 (2021). https://doi.org/10.1002/anie.202011956
163. Li, Y.F., Cui, F., Ross, M.B., et al.: Structure-sensitive CO_2 electroreduction to hydrocarbons on ultrathin 5-fold twinned copper nanowires. Nano Lett. **17**, 1312–1317 (2017). https://doi.org/10.1021/acs.nanolett.6b05287
164. Ke, F.S., Liu, X.C., Wu, J.J., et al.: Selective formation of C_2 products from the electrochemical conversion of CO_2 on CuO-derived copper electrodes comprised of nanoporous ribbon arrays. Catal. Today **288**, 18–23 (2017). https://doi.org/10.1016/j.cattod.2016.10.001
165. Guo, C.Y., He, P., Cui, R.R., et al.: Electrochemical CO_2 reduction using electrons generated from photoelectrocatalytic phenol oxidation. Adv. Energy Mater. **9**, 1900364 (2019). https://doi.org/10.1002/aenm.201900364
166. Cai, Z., Zhang, Y.S., Zhao, Y.X., et al.: Selectivity regulation of CO_2 electroreduction through contact interface engineering on superwetting Cu nanoarray electrodes. Nano Res. **12**, 345–349 (2019). https://doi.org/10.1007/s12274-018-2221-7
167. Yang, H.P., Wang, X.D., Hu, Q., et al.: Recent progress in self-supported catalysts for CO_2 electrochemical reduction. Small Methods **4**, 1900826 (2020). https://doi.org/10.1002/smtd.201900826
168. Cheng, Z., Wang, X.D., Yang, H.P., et al.: Construction of cobalt-copper bimetallic oxide heterogeneous nanotubes for high-efficient and low-overpotential electrochemical CO_2 reduction. J. Energy Chem. **54**, 1–6 (2021). https://doi.org/10.1016/j.jechem.2020.04.018
169. Ma, M., Djanashvili, K., Smith, W.A.: Selective electrochemical reduction of CO_2 to CO on CuO-derived Cu nanowires. Phys. Chem. Chem. Phys. **17**, 20861–20867 (2015). https://doi.org/10.1039/c5cp03559g
170. Raciti, D., Livi, K.J., Wang, C.: Highly dense Cu nanowires for low-overpotential CO_2 reduction. Nano Lett. **15**, 6829–6835 (2015). https://doi.org/10.1021/acs.nanolett.5b03298
171. Zhao, Y., Wang, C.Y., Wallace, G.G.: Tin nanoparticles decorated copper oxide nanowires for selective electrochemical reduction of aqueous CO_2 to CO. J. Mater. Chem. A **4**, 10710–10718 (2016). https://doi.org/10.1039/c6ta04155h
172. Cao, L., Raciti, D., Li, C.Y., et al.: Mechanistic insights for low-overpotential electroreduction of CO_2 to CO on copper nanowires. ACS Catal. **7**, 8578–8587 (2017). https://doi.org/10.1021/acscatal.7b03107
173. Azenha, C., Mateos-Pedrero, C., Alvarez-Guerra, M., et al.: Enhancement of the electrochemical reduction of CO_2 to methanol and suppression of H_2 evolution over CuO nanowires. Electrochim. Acta **363**, 137207 (2020). https://doi.org/10.1016/j.electacta.2020.137207
174. Liu, J., Guo, C., Vasileff, A., et al.: Nanostructured 2D materials: Prospective catalysts for electrochemical CO_2 reduction. Small Methods **1**, 2366–9608 (2017). https://doi.org/10.1002/smtd.201600006
175. Pan, J., Sun, Y.M., Deng, P.L., et al.: Hierarchical and ultrathin copper nanosheets synthesized via galvanic replacement for selective electrocatalytic carbon dioxide conversion to carbon monoxide. Appl. Catal. B Environ. **255**, 117736 (2019). https://doi.org/10.1016/j.apcatb.2019.05.038
176. Zhang, B.X., Zhang, J.L., Hua, M.L., et al.: Highly electrocatalytic ethylene production from CO_2 on nanodefective Cu nanosheets. J. Am. Chem. Soc. **142**, 13606–13613 (2020). https://doi.org/10.1021/jacs.0c06420
177. Luc, W., Fu, X., Shi, J., et al.: Two-dimensional copper nanosheets for electrochemical reduction of carbon monoxide to acetate. Nat. Catal. **2**, 423–430 (2019). https://doi.org/10.1038/s41929-019-0269-8
178. Kas, R., Hummadi, K.K., Kortlever, R., et al.: Three-dimensional porous hollow fibre copper electrodes for efficient and high-rate electrochemical carbon dioxide reduction. Nat. Commun. **7**, 10748 (2016). https://doi.org/10.1038/ncomms10748
179. Pang, Y.J., Burdyny, T., Dinh, C.T., et al.: Joint tuning of nanostructured Cu-oxide morphology and local electrolyte programs high-rate CO_2 reduction to C_2H_4. Green Chem. **19**, 4023–4030 (2017). https://doi.org/10.1039/c7gc01677h
180. Dutta, A., Rahaman, M., Mohos, M., et al.: Electrochemical CO_2 conversion using skeleton (sponge) type of Cu catalysts. ACS Catal. **7**, 5431–5437 (2017). https://doi.org/10.1021/acscatal.7b01548
181. Lv, J.J., Jouny, M., Luc, W., et al.: A highly porous copper electrocatalyst for carbon dioxide reduction. Adv. Mater. **30**, 1803111 (2018). https://doi.org/10.1002/adma.201803111
182. Dutta, A., Rahaman, M., Luedi, N.C., et al.: Morphology matters: tuning the product distribution of CO_2 electroreduction

on oxide-derived Cu foam catalysts. ACS Catal. **6**, 3804–3814 (2016). https://doi.org/10.1021/acscatal.6b00770
183. Yang, K.D., Ko, W.R., Lee, J.H., et al.: Morphology-directed selective production of ethylene or ethane from CO_2 on a Cu mesopore electrode. Angew. Chem. Int. Ed. **56**, 796–800 (2017). https://doi.org/10.1002/anie.201610432
184. Wu, M.F., Zhu, C., Wang, K., et al.: Promotion of CO_2 electrochemical reduction via Cu nanodendrites. ACS Appl. Mater. Interfaces **12**, 11562–11569 (2020). https://doi.org/10.1021/acsami.9b21153
185. de Luna, P., Quintero-Bermudez, R., Dinh, C.T., et al.: Catalyst electro-redeposition controls morphology and oxidation state for selective carbon dioxide reduction. Nat. Catal. **1**, 103–110 (2018). https://doi.org/10.1038/s41929-017-0018-9
186. Niu, Z.-Z., Gao, F.-Y., Zhang, X.-L., et al.: Hierarchical copper with inherent hydrophobicity mitigates electrode flooding for high-rate CO_2 electroreduction to multicarbon products. J. Am. Chem. Soc. **143**, 8011–8021 (2021). https://doi.org/10.1021/jacs.1c01190
187. Raciti, D., Cao, L., Livi, K.J.T., et al.: Low-overpotential electroreduction of carbon monoxide using copper nanowires. ACS Catal. **7**, 4467–4472 (2017). https://doi.org/10.1021/acscatal.7b01124
188. Reller, C., Krause, R., Volkova, E., et al.: Selective electroreduction of CO_2 toward ethylene on nano dendritic copper catalysts at high current density. Adv. Energy Mater. **7**, 1602114 (2017). https://doi.org/10.1002/aenm.201602114
189. Eilert, A., Roberts, F.S., Friebel, D., et al.: Formation of copper catalysts for CO_2 reduction with high ethylene/methane product ratio investigated with in situ X-ray absorption spectroscopy. J. Phys. Chem. Lett. **7**, 1466–1470 (2016). https://doi.org/10.1021/acs.jpclett.6b00367
190. Garza, A.J., Bell, A.T., Head-Gordon, M.: Is subsurface oxygen necessary for the electrochemical reduction of CO_2 on copper? J. Phys. Chem. Lett. **9**, 601–606 (2018). https://doi.org/10.1021/acs.jpclett.7b03180
191. Jiao, J., Lin, R., Liu, S., et al.: Copper atom-pair catalyst anchored on alloy nanowires for selective and efficient electrochemical reduction of CO_2. Nat. Chem. **11**, 222–228 (2019). https://doi.org/10.1038/s41557-018-0201-x
192. Gao, D.F., Zegkinoglou, I., Divins, N.J., et al.: Plasma-activated copper nanocube catalysts for efficient carbon dioxide electroreduction to hydrocarbons and alcohols. ACS Nano **11**, 4825–4831 (2017). https://doi.org/10.1021/acsnano.7b01257
193. Kim, D., Lee, S., Ocon, J.D., et al.: Insights into an autonomously formed oxygen-evacuated Cu_2O electrode for the selective production of C_2H_4 from CO_2. Phys. Chem. Chem. Phys. **17**, 824–830 (2015). https://doi.org/10.1039/c4cp03172e
194. Li, C.W., Ciston, J., Kanan, M.W.: Electroreduction of carbon monoxide to liquid fuel on oxide-derived nanocrystalline copper. Nature **508**, 504–507 (2014). https://doi.org/10.1038/nature13249
195. Verdaguer-Casadevall, A., Li, C.W., Johansson, T.P., et al.: Probing the active surface sites for CO reduction on oxide-derived copper electrocatalysts. J. Am. Chem. Soc. **137**, 9808–9811 (2015). https://doi.org/10.1021/jacs.5b06227
196. Feng, X.F., Jiang, K.L., Fan, S.S., et al.: A direct grain-boundary-activity correlation for CO electroreduction on Cu nanoparticles. ACS Central Sci. **2**, 169–174 (2016). https://doi.org/10.1021/acscentsci.6b00022
197. Kwon, Y., Lum, Y., Clark, E.L., et al.: CO_2 electroreduction with enhanced ethylene and ethanol selectivity by nanostructuring polycrystalline copper. ChemElectroChem **3**, 1012–1019 (2016). https://doi.org/10.1002/celc.201600068
198. Lum, Y., Ager, J.W.: Stability of residual oxides in oxide-derived copper catalysts for electrochemical CO_2 reduction investigated with ^{18}O labeling. Angew. Chem. Int. Ed. **57**, 551–554 (2018). https://doi.org/10.1002/anie.201710590
199. Favaro, M., Xiao, H., Cheng, T., et al.: Subsurface oxide plays a critical role in CO_2 activation by Cu(111) surfaces to form chemisorbed CO_2, the first step in reduction of CO_2. PNAS **114**, 6706–6711 (2017). https://doi.org/10.1073/pnas.1701405114
200. Eilert, A., Cavalca, F., Roberts, F.S., et al.: Subsurface oxygen in oxide-derived copper electrocatalysts for carbon dioxide reduction. J. Phys. Chem. Lett. **8**, 285–290 (2017). https://doi.org/10.1021/acs.jpclett.6b02273
201. Lum, Y., Ager, J.W.: Evidence for product-specific active sites on oxide-derived Cu catalysts for electrochemical CO_2 reduction. Nat. Catal. **2**, 86–93 (2019). https://doi.org/10.1038/s41929-018-0201-7
202. Feng, X.F., Jiang, K.L., Fan, S.S., et al.: Grain-boundary-dependent CO_2 electroreduction activity. J. Am. Chem. Soc. **137**, 4606–4609 (2015). https://doi.org/10.1021/ja5130513
203. Ren, D., Deng, Y.L., Handoko, A.D., et al.: Selective electrochemical reduction of carbon dioxide to ethylene and ethanol on copper(I) oxide catalysts. ACS Catal. **5**, 2814–2821 (2015). https://doi.org/10.1021/cs502128q
204. Jeon, H.S., Timoshenko, J., Rettenmaier, C., et al.: Selectivity control of Cu nanocrystals in a gas-fed flow cell through CO_2 pulsed electroreduction. J. Am. Chem. Soc. **143**, 7578–7587 (2021). https://doi.org/10.1021/jacs.1c03443
205. Lee, S.Y., Jung, H., Kim, N.K., et al.: Mixed copper states in anodized Cu electrocatalyst for stable and selective ethylene production from CO_2 reduction. J. Am. Chem. Soc. **140**, 8681–8689 (2018). https://doi.org/10.1021/jacs.8b02173
206. Gao, D.F., Scholten, F., Roldan Cuenya, B.: Improved CO_2 electroreduction performance on plasma-activated Cu catalysts via electrolyte design: halide effect. ACS Catal. **7**, 5112–5120 (2017). https://doi.org/10.1021/acscatal.7b01416
207. Zhong, Y., Xu, Y., Ma, J., et al.: An artificial electrode/electrolyte interface for CO_2 electroreduction by cation surfactant self-assembly. Angew. Chem. Int. Ed. **59**, 19095–19101 (2020). https://doi.org/10.1002/anie.202005522
208. Cheng, N.C., Zhang, L., Doyle-Davis, K., et al.: Single-atom catalysts: from design to application. Electrochem. Energy Rev. **2**, 539–573 (2019). https://doi.org/10.1007/s41918-019-00050-6
209. Wang, J.G., Zhang, F.Q., Kang, X.W., et al.: Organic functionalization of metal catalysts: enhanced activity towards electroreduction of carbon dioxide. Curr. Opin. Electrochem. **13**, 40–46 (2019). https://doi.org/10.1016/j.coelec.2018.10.010
210. Hu, C.G., Xiao, Y., Zou, Y.Q., et al.: Carbon-based metal-free electrocatalysis for energy conversion, energy storage, and environmental protection. Electrochem. Energy Rev. **1**, 238 (2018). https://doi.org/10.1007/s41918-018-0005-0
211. Xie, M.S., Xia, B.Y., Li, Y.W., et al.: Amino acid modified copper electrodes for the enhanced selective electroreduction of carbon dioxide towards hydrocarbons. Energy Environ. Sci. **9**, 1687–1695 (2016). https://doi.org/10.1039/c5ee03694a
212. Ahn, S., Klyukin, K., Wakeham, R.J., et al.: Poly-amide modified copper foam electrodes for enhanced electrochemical reduction of carbon dioxide. ACS Catal. **8**, 4132–4142 (2018). https://doi.org/10.1021/acscatal.7b04347
213. Jia, S.Q., Zhu, Q.G., Chu, M.G., et al.: Hierarchical metal-polymer hybrids for enhanced CO_2 electroreduction. Angew. Chem. Int. Ed. **60**, 10977–10982 (2021). https://doi.org/10.1002/anie.202102193
214. Chen, X., Chen, J., Alghoraibi, N.M., et al.: Electrochemical CO_2-to-ethylene conversion on polyamine-incorporated Cu electrodes. Nat. Catal. **4**, 20–27 (2021). https://doi.org/10.1038/s41929-020-00547-0
215. Wei, X., Yin, Z.L., Lyu, K.J., et al.: Highly selective reduction of CO_2 to C_{2+} hydrocarbons at copper/polyaniline interfaces. ACS

Catal. **10**, 4103–4111 (2020). https://doi.org/10.1021/acscatal.0c00049
216. Zhong, S.H., Yang, X.L., Cao, Z., et al.: Efficient electrochemical transformation of CO_2 to C_2/C_3 chemicals on benzimidazole-functionalized copper surfaces. Chem. Commun. **54**, 11324–11327 (2018). https://doi.org/10.1039/c8cc04735a
217. Han, Z.J., Kortlever, R., Chen, H.Y., et al.: CO_2 reduction selective for $C_{\geqslant 2}$ products on polycrystalline copper with N-substituted pyridinium additives. ACS Cent. Sci. **3**, 853–859 (2017). https://doi.org/10.1021/acscentsci.7b00180
218. Li, F., Thevenon, A., Rosas-Hernández, A., et al.: Molecular tuning of CO_2-to-ethylene conversion. Nature **577**, 509–513 (2020). https://doi.org/10.1038/s41586-019-1782-2
219. Li, F., Li, Y.C., Wang, Z., et al.: Cooperative CO_2-to-ethanol conversion via enriched intermediates at molecule-metal catalyst interfaces. Nat. Catal. **3**, 75–82 (2020). https://doi.org/10.1038/s41929-019-0383-7
220. Gong, M., Cao, Z., Liu, W., et al.: Supramolecular porphyrin cages assembled at molecular-materials interfaces for electrocatalytic CO reduction. ACS Cent. Sci. **3**, 1032–1040 (2017). https://doi.org/10.1021/acscentsci.7b00316
221. Thevenon, A., Rosas-Hernández, A., Peters, J.C., et al.: In-situ nanostructuring and stabilization of polycrystalline copper by an organic salt additive promotes electrocatalytic CO_2 reduction to ethylene. Angew. Chem. Int. Ed. **58**, 16952–16958 (2019). https://doi.org/10.1002/anie.201907935
222. Liu, J., Fu, J.J., Zhou, Y., et al.: Controlled synthesis of edta-modified porous hollow copper microspheres for high-efficiency conversion of CO_2 to multicarbon products. Nano Lett. **20**, 4823–4828 (2020). https://doi.org/10.1021/acs.nanolett.0c00639
223. Chen, C.S., Handoko, A.D., Wan, J.H., et al.: Stable and selective electrochemical reduction of carbon dioxide to ethylene on copper mesocrystals. Catal. Sci. Technol. **5**, 161–168 (2015). https://doi.org/10.1039/c4cy00906a
224. Qin, T., Qian, Y., Zhang, F., et al.: Cloride-derived copper electrode for efficient electrochemical reduction of CO_2 to ethylene. Chin. Chem. Lett. **30**, 314–318 (2019). https://doi.org/10.1016/j.cclet.2018.07.003
225. Kim, T., Palmore, G.T.R.: A scalable method for preparing Cu electrocatalysts that convert CO_2 into C_{2+} products. Nat. Commun. **11**, 3622 (2020). https://doi.org/10.1038/s41467-020-16998-9
226. Gao, D.F., Sinev, I., Scholten, F., et al.: Selective CO_2 electroreduction to ethylene and multicarbon alcohols via electrolyte-driven nanostructuring. Angew. Chem. Int. Ed. **58**, 17047–17053 (2019). https://doi.org/10.1002/anie.201910155
227. Huang, Y., Ong, C.W., Yeo, B.S.: Effects of electrolyte anions on the reduction of carbon dioxide to ethylene and ethanol on copper (100) and (111) surfaces. ChemSusChem **11**, 3299–3306 (2018). https://doi.org/10.1002/cssc.201801078
228. Bai, H.P., Cheng, T., Li, S.Y., et al.: Controllable CO adsorption determines ethylene and methane productions from CO_2 electroreduction. Sci. Bull. **66**, 62–68 (2021). https://doi.org/10.1016/j.scib.2020.06.023
229. He, J.F., Johnson, N.J.J., Huang, A.X., et al.: Electrocatalytic alloys for CO_2 reduction. ChemSusChem **11**, 48–57 (2018). https://doi.org/10.1002/cssc.201701825
230. Gao, D., Arán-Ais, R.M., Jeon, H.S., et al.: Rational catalyst and electrolyte design for CO_2 electroreduction towards multicarbon products. Nat. Catal. **2**, 198–210 (2019). https://doi.org/10.1038/s41929-019-0235-5
231. Vasileff, A., Xu, C.C., Jiao, Y., et al.: Surface and interface engineering in copper-based bimetallic materials for selective CO_2 electroreduction. Chem **4**, 1809–1831 (2018). https://doi.org/10.1016/j.chempr.2018.05.001
232. Kim, C., Dionigi, F., Beermann, V., et al.: Alloy nanocatalysts for the electrochemical oxygen reduction (ORR) and the direct electrochemical carbon dioxide reduction reaction (CO_2RR). Adv. Mater. **31**, 1805617 (2019). https://doi.org/10.1002/adma.201805617
233. Clark, E.L., Hahn, C., Jaramillo, T.F., et al.: Electrochemical CO_2 reduction over compressively strained CuAg surface alloys with enhanced multi-carbon oxygenate selectivity. J. Am. Chem. Soc. **139**, 15848–15857 (2017). https://doi.org/10.1021/jacs.7b08607
234. Chang, C.J., Hung, S.F., Hsu, C.S., et al.: Quantitatively unraveling the redox shuttle of spontaneous oxidation/electroreduction of CuO_x on silver nanowires using in situ X-ray absorption spectroscopy. ACS Cent. Sci. **5**, 1998–2009 (2019). https://doi.org/10.1021/acscentsci.9b01142
235. Gao, J., Zhang, H., Guo, X.Y., et al.: Selective C–C coupling in carbon dioxide electroreduction via efficient spillover of intermediates as supported by operando Raman spectroscopy. J. Am. Chem. Soc. **141**, 18704–18714 (2019). https://doi.org/10.1021/jacs.9b07415
236. Huang, J.F., Mensi, M., Oveisi, E., et al.: Structural sensitivities in bimetallic catalysts for electrochemical CO_2 reduction revealed by Ag–Cu nanodimers. J. Am. Chem. Soc. **141**, 2490–2499 (2019). https://doi.org/10.1021/jacs.8b12381
237. Chen, C.B., Li, Y.F., Yu, S., et al.: Cu–Ag tandem catalysts for high-rate CO_2 electrolysis toward multicarbons. Joule **4**, 1688–1699 (2020). https://doi.org/10.1016/j.joule.2020.07.009
238. Dutta, A., Montiel, I.Z., Erni, R., et al.: Activation of bimetallic AgCu foam electrocatalysts for ethanol formation from CO_2 by selective Cu oxidation/reduction. Nano Energy **68**, 104331 (2020). https://doi.org/10.1016/j.nanoen.2019.104331
239. Herzog, A., Bergmann, A., Jeon, H.S., et al.: Operando investigation of Ag-decorated Cu_2O nanocube catalysts with enhanced CO_2 electroreduction toward liquid products. Angew. Chem. Int. Ed. **60**, 7426–7435 (2021). https://doi.org/10.1002/anie.202017070
240. Wang, X., Wang, Z., Zhuang, T.T., et al.: Efficient upgrading of CO to C_3 fuel using asymmetric C–C coupling active sites. Nat. Commun. **10**, 5186 (2019). https://doi.org/10.1038/s41467-019-13190-6
241. Yang, Y., Ajmal, S., Feng, Y.Q., et al.: Insight into the formation and transfer process of the first intermediate of CO_2 reduction over Ag-decorated dendritic Cu. Chem. A Eur. J. **26**, 4080–4089 (2020). https://doi.org/10.1002/chem.201904063
242. Lv, X.M., Shang, L.M., Zhou, S., et al.: Electron-deficient Cu sites on Cu_3Ag_1 catalyst promoting CO_2 electroreduction to alcohols. Adv. Energy Mater. **10**, 2001987 (2020). https://doi.org/10.1002/aenm.202001987
243. Wang, J.Q., Li, Z., Dong, C.K., et al.: Silver/copper interface for relay electroreduction of carbon dioxide to ethylene. ACS Appl. Mater. Interfaces **11**, 2763–2767 (2019). https://doi.org/10.1021/acsami.8b20545
244. Feng, Y., Li, Z., Liu, H., et al.: Laser-prepared CuZn alloy catalyst for selective electrochemical reduction of CO_2 to ethylene. Langmuir **34**, 13544–13549 (2018). https://doi.org/10.1021/acs.langmuir.8b02837
245. Moreno-García, P., Schlegel, N., Zanetti, A., et al.: Selective electrochemical reduction of CO_2 to CO on Zn-based foams produced by Cu^{2+} and template-assisted electrodeposition. ACS Appl. Mater. Interfaces **10**, 31355–31365 (2018). https://doi.org/10.1021/acsami.8b09894
246. Song, Y.F., Junqueira, J.R.C., Sikdar, N., et al.: B–Cu–Zn gas diffusion electrodes for CO_2 electroreduction to C_{2+} products at high current densities. Angew. Chem. Int. Ed. **60**, 9135–9141 (2021). https://doi.org/10.1002/anie.202016898
247. Ren, D., Gao, J., Pan, L.F., et al.: Atomic layer deposition of ZnO on CuO enables selective and efficient electroreduction of carbon

dioxide to liquid fuels. Angew. Chem. **131**, 15178–15182 (2019). https://doi.org/10.1002/ange.201909610
248. Wang, R.Z., Jiang, R., Dong, C.K., et al.: Engineering a Cu/ZnO_x interface for high methane selectivity in CO_2 electrochemical reduction. Ind. Eng. Chem. Res. **60**, 273–280 (2021). https://doi.org/10.1021/acs.iecr.0c04718
249. Jeon, H.S., Timoshenko, J., Scholten, F., et al.: Operando insight into the correlation between the structure and composition of CuZn nanoparticles and their selectivity for the electrochemical CO_2 reduction. J. Am. Chem. Soc. **141**, 19879–19887 (2019). https://doi.org/10.1021/jacs.9b10709
250. Hou, L., Han, J.Y., Wang, C., et al.: Ag nanoparticle embedded Cu nanoporous hybrid arrays for the selective electrocatalytic reduction of CO_2 towards ethylene. Inorg. Chem. Front. **7**, 2097–2106 (2020). https://doi.org/10.1039/d0qi00025f
251. Kim, D., Resasco, J., Yu, Y., et al.: Synergistic geometric and electronic effects for electrochemical reduction of carbon dioxide using gold-copper bimetallic nanoparticles. Nat. Commun. **5**, 4948 (2014). https://doi.org/10.1038/ncomms5948
252. Kim, D., Xie, C.L., Becknell, N., et al.: Electrochemical activation of CO_2 through atomic ordering transformations of AuCu nanoparticles. J. Am. Chem. Soc. **139**, 8329–8336 (2017). https://doi.org/10.1021/jacs.7b03516
253. Chen, Y., Fan, Z.X., Wang, J., et al.: Ethylene selectivity in electrocatalytic CO_2 reduction on Cu nanomaterials: a crystal phase-dependent study. J. Am. Chem. Soc. **142**, 12760–12766 (2020). https://doi.org/10.1021/jacs.0c04981
254. Shen, S.B., Peng, X.Y., Song, L.D., et al.: AuCu alloy nanoparticle embedded Cu submicrocone arrays for selective conversion of CO_2 to ethanol. Small **15**, 1902229 (2019). https://doi.org/10.1002/smll.201902229
255. Zhu, W.W., Zhao, K.M., Liu, S.Q., et al.: Low-overpotential selective reduction of CO_2 to ethanol on electrodeposited Cu_xAu_y nanowire arrays. J. Energy Chem. **37**, 176–182 (2019). https://doi.org/10.1016/j.jechem.2019.03.030
256. Morales-Guio, C.G., Cave, E.R., Nitopi, S.A., et al.: Improved CO_2 reduction activity towards C_{2+} alcohols on a tandem gold on copper electrocatalyst. Nat. Catal. **1**, 764–771 (2018). https://doi.org/10.1038/s41929-018-0139-9
257. Feng, R.T., Zhu, Q.G., Chu, M.G., et al.: Electrodeposited Cu–Pd bimetallic catalysts for the selective electroreduction of CO_2 to ethylene. Green Chem. **22**, 7560–7565 (2020). https://doi.org/10.1039/d0gc03051a
258. Guo, X., Zhang, Y.X., Deng, C., et al.: Composition dependent activity of Cu–Pt nanocrystals for electrochemical reduction of CO_2. Chem. Commun. **51**, 1345–1348 (2015). https://doi.org/10.1039/c4cc08175g
259. Yin, Z., Gao, D.F., Yao, S.Y., et al.: Highly selective palladium-copper bimetallic electrocatalysts for the electrochemical reduction of CO_2 to CO. Nano Energy **27**, 35–43 (2016). https://doi.org/10.1016/j.nanoen.2016.06.035
260. Zhang, S., Kang, P., Bakir, M., et al.: Polymer-supported CuPd nanoalloy as a synergistic catalyst for electrocatalytic reduction of carbon dioxide to methane. PNAS **112**, 15809–15814 (2015). https://doi.org/10.1073/pnas.1522496112
261. Zhang, X.L., Liu, C.W., Zhao, Y., et al.: Atomic nickel cluster decorated defect-rich copper for enhanced C_2 product selectivity in electrocatalytic CO_2 reduction. Appl. Catal. B Environ. **291**, 120030 (2021). https://doi.org/10.1016/j.apcatb.2021.120030
262. Li, X.D., Wang, S.M., Li, L., et al.: Progress and perspective for in situ studies of CO_2 reduction. J. Am. Chem. Soc. (2020). https://doi.org/10.1021/jacs.0c02973
263. Li, X.X., Blinn, K., Chen, D.C., et al.: In situ and surface-enhanced Raman spectroscopy study of electrode materials in solid oxide fuel cells. Electrochem. Energy Rev. **1**, 433–459 (2018). https://doi.org/10.1007/s41918-018-0017-9
264. He, M., Li, C., Zhang, H., et al.: Oxygen induced promotion of electrochemical reduction of CO_2 via co-electrolysis. Nat. Commun. **11**, 3844 (2020). https://doi.org/10.1038/s41467-020-17690-8
265. Wang, Y.H., Wang, Z.Y., Dinh, C.-T., et al.: Catalyst synthesis under CO_2 electroreduction favours faceting and promotes renewable fuels electrosynthesis. Nat. Catal. **3**, 98–106 (2019). https://doi.org/10.1038/s41929-019-0397-1
266. Jiang, S., Klingan, K., Pasquini, C., et al.: New aspects of operando Raman spectroscopy applied to electrochemical CO_2 reduction on Cu foams. J. Chem. Phys. **150**, 041718 (2018). https://doi.org/10.1063/1.5054109
267. Yang, Y., Ohnoutek, L., Ajmal, S., et al.: "Hot edges" in an inverse opal structure enable efficient CO_2 electrochemical reduction and sensitive in situ Raman characterization. J. Mater. Chem. A **7**, 11836–11846 (2019). https://doi.org/10.1039/c9ta02288k
268. Xu, Z.Z., Liang, Z.B., Guo, W.H., et al.: In situ/operando vibrational spectroscopy for the investigation of advanced nanostructured electrocatalysts. Coord. Chem. Rev. **436**, 213824 (2021). https://doi.org/10.1016/j.ccr.2021.213824
269. Yang, P.P., Zhang, X.L., Gao, F.Y., et al.: Protecting copper oxidation state via intermediate confinement for selective CO_2 electroreduction to C_{2+} fuels. J. Am. Chem. Soc. **142**, 6400–6408 (2020). https://doi.org/10.1021/jacs.0c01699
270. Zhong, D.Z., Zhao, Z.J., Zhao, Q., et al.: Coupling of Cu(100) and (110) facets promotes carbon dioxide conversion to hydrocarbons and alcohols. Angew. Chem. Int. Ed. **60**, 4879–4885 (2021). https://doi.org/10.1002/anie.202015159
271. Phan, T.H., Banjac, K., Cometto, F.P., et al.: Emergence of potential-controlled Cu-nanocuboids and graphene-covered Cu-nanocuboids under operando CO_2 electroreduction. Nano Lett. **21**, 2059–2065 (2021). https://doi.org/10.1021/acs.nanolett.0c04703
272. Tao, Z.X., Wu, Z.S., Wu, Y.S., et al.: Activating copper for electrocatalytic CO_2 reduction to formate via molecular interactions. ACS Catal. **10**, 9271–9275 (2020). https://doi.org/10.1021/acscatal.0c02237
273. Pan, Z.W.H., Wang, K., Ye, K.H., et al.: Intermediate adsorption states switch to selectively catalyze electrochemical CO_2 reduction. ACS Catal. **10**, 3871–3880 (2020). https://doi.org/10.1021/acscatal.9b05115
274. Li, Y., Xu, A., Lum, Y., et al.: Promoting CO_2 methanation via ligand-stabilized metal oxide clusters as hydrogen-donating motifs. Nat. Commun. **11**, 6190 (2020). https://doi.org/10.1038/s41467-020-20004-7
275. Fu, W.L., Liu, Z., Wang, T.Y., et al.: Promoting C_{2+} production from electrochemical CO_2 reduction on shape-controlled cuprous oxide nanocrystals with high-index facets. ACS Sustain. Chem. Eng. **8**, 15223–15229 (2020). https://doi.org/10.1021/acssuschemeng.0c04873
276. Chen, X.Y., Henckel, D.A., Nwabara, U.O., et al.: Controlling speciation during CO_2 reduction on Cu-alloy electrodes. ACS Catal. **10**, 672–682 (2020). https://doi.org/10.1021/acscatal.9b04368
277. Lee, C.W., Shin, S.J., Jung, H., et al.: Metal-oxide interfaces for selective electrochemical C–C coupling reactions. ACS Energy Lett. **4**, 2241–2248 (2019). https://doi.org/10.1021/acsenergylett.9b01721
278. Kottakkat, T., Klingan, K., Jiang, S., et al.: Electrodeposited AgCu foam catalysts for enhanced reduction of CO_2 to CO. ACS Appl. Mater. Interfaces **11**, 14734–14744 (2019). https://doi.org/10.1021/acsami.8b22071
279. Jiang, X.X., Wang, X.K., Liu, Z.J., et al.: A highly selective tin-copper bimetallic electrocatalyst for the electrochemical reduction of aqueous CO_2 to formate. Appl. Catal. B Environ. **259**, 118040 (2019). https://doi.org/10.1016/j.apcatb.2019.118040

280. Deng, Y.L., Huang, Y., Ren, D., et al.: On the role of sulfur for the selective electrochemical reduction of CO_2 to formate on CuS_x catalysts. ACS Appl. Mater. Interfaces **10**, 28572–28581 (2018). https://doi.org/10.1021/acsami.8b08428
281. Mandal, L., Yang, K.R., Motapothula, M.R., et al.: Investigating the role of copper oxide in electrochemical CO_2 reduction in real time. ACS Appl. Mater. Interfaces **10**, 8574–8584 (2018). https://doi.org/10.1021/acsami.7b15418
282. Wu, Z.-Z., Zhang, X.-L., Niu, Z.-Z., et al.: Identification of Cu(100)/Cu(111) interfaces as superior active sites for CO dimerization during CO_2 electroreduction. J. Am. Chem. Soc. **144**, 259–269 (2022). https://doi.org/10.1021/jacs.1c09508
283. Henckel, D.A., Counihan, M.J., Holmes, H.E., et al.: Potential dependence of the local pH in a CO_2 reduction electrolyzer. ACS Catal. **11**, 255–263 (2021). https://doi.org/10.1021/acscatal.0c04297
284. Zhang, Z.S., Melo, L., Jansonius, R.P., et al.: pH matters when reducing CO_2 in an electrochemical flow cell. ACS Energy Lett. **5**, 3101–3107 (2020). https://doi.org/10.1021/acsenergylett.0c01606
285. Yang, H., Hu, Y.W., Chen, J.J., et al.: CO_2 electroreduction: intermediates adsorption engineering of CO_2 electroreduction reaction in highly selective heterostructure Cu-based electrocatalysts for CO production. Adv. Energy Mater. **9**, 1970107 (2019). https://doi.org/10.1002/aenm.201970107
286. Dutta, A., Rahaman, M., Hecker, B., et al.: CO_2 electrolysis - complementary operando XRD, XAS and Raman spectroscopy study on the stability of Cu_xO foam catalysts. J. Catal. **389**, 592–603 (2020). https://doi.org/10.1016/j.jcat.2020.06.024
287. Handoko, A.D., Wei, F., Jenndy, et al.: Understanding heterogeneous electrocatalytic carbon dioxide reduction through operando techniques. Nat. Catal. **1**, 922–934 (2018). https://doi.org/10.1038/s41929-018-0182-6
288. Gunathunge, C.M., Ovalle, V.J., Li, Y.W., et al.: Existence of an electrochemically inert CO population on Cu electrodes in alkaline pH. ACS Catal. **8**, 7507–7516 (2018). https://doi.org/10.1021/acscatal.8b01552
289. Lee, S., Lee, J.: Ethylene selectivity in CO electroreduction when using Cu oxides: an in situ ATR-SEIRAS study. ChemElectroChem **5**, 558–564 (2018). https://doi.org/10.1002/celc.201700892
290. Kim, Y., Park, S., Shin, S.J., et al.: Time-resolved observation of C–C coupling intermediates on Cu electrodes for selective electrochemical CO_2 reduction. Energy Environ. Sci. **13**, 4301–4311 (2020). https://doi.org/10.1039/d0ee01690j
291. Xiong, L.K., Zhang, X., Yuan, H., et al.: Breaking the linear scaling relationship by compositional and structural crafting of ternary Cu–Au/Ag nanoframes for electrocatalytic ethylene production. Angew. Chem. Int. Ed. **60**, 2508–2518 (2021). https://doi.org/10.1002/anie.202012631
292. Malkani, A., Dunwell, M., Xu, B.J.: Operando spectroscopic investigations of copper and oxide-derived copper catalysts for electrochemical CO reduction. ACS Catal. **9**, 474–478 (2019). https://doi.org/10.1021/acscatal.8b04269
293. Hori, Y., Koga, O., Watanabe, Y., et al.: FTIR measurements of charge displacement adsorption of CO on poly- and single crystal (100) of Cu electrodes. Electrochim. Acta **44**, 1389–1395 (1998). https://doi.org/10.1016/S0013-4686(98)00261-8
294. Zhu, S.Q., Jiang, B., Cai, W.B., et al.: Direct observation on reaction intermediates and the role of bicarbonate anions in CO_2 electrochemical reduction reaction on Cu surfaces. J. Am. Chem. Soc. **139**, 15664–15667 (2017). https://doi.org/10.1021/jacs.7b10462
295. Katayama, Y., Nattino, F., Giordano, L., et al.: An In situ surface-enhanced infrared absorption spectroscopy study of electrochemical CO_2 reduction: selectivity dependence on surface C-bound and O-bound reaction intermediates. J. Phys. Chem. C **123**, 5951–5963 (2019). https://doi.org/10.1021/acs.jpcc.8b09598
296. Li, J.K., Gong, J.L.: Operando characterization techniques for electrocatalysis. Energy Environ. Sci. **13**, 3748–3779 (2020). https://doi.org/10.1039/d0ee01706j
297. Zhang, W., Huang, C.Q., Xiao, Q., et al.: Atypical oxygen-bearing copper boosts ethylene selectivity toward electrocatalytic CO_2 reduction. J. Am. Chem. Soc. **142**, 11417–11427 (2020). https://doi.org/10.1021/jacs.0c01562
298. Yao, K.L., Xia, Y.J., Li, J., et al.: Metal-organic framework derived copper catalysts for CO_2 to ethylene conversion. J. Mater. Chem. A **8**, 11117–11123 (2020). https://doi.org/10.1039/d0ta02395g
299. Wu, Y.H., Chen, C.J., Yan, X.P., et al.: Effect of the coordination environment of Cu in Cu_2O on the electroreduction of CO_2 to ethylene. Green Chem. **22**, 6340–6344 (2020). https://doi.org/10.1039/d0gc02842h
300. Tan, D.X., Zhang, J.L., Yao, L., et al.: Multi-shelled CuO microboxes for carbon dioxide reduction to ethylene. Nano Res. **13**, 768–774 (2020). https://doi.org/10.1007/s12274-020-2692-1
301. Gu, Z.X., Yang, N., Han, P., et al.: Oxygen vacancy tuning toward efficient electrocatalytic CO_2 reduction to C_2H_4. Small Methods. **3**, 1800449 (2018). https://doi.org/10.1002/smtd.201800449
302. Scholten, F., Sinev, I., Bernal, M., et al.: Plasma-modified dendritic Cu catalyst for CO_2 electroreduction. ACS Catal. **9**, 5496–5502 (2019). https://doi.org/10.1021/acscatal.9b00483
303. Li, J., Che, F., Pang, Y., et al.: Copper adparticle enabled selective electrosynthesis of n-propanol. Nat. Commun. **9**, 4614 (2018). https://doi.org/10.1038/s41467-018-07032-0
304. Pang, Y., Li, J., Wang, Z., et al.: Efficient electrocatalytic conversion of carbon monoxide to propanol using fragmented copper. Nat. Catal. **2**, 251–258 (2019). https://doi.org/10.1038/s41929-019-0225-7
305. Bernal, M., Bagger, A., Scholten, F., et al.: CO_2 electroreduction on copper-cobalt nanoparticles: size and composition effect. Nano Energy **53**, 27–36 (2018). https://doi.org/10.1016/j.nanoen.2018.08.027
306. Luo, M., Wang, Z., Li, Y.C., et al.: Hydroxide promotes carbon dioxide electroreduction to ethanol on copper via tuning of adsorbed hydrogen. Nat. Commun. **10**, 5814 (2019). https://doi.org/10.1038/s41467-019-13833-8
307. Weng, Z., Wu, Y., Wang, M., et al.: Active sites of copper-complex catalytic materials for electrochemical carbon dioxide reduction. Nat. Commun. **9**, 415 (2018). https://doi.org/10.1038/s41467-018-02819-7
308. Karapinar, D., Zitolo, A., Huan, T.N., et al.: Carbon-nanotube-supported copper polyphthalocyanine for efficient and selective electrocatalytic CO_2 reduction to CO. ChemSusChem **13**, 173–179 (2020). https://doi.org/10.1002/cssc.201902859
309. Ma, L.S., Hu, W.B., Mei, B.B., et al.: Covalent triazine framework confined copper catalysts for selective electrochemical CO_2 reduction: operando diagnosis of active sites. ACS Catal. **10**, 4534–4542 (2020). https://doi.org/10.1021/acscatal.0c00243
310. Liang, Z.Q., Zhuang, T.T., Seifitokaldani, A., et al.: Copper-on-nitride enhances the stable electrosynthesis of multi-carbon products from CO_2. Nat. Commun. **9**, 3828 (2018). https://doi.org/10.1038/s41467-018-06311-0
311. Yin, Z.Y., Yu, C., Zhao, Z.L., et al.: Cu_3N nanocubes for selective electrochemical reduction of CO_2 to ethylene. Nano Lett. **19**, 8658–8663 (2019). https://doi.org/10.1021/acs.nanolett.9b03324
312. Mi, Y.Y., Shen, S.B., Peng, X.Y., et al.: Selective electroreduction of CO_2 to C_2 products over Cu_3N–derived Cu nanowires. ChemElectroChem **6**, 2393–2397 (2019). https://doi.org/10.1002/celc.201801826

313. He, C.H., Duan, D.L., Low, J., et al.: $Cu_{2-x}S$ derived copper nanoparticles: a platform for unraveling the role of surface reconstruction in efficient electrocatalytic CO_2-to-C_2H_4 conversion. Nano Res. (2021). https://doi.org/10.1007/s12274-021-3532-7
314. Clark, E.L., Wong, J., Garza, A.J., et al.: Explaining the incorporation of oxygen derived from solvent water into the oxygenated products of CO reduction over Cu. J. Am. Chem. Soc. **141**, 4191–4193 (2019). https://doi.org/10.1021/jacs.8b13201
315. Jouny, M., Hutchings, G.S., Jiao, F.: Carbon monoxide electroreduction as an emerging platform for carbon utilization. Nat. Catal. **2**, 1062–1070 (2019). https://doi.org/10.1038/s41929-019-0388-2
316. Dunwell, M., Lu, Q., Heyes, J.M., et al.: The central role of bicarbonate in the electrochemical reduction of carbon dioxide on gold. J. Am. Chem. Soc. **139**, 3774–3783 (2017). https://doi.org/10.1021/jacs.6b13287
317. Iijima, G., Inomata, T., Yamaguchi, H., et al.: Role of a hydroxide layer on Cu electrodes in electrochemical CO_2 reduction. ACS Catal. **9**, 6305–6319 (2019). https://doi.org/10.1021/acscatal.9b00896
318. Lee, S.Y., Chae, S.Y., Jung, H., et al.: Controlling the C_{2+} product selectivity of electrochemical CO_2 reduction on an electrosprayed Cu catalyst. J. Mater. Chem. A **8**, 6210–6218 (2020). https://doi.org/10.1039/c9ta13173f
319. Wang, X., de Araújo, J.F., Ju, W., et al.: Mechanistic reaction pathways of enhanced ethylene yields during electroreduction of CO_2-CO co-feeds on Cu and Cu-tandem electrocatalysts. Nat. Nanotechnology **14**, 1063–1070 (2019). https://doi.org/10.1038/s41565-019-0551-6
320. Williams, K., Corbin, N., Zeng, J., et al.: Protecting effect of mass transport during electrochemical reduction of oxygenated carbon dioxide feedstocks. Sustain. Energy Fuels **3**, 1225–1232 (2019). https://doi.org/10.1039/c9se00024k
321. Ma, W., Xie, S., Zhang, X.G., et al.: Promoting electrocatalytic CO_2 reduction to formate via sulfur-boosting water activation on indium surfaces. Nat. Commun. **10**, 892 (2019). https://doi.org/10.1038/s41467-019-08805-x
322. Lin, L., Li, H.B., Yan, C.C., et al.: Synergistic catalysis over iron-nitrogen sites anchored with cobalt phthalocyanine for efficient CO_2 electroreduction. Adv. Mater. **31**, 1903470 (2019). https://doi.org/10.1002/adma.201903470
323. Wang, J.J., Kattel, S., Hawxhurst, C.J., et al.: Enhancing activity and reducing cost for electrochemical reduction of CO_2 by supporting palladium on metal carbides. Angew. Chem. Int. Ed. **58**, 6271–6275 (2019). https://doi.org/10.1002/anie.201900781
324. Luo, W.J., Nie, X.W., Janik, M.J., et al.: Facet dependence of CO_2 reduction paths on Cu electrodes. ACS Catal. **6**, 219–229 (2016). https://doi.org/10.1021/acscatal.5b01967
325. Nie, X.W., Luo, W.J., Janik, M.J., et al.: Reaction mechanisms of CO_2 electrochemical reduction on Cu(111) determined with density functional theory. J. Catal. **312**, 108–122 (2014). https://doi.org/10.1016/j.jcat.2014.01.013
326. Liu, S.P., Zhao, M., Gao, W., et al.: Mechanistic insights into the unique role of copper in CO_2 electroreduction reactions. ChemSusChem **10**, 387–393 (2017). https://doi.org/10.1002/cssc.201601144
327. Cheng, T., Fortunelli, A., Goddard, W.A., III.: Reaction intermediates during operando electrocatalysis identified from full solvent quantum mechanics molecular dynamics. PNAS **116**, 7718–7722 (2019). https://doi.org/10.1073/pnas.1821709116
328. Li, Y.W., Sun, Q.: Recent advances in breaking scaling relations for effective electrochemical conversion of CO_2. Adv. Energy Mater. **6**, 1600463 (2016). https://doi.org/10.1002/aenm.201600463
329. Birdja, Y.Y., Pérez-Gallent, E., Figueiredo, M.C., et al.: Advances and challenges in understanding the electrocatalytic conversion of carbon dioxide to fuels. Nat. Energy **4**, 732–745 (2019). https://doi.org/10.1038/s41560-019-0450-y
330. Calle-Vallejo, F., Koper, M.T.M.: Accounting for bifurcating pathways in the screening for CO_2 reduction catalysts. ACS Catal. **7**, 7346–7351 (2017). https://doi.org/10.1021/acscatal.7b02917
331. Cheng, T., Xiao, H., Goddard, W.A., III.: Free-energy barriers and reaction mechanisms for the electrochemical reduction of CO on the Cu(100) surface, including multiple layers of explicit solvent at pH 0. J. Phys. Chem. Lett. **6**, 4767–4773 (2015). https://doi.org/10.1021/acs.jpclett.5b02247
332. Nie, X.W., Esopi, M.R., Janik, M.J., et al.: Selectivity of CO_2 reduction on copper electrodes: the role of the kinetics of elementary steps. Angew. Chem. Int. Ed. **52**, 2459–2462 (2013). https://doi.org/10.1002/anie.201208320
333. Hussain, J., Jónsson, H., Skúlason, E.: Calculations of product selectivity in electrochemical CO_2 reduction. ACS Catal. **8**, 5240–5249 (2018). https://doi.org/10.1021/acscatal.7b03308
334. Lim, D.H., Jo, J.H., Shin, D.Y., et al.: Carbon dioxide conversion into hydrocarbon fuels on defective graphene-supported Cu nanoparticles from first principles. Nanoscale **6**, 5087–5092 (2014). https://doi.org/10.1039/c3nr06539a
335. Liu, S.G., Huang, S.P.: Size effects and active sites of Cu nanoparticle catalysts for CO_2 electroreduction. Appl. Surf. Sci. **475**, 20–27 (2019). https://doi.org/10.1016/j.apsusc.2018.12.251
336. Bu, Y.F., Zhao, M., Zhang, G.X., et al.: Electroreduction of CO_2 on Cu clusters: the effects of size, symmetry, and temperature. ChemElectroChem **6**, 1831–1837 (2019). https://doi.org/10.1002/celc.201801830
337. Cheng, T., Xiao, H., Goddard, W.A., III.: Full atomistic reaction mechanism with kinetics for CO reduction on Cu(100) from ab initio molecular dynamics free-energy calculations at 298 K. Proc. Natl. Acad. Sci. U.S.A. **114**, 1795–1800 (2017). https://doi.org/10.1073/pnas.1612106114
338. Rawat, K.S., Mahata, A., Pathak, B.: Thermochemical and electrochemical CO_2 reduction on octahedral Cu nanocluster: role of solvent towards product selectivity. J. Catal. **349**, 118–127 (2017). https://doi.org/10.1016/j.jcat.2017.03.011
339. Xiang, S.Q., Shi, J.L., Gao, S.T., et al.: Thermodynamic and kinetic competition between C–H and O–H bond formation pathways during electrochemical reduction of CO on copper electrodes. ACS Catal. **11**, 2422–2434 (2021). https://doi.org/10.1021/acscatal.0c05472
340. Sandberg, R.B., Montoya, J.H., Chan, K.R., et al.: CO–CO coupling on Cu facets: coverage, strain and field effects. Surface Sci. **654**, 56–62 (2016). https://doi.org/10.1016/j.susc.2016.08.006
341. Huang, Y., Handoko, A.D., Hirunsit, P., et al.: Electrochemical reduction of CO_2 using copper single-crystal surfaces: effects of CO* coverage on the selective formation of ethylene. ACS Catal. **7**, 1749–1756 (2017). https://doi.org/10.1021/acscatal.6b03147
342. Montoya, J.H., Peterson, A.A., Nørskov, J.K.: Insights into C–C coupling in CO_2 electroreduction on copper electrodes. ChemCatChem **5**, 737–742 (2013). https://doi.org/10.1002/cctc.201200564
343. Li, J., Wang, Z., McCallum, C., et al.: Constraining CO coverage on copper promotes high-efficiency ethylene electroproduction. Nat. Catal. **2**, 1124–1131 (2019). https://doi.org/10.1038/s41929-019-0380-x
344. Chang, X.X., Li, J., Xiong, H.C., et al.: C–C coupling is unlikely to be the rate-determining step in the formation of C_{2+} products in the copper-catalyzed electrochemical reduction of CO. Angew. Chem. Int. Ed. **61**, e202111167 (2022). https://doi.org/10.1002/anie.202111167
345. Cheng, D., Zhao, Z.J., Zhang, G., et al.: The nature of active sites for carbon dioxide electroreduction over oxide-derived copper

catalysts. Nat. Commun. **12**, 395 (2021). https://doi.org/10.1038/s41467-020-20615-0
346. Piqué, O., Low, Q.H., Handoko, A.D., et al.: Selectivity map for the late stages of CO and CO_2 reduction to C_2 species on copper electrodes. Angew. Chem. Int. Ed. **60**, 10784–10790 (2021). https://doi.org/10.1002/anie.202014060
347. Xiao, H., Cheng, T., Goddard, W.A., III.: Atomistic mechanisms underlying selectivities in C_1 and C_2 products from electrochemical reduction of CO on Cu(111). J. Am. Chem. Soc. **139**, 130–136 (2017). https://doi.org/10.1021/jacs.6b06846
348. Chen, R.X., Su, H.Y., Liu, D.Y., et al.: Highly selective production of ethylene by the electroreduction of carbon monoxide. Angew. Chem. Int. Ed. **59**, 154–160 (2020). https://doi.org/10.1002/anie.201910662

Xiaodeng Wang is a Lecturer at the School of Electronic and Electrical Engineering, Chongqing University of Arts and Sciences. He received his Ph.D. degree from the Chongqing University in 2019. He joined in Prof. Chuanxin He's group at Shenzhen University as a postdoc researcher in 2019. His research interests focus on synthesis of novel electrocatalysts for water splitting, and electrochemical reduction of CO_2.

Qi Hu received the Ph.D. degree from the Beijing University of Chemical Technology, China in 2016. He joined Prof. Chuanxin He's group at Shenzhen University as a postdoc researcher in 2016, and was promoted as an Associate Professor in 2021 at Shenzhen University. His current interests focus on the design and synthesis of nanocomposite materials for efficient electrocatalysis including water splitting, carbon dioxide reduction, and nitrate reduction.

Guodong Li received the Ph. D. degree from University of Science and Technology of China in 2019. After that, he joined Prof. Chuanxin He's group at Shenzhen University as a Post-doctor from 2019 to 2021. Currently, He is a postdoctoral researcher in Professor Yujie Sun's group at the University of Cincinnati. His current research interest is the hybrid molecular electrocatalysts for small molecule transformation and organic transformation, and photoactivable complexes and materials for luminescence sensing and phototherapy.

Hengpan Yang is an Assistant Professor at the College of Chemistry and Environmental Engineering, Shenzhen University. He received his Ph.D. degree from the East China Normal University in 2017. His research interests focus on synthesis of novel electrocatalysts and electrochemical CO_2 reduction.

Chuanxin He received his Ph.D. degree in polymer chemistry and physics from the University of Science and Technology of China in 2010. He joined the Department of Chemistry at Shenzhen University in 2010, and was promoted to Associate Professor in 2012 and Professor in 2019. His current research interests are to design and synthesize novel nanostructure materials for fuel cells, water splitting, and electrochemical reduction of CO_2.